A study on the structural, thermal, and mechanical properties of U1-yLnyO2-x and Ce1-yLnyO2-x (Ln = Gd, Er) solid solutions

ファム, ヴァン, マオ

Kyushu University

Graduated School of Engineering

Department of Applied Quantum Physics and Nuclear Engineering

A study on the structural, thermal, and mechanical properties of $U_{1-y}Ln_yO_{2-x}$ and $Ce_{1-y}Ln_yO_{2-x}$ (Ln = Gd, Er) solid solutions

By

PHAM VAN MAO

A thesis submitted in partial fulfillment of the requirements for the degree of Doctor of Philosophy

Supervised by

Prof. Kazuya Idemitsu

Associate Prof. Yaohiro Inagaki

Assistant Prof. Tatsumi Arima

July 19, 2021

Abstract

Burnable poison fuels, such as UO_2–$GdO_{1.5}$ are widely used in light-water reactors (LWRs), especially in pressurized water reactors. UO_2–$ErO_{1.5}$ is also a burnable absorber for LWRs. LWRs use $GdO_{1.5}$ or $ErO_{1.5}$ dispersed in UO_2 fuel pellets in several fuel rods in each fuel assembly. These burnable poisons help to control the initial reactivity and to spread the distribution of core power by keeping the power distribution uniform throughout the core life. In addition, they help to increase fuel burnup, to prolong the refueling cycle length, to reduce the number of control rods, and thereby to decrease the operating costs of the nuclear reactors. Moreover, burnable poisons decrease the necessary boron concentration in 1st cooling water for the chemical shim. However, the safety margin must be considered for using burnable poison fuel in nuclear reactors because $GdO_{1.5}$- and $ErO_{1.5}$-doped UO_2 have lower melting points and thermal conductivities than pure UO_2. Especially, lowering the thermal conductivity causes an increase in the center temperature of the fuel pellet and results in fission gas release, irradiation swelling, and other problems during reactor operation. In addition, the $LnO_{1.5}$ (Ln = Gd, Er) doping leads to the degradation in elastic moduli and Debye temperature of UO_2–$LnO_{1.5}$. The change in the crystal structure due to the dopant Ln^{3+} has the largest effect on these thermal and mechanical properties. However, the literature data on the atomic-scale structure of UO_2–$LnO_{1.5}$ are limited. Furthermore, although the thermal properties of UO_2–$LnO_{1.5}$ have been extensively studied, there are some differences in the literature data. Therefore, the structural, thermal, and mechanical properties of UO_2–$LnO_{1.5}$ must be experimentally evaluated and also confirmed by simulations.

In this study, the structural, thermal, and mechanical properties were evaluated for $U_{1-y}Ln_yO_{2-x}$ and $Ce_{1-y}Ln_yO_{2-x}$ (y = 0–0.4) solid solution samples by using both experimental and theoretical simulation methods. Here, with the similarity in crystal structures of UO_2–$GdO_{1.5}$ and CeO_2–$GdO_{1.5}$, CeO_2 was used as a surrogate material for UO_2 to measure the sound velocities in CeO_2–$GdO_{1.5}$ samples. The whole thesis is organized into eight chapters, as follows:

Chapter 1 introduces the fundamental concepts about the background of burnable poison fuel and nuclear fuel performance. This chapter describes the use of UO_2–$LnO_{1.5}$ in the LWRs as a burnable absorber and its advantages as well as its negative effects on the safety of a nuclear reactor.

Chapter 2 provides the phase relation of UO_2–$LnO_{1.5}$ and CeO_2–$LnO_{1.5}$ solid solutions. In addition, it explains the details about the methodology used in different sample preparations. Then, the sintered sample characteristics are also provided.

Chapter 3 provides an evaluation of the structural properties of UO_2–$LnO_{1.5}$ and CeO_2–$LnO_{1.5}$ samples by X-ray diffraction, Raman spectroscopy, and X-ray absorption fine structure (XAFS). The results are: the lattice parameters of UO_2–$LnO_{1.5}$ decreased as the $LnO_{1.5}$ content increased to 40 mol %. The UO_2–$LnO_{1.5}$

samples sintered in Ar-10% H_2 had a slightly larger lattice size than those sintered in Ar. Since the lattice parameter of UO_2–$LnO_{1.5}$ decreases as the O/M ratio increases, this observation indicated that the sample sintered under more reducing conditions with Ar-10% H_2 had a smaller O/M ratio than that sintered in Ar. However, the lattice parameters of UO_2–$LnO_{1.5}$ sintered under both conditions were close and they were also close to that of stoichiometric $(U,Ln)O_{2.00}$. When Ln^{3+} ions are substituted for U^{4+} ions in the host cation sites, either oxygen vacancies (V_O) are created or some of the U^{4+} are oxidized to U^{5+} or U^{6+} ions to maintain electrical neutrality. It was confirmed by XAFS that the oxidation state of U in the UO_2–$LnO_{1.5}$ was not solely tetravalent U^{4+}, partly oxidized to U^{5+}. A similar observation was obtained by Raman spectroscopy. The U–O and Ln–O interatomic distances decreased slightly with increasing $LnO_{1.5}$ content. The presence of U^{5+}, which has a smaller ionic radius than that of U^{4+}, therefore, resulted in the reduction in the lattice parameter of UO_2–$LnO_{1.5}$. For CeO_2–$LnO_{1.5}$ sintered in air, the lattice size of CeO_2–$GdO_{1.5}$ increased with increasing $GdO_{1.5}$ content, whereas that of CeO_2–$ErO_{1.5}$ decreased as the $ErO_{1.5}$ content increased. XAFS showed that Ce retained the Ce^{4+} cation, and both Ce–O and Ln–O interatomic distances decreased with increasing $LnO_{1.5}$ content. Therefore, the ionic radii of cations and V_O were supposed to determine the lattice sizes of these samples. Based on MD (molecular dynamics) simulation results of the lattice parameters, it is supposed that Ln^{3+} ions and V_O are not randomly distributed on cation and anion sites, respectively, but defect clusters, e.g., Ln^{3+}–V_O–Ln^{3+}, formed in CeO_2–$LnO_{1.5}$ samples. Thus, MD analyses well explained the increase and decrease in lattice parameters of CeO_2–$GdO_{1.5}$ and CeO_2–$ErO_{1.5}$, respectively, with an increase of Ln^{3+} content at the atomic scale.

Chapter 4 introduces the use of the laser flash analysis technique to simultaneously measure the heat capacities, thermal diffusivities, and thermal conductivities of UO_2–$LnO_{1.5}$ and CeO_2–$LnO_{1.5}$ samples. The results showed that the thermal conductivities of UO_2–$LnO_{1.5}$ and CeO_2–$LnO_{1.5}$ decreased with temperature up to nearly 1700 K and they also decreased as $LnO_{1.5}$ content increased up to 40 mol %. Thermal conductivities of the samples were mostly determined by phonon mean free path, which decreases due to the Umklapp processes at high temperatures, and due to the increase of phonon scattering caused by the increase of dopant Ln and oxygen vacancies at low temperatures.

Chapter 5 gives the sound velocity measurements of CeO_2–$GdO_{1.5}$ samples by the ultrasonic pulse-echo method. Then, the mechanical properties such as the elastic moduli and Debye temperature of CeO_2–$GdO_{1.5}$ samples, which were estimated from the longitudinal and transverse sound velocities, are discussed in detail. In addition, because of the lack of experimental data of UO_2–$LnO_{1.5}$ samples in this study, the data on mechanical properties of UO_2–$LnO_{1.5}$ were widely investigated in the literature. The results are: $LnO_{1.5}$ doping into CeO_2 or UO_2 decreased the sound velocities in both samples and thereby reduced their elastic moduli and Debye temperature.

Chapter 6 introduces the MD simulation method and results. The results showed that the lattice parameter, the thermal conductivity, and the bulk modulus of CeO_2–$LnO_{1.5}$ samples calculated by MD agreed well with those of experimental values.

Chapter 7 provides a comparison of the thermal and mechanical properties between UO_2–$LnO_{1.5}$ and CeO_2–$LnO_{1.5}$ samples. The results are: the effect of $LnO_{1.5}$ doping on the UO_2–$LnO_{1.5}$ system was comparable to that effect on CeO_2–$LnO_{1.5}$ system, which means these properties of both samples decreased as the $LnO_{1.5}$ content increased.

Finally, chapter 8 provides concisely the results and findings from this study, has the discussion and conclusions, and provides the potential improvements in detail for each research item.

Acknowledgment

An entire book won't be enough to thank all the people to whom I am grateful. Instead, I want to dedicate this part to an incomplete list of special people who had an impact throughout my journey in researching at Kyushu University and in writing this thesis. This accomplishment would not have been possible without them.

I would first like to give my profound gratitude to my parents, my brothers, and my sisters for providing me with unfailing support and continuous encouragement throughout my years of study in Japan. Their presence, unconditional support, and happiness are my driving force and guiding light in times of my life. I would not be who I am, now, without them.

It goes without saying, that I have the utmost respect, gratitude, and admiration toward my supervisors, Prof. Kazuya Idemitsu, Associate Prof. Yaohiro Inagaki, and Assistant Prof. Tatsumi Arima of the Department of Applied Quantum Physics and Nuclear Engineering, Graduate School of Engineering, Kyushu University, Japan, for giving me a valuable opportunity to do a lot of experiments at fully equipped laboratories, to do such works and for their valuable instructions and advices, their interest and instructions at each step of research, their helpful comments and suggestions during my researching for the success of this thesis. I owe them an immeasurable debt.

I would also like to thank the committee members, especially Prof. Yasukazu Murakami and Associate Prof. Kenichi Hashizume, who accepted to review this modest work and to give the possibility to discuss it and to take advantage of their remarks. And I really hope that this work will successfully address their concerns and requirements, meet their expectations and the trust that they granted me.

I would like to convey my gratitude to Dr. Yoshihiro Okamoto and Dr. Takayuki Nagai of the Japan Atomic Energy Agency (JAEA), for XAFS measurements, to Prof. Akira Kirishima and Assistant Prof. Daisuke Akiyama of the Institute of Multidisciplinary Research of Advanced Materials, Tohoku University, for allowing me to do many experiments during sample preparation and characterization, and to Assistant Prof. Midori Watanabe of the Center of Advanced Instrumental Analysis, Kyushu University, for XRD and Raman spectroscopy measurements.

I would also like to especially thank my company, Vietnam Electricity (EVN), for giving me all favorable conditions, continued and effective supports, and trust during my study at Kyushu University, so that I could gain lots of knowledge and improve experiences, and hereafter I will be able to grow it to contribute to Vietnam clean energy programs.

Finally, I was blessed to be surrounded by brilliant researchers and faculty members that inspired me, and I must express my very profound gratitude to my friends, especially Japanese friends in the laboratory for providing me with unconditional support throughout my years of living in Japan and through the process of researching and writing this thesis.

Thank you so much!

本研究を進めるにあたり直接御指導、御助言並びに御討論頂いた有馬立身助教に心より感謝し、お礼申し上げます。

また本研究に対して深い関心を示され、貴重な御意見を頂くと共に御検討して頂いた出光一哉教授、村上恭和教授、橋爪健一准教授、稲垣八穂広准教授に深く感謝致します。

本研究を進める上で協力、御助言して頂いた本研究室卒業生の山門鋼司氏、黒岩真成氏、岩佐龍磨氏、有光玄氏、山内宗治氏、栫優樹氏、大和邦滉氏、嘉藤良介氏、平川真之氏、山田良太氏、生田祥登氏、鯉池卓氏、古賀遼氏、吉田圭祐氏、

修士課程 2 年の武藤圭太氏、来海寿宏氏、福島七瀬氏、住吉壮斗氏、田中僚氏、修士課程 1 年の江上立樹氏、中崎友哉氏、南原傑氏、常楽忠宏氏、学部 4 年の横山礼幸氏、園田佑介氏、原田康平氏、飯田美穂氏に深く感謝致します。

PHAM VAN MAO

Declaration

I hereby declare that this thesis presented for the degree of doctor of philosophy was composed by myself, that the work contained herein is my own except where explicitly stated otherwise in the text, and that this work has not been submitted for any other institution for assessment purposes except as specified. Further, I have acknowledged all sources used and have cited these in the reference section.

Parts of this work have been published under the titles:

1. "*Evaluation of mechanical properties of $(Ce,Gd)O_{2-x}$ as a surrogate for $(U,Gd)O_{2-x}$ solid solutions*", Pham Van Mao, Tatsumi Arima, Yaohiro Inagaki, Kazuya Idemitsu, Proceedings of the 27th International Conference on Nuclear Engineering (ICONE-27), No. 1927 (2019), https://doi.org/10.1299/jsmeicone.2019.27.1927.
2. "*Evaluation of structural and thermal properties of $Ce_{1-y}Gd_yO_{2-x}$ solid solution*", International Journal of Thermophysics, 41-8, (2020) 111, http://doi.org/10.1007/s10765-020-02689-6.
3. "*Crystal structure of $U_{1-y}Ln_yO_{2-x}$ (Ln = Gd, Er) solid solution*", Pham Van Mao, Tatsumi Arima, Yaohiro Inagaki, Kazuya Idemitsu, Daisuke Akiyama, Takayuki Nagai, Yoshihiro Okamoto, Journal of Nuclear Materials, (2021), https://doi.org/10.1016/j.jnucmat.2021.153189.
4. "*Evaluation of melting behavior in the system UO_2-ZrO_2: Molecular dynamic simulation*", Tatsumi Arima, Junpei Miyachi, Pham Van Mao, Yaohiro Inagaki, Kazuya Idemitsu, Proceedings of the 27th International Conference on Nuclear Engineering (ICONE-27), No. 2095 (2019), http://doi.org/10.1299/jsmeicone.2019.27.2095.

Parts of this work were presented at the flowing conferences:

1. The 27th International Conference on Nuclear Engineering, May 19-24, 2019, Ibaraki, Japan: *"Evaluation of mechanical properties of $(Ce,Gd)O_{2-x}$ as a surrogate for $(U,Gd)O_{2-x}$ solid solutions"*, Pham Van Mao, Tatsumi Arima, Yaohiro Inagaki, Kazuya Idemitsu.
2. Kyushu University Open Innovation Workshop 2019, November 8, Kyushu University, Fukuoka, Japan: *"Evaluation of the thermal and mechanical properties of $(Ce,Gd)O_{2-x}$ solid solutions"*, Pham Van Mao.
3. Atomic Energy Society of Japan 2019 Meeting, December 7, Kyushu University, Fukuoka, Japan: *"Thermal properties of $(Ce,Gd)O_{2-x}$ and $(Ce,Er)O_{2-x}$ solid solutions"*, Pham Van Mao, Tatsumi Arima, Yaohiro Inagaki, Kazuya Idemitsu.
4. Atomic Energy Society of Japan 2020 Fall Meeting, September 16-18, online meeting: *"Study on the crystal structure of $U_{1-y}Ln_yO_{2-x}$ (Ln=Gd, Er) solid solutions"*, Pham Van Mao, Tatsumi Arima, Yaohiro Inagaki, Kazuya Idemitsu, Daisuke Akiyama, Takayuki Nagai, Yoshihiro Okamoto.

Table of contents

List of figures

List of tables and appendices

List of acronyms

UO_2	Uranium oxide (urania)
CeO_2	Cerium oxide (ceria)
PuO_2	Plutonium oxide
ThO_2	Thorium oxide
Gd_2O_3	Gadolinium oxide (gadolinia)
Er_2O_3	Erbium oxide (erbia)
BN	Boron nitride
UO_2–$GdO_{1.5}$	Uranium-gadolinium oxide
UO_2–$ErO_{1.5}$	Uranium-erbium oxide
$U_{1-y}Ln_yO_{2.00}$	Stoichiometric uranium-lanthanide oxide
$U_{1-y}Ln_yO_{2-x}$	Hypo-stoichiometric uranium-lanthanide oxide
$U_{1-y}Ln_yO_{2+x}$	Hyper-stoichiometric uranium-lanthanide oxide
CeO_2–$GdO_{1.5}$	Cerium-gadolinium oxide
CeO_2–$ErO_{1.5}$	Cerium-erbium oxide
BP	Burnable poison
LWRs	Light water reactors
PWRs	Pressurized water reactors
BWRs	Boiling water reactors
EFPD	Effective full power per day
F-type structure	Face-centered cubic (FCC)
C-type structure	Body-centered cubic (BCC)
MOX	Mixed oxide fuel
RE	Rare-earth
SOFC	Solid oxide fuel cells
TD	Theoretical density
O/M	The oxygen-to-metal ratio
CN	Coordination number
SEM	Scanning electron microscope
EDS	Energy dispersive spectroscopy
XRD	X-ray diffraction analysis
RS	Raman spectroscopy

XAFS	X-ray absorption fine structure
XANES	X-ray absorption near edge structure
EXAFS	Extended X-ray absorption fine structure
LFA	Laser flash analysis
IR	Infrared detector
UPE	Ultrasonic pulse-echo
MD	Molecular dynamics simulation
LMT	Laser melting technique
JAEA	Japan atomic energy agency

CHAPTER 1

INTRODUCTION

1.1 Background: nuclear fuels, burnable poison fuels, and nuclear fuel performance

For the nuclear fuel performance, thermo-physical and mechanical properties such as enthalpy, heat capacity, melting point, thermal diffusivity, thermal conductivity, the elastic moduli, and Debye temperature are very important. Systematic evaluation of these properties is, therefore, extremely essential to the safety of nuclear fuel management in nuclear power plants. For instance, the linear power of a fuel rod is dependent on its thermal conductivity and the temperature distribution in the pellet. As the higher the thermal conductivity, the lower the fuel centerline temperature. This results in an increase in the safety of the nuclear reactor and the retention of fission gas products.

Considerably more control reactivity is required before the startup of a new reactor core which is loaded with fresh fuels, and during the reactor core's early operating stages than that toward the end of the core life. A nuclear reactor core containing fresh fuels must have an excess reactivity to compensate for fuel depletion, production of fission product poisons, and temperature effects that introduce a negative reactivity. In order to reduce these control requirements, it is a common way to place burnable poison rods (UO_2–$LnO_{1.5}$) at selected locations in the reactor core. Figure 1 shows the fuel module cross-section and the distribution of the burnable poison rods in a fuel assembly in the reactor core, initial core loading for a typical commercial pressurized water reactor (PWR).

The need to improve reactor performance through longer cycle lengths or improved fuel utilization has been apparent since the beginning of commercial nuclear power generation. Among several modifications introduced as a consequence, the fuel initial enrichment has been increased, which means that the additional amount of fissile material (^{235}U) in the reactor core has to be compensated by the introduction of additional neutron absorber material in the reactor core. This compensation was initially achieved only by using neutron absorber materials assembled in control rods or/and by the addition of a soluble absorber (boric acid) in the reactor coolant.

In the boiling water reactors (BWRs), the use of a soluble absorber in the coolant/moderator was prohibited for technological reasons. In PWRs, the use of boric acid as a soluble absorber added to the coolant/moderator has been routinely used, but the increase in initial fuel enrichment cannot be indefinitely compensated by increasing the boric acid concentration. Beyond a certain concentration, thermal expansion of water at start-up reduces the quantity of boron in the core, resulting ultimately in a positive moderator reactivity coefficient, which is an unacceptable situation regarding the safe reactor operation. This is the reason why the introduction of solid burnable absorbers (or burnable poison) within the fuel rods was considered.

The use of a burnable poison in nuclear reactors provides the necessary negative moderator reactivity coefficient at the beginning of core life and helps shape core power distributions. The poison material should have a high neutron absorption cross-section and form daughter products with low absorption cross-sections. Then, as soon as the irradiation proceeds, the burnable poison burns up and the macroscopic absorption cross-section decreases.

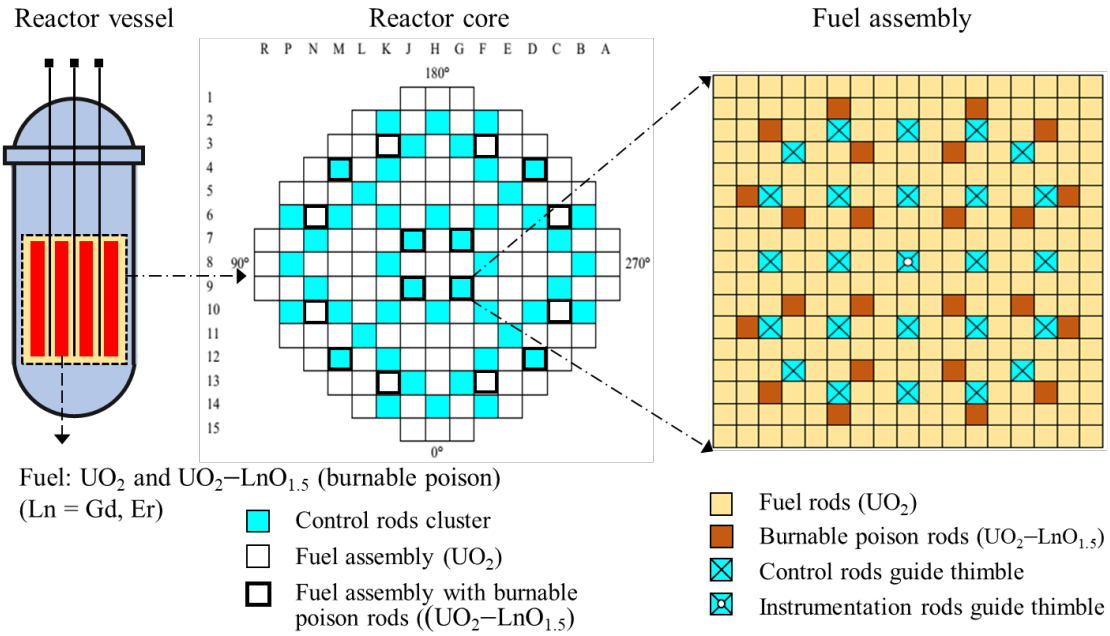

Figure 1. Typical commercial PWR fuel module cross-section and the arrangement of the burnable poison rods in a fuel assembly of initial core loading.

"*Poison*" is a material that absorbs neutrons unproductively and hence removes them from the fission chain reaction in a reactor, thereby decreasing its reactivity. In general, burnable poison is a nuclide that has a large absorption cross-section which is converted into a nuclide with a lower absorption cross-section as the result of neutron absorption. Thus, the increase in reactivity accompanying the burnup of the poison compensates to some extent for the decrease in reactivity due to fuel burnup and the accumulation of fission product poisons. Good burnable poisons have a high microscopic absorption cross-section for neutrons, do not fission, and create products having low microscopic absorption cross-sections.

A number of materials that consist of isotopes of ^{157}Gd, ^{167}Er, ^{164}Dy, ^{149}Sm, ^{177}Hf, and ^{151}Eu have been considered for burnable poisons. From a nuclear viewpoint, gadolinia ($GdO_{1.5}$) is an excellent burnable poison, having a high neutron absorption cross-section coupled to a burnup rate that, if properly designed, can match approximately the ^{235}U depletion, minimizing the reactivity penalty at the end-of-cycle. Gadolinium has several stable isotopes, many of which are strong absorbers, but ^{157}Gd (15.8% natural isotopic abundance) has a very high absorption cross-section for neutrons, and it transmutes to ^{158}Gd, which has an absorption cross-section for neutrons of only a few barns [1]. The UO_2–$GdO_{1.5}$ poisoned fuel was first introduced in 1967 in the BWR type Dresden 2 reactor. The maximum $GdO_{1.5}$ concentration usually

incorporated into the BWR fuel is about 4 wt %. Its use in PWR reactors is more recent and in general, requires higher $GdO_{1.5}$ concentrations (up to 10 wt %).

Currently, burnable poison fuels, such as UO_2–$GdO_{1.5}$ are widely used in light-water reactors (LWRs), especially in pressurized water reactors (PWRs) [2,3]. UO_2–$ErO_{1.5}$ is also a burnable absorber for PWRs [3,4]. Light-water reactors use gadolinia ($GdO_{1.5}$) or erbia ($ErO_{1.5}$) with uranium dioxide (UO_2) dispersed in the fuel pellets in several fuel rods in each fuel assembly. These materials help to control the initial reactivity and spread the distribution of core power by keeping the power distribution uniform throughout the core life. Figure 2 shows the effect of UO_2–$GdO_{1.5}$ burnable poison on multiplication factor K∞, which is defined as the number of fissions in one generation divided by the number in the preceding generation, or reactivity [4]. $K = 1$ is critical, $K > 1$ is supercritical (positive reactivity), $K < 1$ is subcritical (negative reactivity). For PWR assembly fueled without burnable poisons, $K\infty$ decreases with effective full power per day (EFPD) in a nearly linear shape. In contrast, with burnable poisons, a lower $K\infty$ can be kept, that is, a negative reactivity is introduced at the early operating stages of the reactor core [4]. The increase in reactivity accompanying the burnup of the poison compensates to some extent for the decrease in reactivity due to fuel burnup and the accumulation of fission product poisons. In addition, burnable poison fuel helps to increase fuel burnup, to prolong the refueling cycle length, and to reduce the number of control rods, decreasing the operating costs of the nuclear reactors [2–6]. Moreover, in water reactors controlled by chemical shim, burnable poisons decrease the necessary boron concentration in the 1st cooling water. This is shown in Fig. 3, where the boron concentration with and without burnable poison is indicated over the lifetime of the reactor core [7].

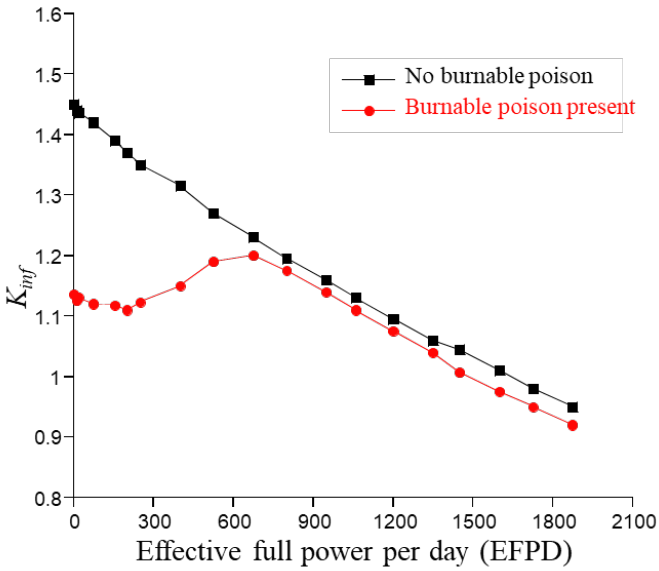

Figure 2. Infinity multiplication factor at different EFPD [4].

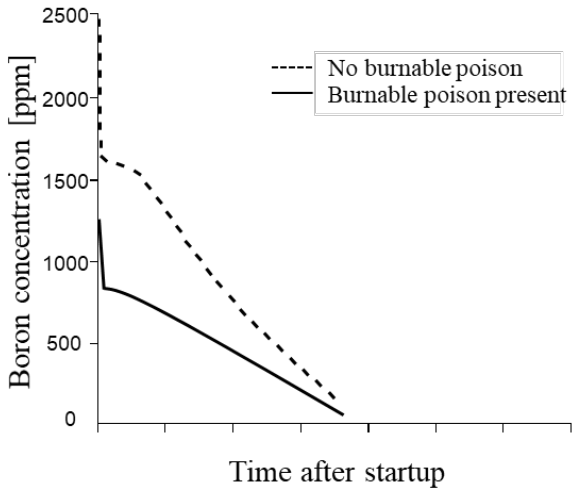

Figure 3. Boron shim with and without burnable poison (effect of burnable poison rods on soluble poison requirements) [7].

However, the safety margin must be considered for using burnable poison fuel in nuclear reactors because $GdO_{1.5}$- and $ErO_{1.5}$-doped UO_2 have lower melting points and thermal conductivities than UO_2 [8–12]. Especially, lowering the thermal conductivity increases the center temperature of the fuel pellet and results in fission gas release, irradiation swelling, and other problems during reactor operation. In addition, $LnO_{1.5}$ (Ln = Gd, Er) doping into UO_2 leads to the degradation in its elastic moduli and Debye temperature [13–15]. As a result, the safety of nuclear reactors might be reduced. The change in the crystal structure due to the dopant Ln^{3+} has the largest effect on these thermal and mechanical properties. The lattice parameter of UO_2–$LnO_{1.5}$ solid solutions decreases as the $LnO_{1.5}$ content increases [11,16–20]. In addition, the lattice parameter of UO_2–$LnO_{1.5}$ depends on stoichiometry, which decreases as the oxygen-to-metal (O/M) ratio (M = U + Ln) increases [16,17]. However, the literature data on the atomic-scale structure of UO_2–$LnO_{1.5}$ are limited [21]. Furthermore, although the thermal properties of UO_2–$LnO_{1.5}$ have been extensively studied, there are some differences in the literature data. Therefore, the crystal, thermal, and mechanical properties of UO_2–$LnO_{1.5}$ solid solutions must be experimentally evaluated and also confirmed by simulations.

UO_2 crystallizes in the cubic fluorite (F-type) structure and belongs to the *Fm*-3*m* space group, in which each U atom is surrounded by eight oxygen atoms. Gadolinium sesquioxide (Gd_2O_3) and erbium sesquioxide (Er_2O_3) have a cubic Mn_2O_3 (C-type) structure and belong to the *Ia*-3 space group, in which the oxygen coordination number (CN) for each Gd or Er atom is six. The UO_2–$GdO_{1.5}$ system has an F-type structure over a wide range of $GdO_{1.5}$ content up to the melting point [12].

UO_2 is the most widely used as nuclear fuel but it is a radioactive material and therefore it cannot be easily utilized in the laboratory. CeO_2 is, therefore, commonly used as a surrogate material for UO_2. Historically, CeO_2 has been used as a surrogate material for PuO_2, which is an oxide of fissile material used in mixed oxide fuel (MOX) more widely than for UO_2 because both Pu and Ce have similar ionic radii, only take on the 3^+ and 4^+ valence states when they are in oxide forms and have a crystal structure of fluorite. Similarly, in comparison with UO_2, CeO_2 has a close ionic radius in the case of U^{4+} and Ce^{4+} ions with CN = 8 and

possesses a similar crystal structure as UO_2. In terms of phase relation, with maximum a molar fraction of $LnO_{1.5}$ less than 40 % and sintered at 1873 K in this study, CeO_2–$LnO_{1.5}$ has almost the same crystal structures as UO_2–$LnO_{1.5}$ system [12,22]. Figure 4 shows the similarity in the crystal structures of UO_2 and CeO_2.

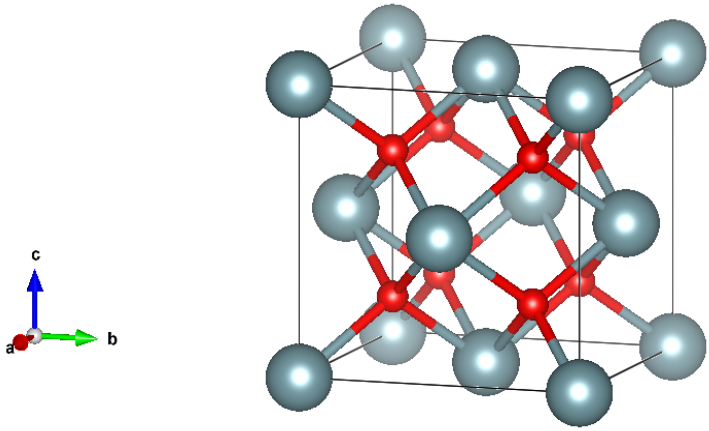

Figure 4. Crystal structure of UO_2 and CeO_2 (F-type). The small red circles illustrate oxygen ions. The gray balls indicate U^{4+} or Ce^{4+} ions in which each U or Ce atom is surrounded by eight O atoms.

On the other hand, rare-earth doped ceria $Ce_{1-y}RE_yO_{2-x}$ (RE: rare-earth) in recent years has been considered as electrolytes in intermediate temperature (773–1023 K) solid oxide fuel cells (SOFC). Ceria-based electrolyte $Ce_{1-y}Gd_yO_{2-x}$ offers many advantages due to its higher ionic conductivity compared with the yttria-stabilized zirconia (YSZ) electrolyte [23,24]. High oxide ion conduction in electrolyte $Ce_{1-y}Gd_yO_{2-x}$ makes it possible to decrease the operation temperature of SOFC, and thereby to solve technical problems.

In this study, the structural, thermal, and mechanical properties were evaluated for $U_{1-y}Ln_yO_{2-x}$ and $Ce_{1-y}Ln_yO_{2-x}$ (y = 0–0.4) solid solution samples by using both experimental and theoretical simulation methods. Here, with the similarity in the crystal structures of UO_2–$GdO_{1.5}$ and CeO_2–$GdO_{1.5}$, CeO_2 is used as a surrogate material for UO_2 to measure the sound velocities in CeO_2–$GdO_{1.5}$ samples.

1.2 Importance of the research, research objectives, and contributions

In fact, with the economic and technical benefits, burnable poison fuels are being used widely together with uranium dioxide in the LWRs within the safe margin in the commercial operation. In nuclear fuel management, the structural, thermal, and mechanical properties of the nuclear fuel pellets are of great importance. For instance, a lower thermal conductivity or lower melting point affects negatively the safety of a nuclear reactor. These properties are dependent on the density of the sample, temperature, chemical composition, grain boundaries, oxygen-to-metal ratio (O/M), etc. Therefore, evaluation of the effect of $LnO_{1.5}$ doping on UO_2 is very essential.

Besides, because of the difficultly in the use of UO_2 in the laboratory, the available data on the structural, thermal and mechanical properties such as local structures, the U-O and Ln-O interatomic distances, the

lattice parameters, thermal conductivities, melting points, the elastic moduli, and the Debye temperatures of UO_2–$LnO_{1.5}$ solid solutions are limited. In addition, there is little literature on the atomic-scale structure of $GdO_{1.5}$- and $ErO_{1.5}$-doped UO_2 solid solutions. Furthermore, although the thermal properties of UO_2–$LnO_{1.5}$ have been extensively studied, there are some differences in the experimental data of the literature. Therefore, the crystal structure, thermal, and mechanical properties of UO_2–$LnO_{1.5}$ solid solutions must be experimentally evaluated and also confirmed by simulations.

The main goal of this work was to provide a comprehensive evaluation of the effect of $LnO_{1.5}$ on such properties of UO_2–$LnO_{1.5}$ solid solution samples. In order to investigate such properties, in this study I used various techniques, i.e., scanning electron microscope (SEM), X-ray diffraction (XRD), Raman spectroscopy (RS), X-ray absorption fine structure (XAFS), laser flash analysis (LFA), ultrasonic pulse-echo (UPE), and laser melting technique (LMT) methods. Almost techniques used in this study are very advanced in studying strcutural, thermo-physical, and mechanical properties of materials. The measured results then were compared with the calculated results obtained from the theoretical simulation method using molecular dynamics simulations (MD).

1.3 Chapter outline

Chapter 1 introduces the fundamental concepts about the background of burnable poison fuel and nuclear fuel performance. This chapter describes the use of UO_2–$LnO_{1.5}$ in the LWRs as a burnable absorber and its advantages as well as its negative effects on the safety of a nuclear reactor. The rest of this dissertation is organized as follows:

Chapter 2 provides the phase relation of UO_2–$LnO_{1.5}$ and CeO_2–$LnO_{1.5}$ solid solutions. Moreover, it explains the details about the methodology used in different sample preparations. Then, the sintered sample characteristics are also provided.

Chapter 3 provides an evaluation of the structural properties of UO_2–$LnO_{1.5}$ and CeO_2–$LnO_{1.5}$ samples by using XRD, Raman spectroscopy, and XAFS techniques. Accordingly, this chapter discusses the effect of $LnO_{1.5}$ doping on the crystalline phases, crystallinities, lattice parameters, and local structures in the above solid solutions.

Chapter 4 introduces the use of the laser flash analysis technique to simultaneously measure the heat capacities, thermal diffusivities, and thermal conductivities of UO_2–$LnO_{1.5}$ and CeO_2–$LnO_{1.5}$ samples as functions of temperature and $LnO_{1.5}$ content.

Chapter 5 gives the sound velocity measurements of CeO_2–$GdO_{1.5}$ samples by the ultrasonic pulse-echo method. Then, the mechanical properties such as the elastic moduli and Debye temperature of CeO_2–$GdO_{1.5}$ samples, which were estimated from the longitudinal and transverse sound velocities, are discussed in detail.

In addition, because of the lack of experimental data of UO_2–$LnO_{1.5}$ samples in this study, the data on mechanical properties of UO_2–$LnO_{1.5}$ were widely investigated in the literature.

Chapter 6 introduces the MD simulation method. Then, the calculated lattice parameter, thermal conductivity, and bulk modulus of CeO_2–$LnO_{1.5}$ samples by MD simulations were compared with those of experimental results.

Chapter 7 provides a comparison of the thermal and mechanical properties between UO_2–$LnO_{1.5}$ and CeO_2–$LnO_{1.5}$ solid solution samples.

Finally, chapter 8 provides concisely the results and findings from this study, has the discussion and conclusions, and provides the potential improvements in detail for each research item.

1.4 References

[1] J.P.A. Renier, M.L. Grossbeck, “Development of improved burnable poisons for commercial nuclear power reactors”. 238 (2001).

[2] L. Goldstein, A.A. Strasser, Nucl. Tech. 60 (1983) 352–361.

[3] M.S. Yahya, H. Yu, Y. Kim, J. Nucl. Sci. Tech. 53 (2016) 1048–1060.

[4] A.A Galahom, Nucl. Ener. Tech. 4 (2018) 287–293.

[5] V. Barchevtsev, V. Artisyuk, H. Ninokata, J. Nucl. Sci. Tech. 39 (2002) 506–513.

[6] Rouf, Z. Su'ud, Indi. J. Sci. Tech. 28 (2016) 1–8.

[7] J.R. Lamarsh, A.J. Baratta, “Introduction to Nuclear Engineering”. 3 (2001).

[8] S. Fukushima, T. Ohmichi, A. Maeda, H. Watanabe, J. Nucl. Mater. 105 (1982) 201–210.

[9] K. Minato, T. Shiratori, H. Serizawa, K. Hayashi, K. Une, K. Nogita, M. Hirai, M. Amaya, J. Nucl. Mater. 288 (2001) 57–65.

[10] K. Iwasaki, T. Matsui, K. Yanai, R. Yuda, Y. Arita, T. Nagasaki, N. Yokohama, I. Tokura, K. Une, K. Harada, J. Nucl. Sci. Tech. 46 (2009) 673–676.

[11] S. Yamanaka, K. Kurosaki, M. Katayama, J. Adachi, M. Uno, T. Kuroishi, M. Yamasaki, J. Nucl. Mater. 389 (2009) 115–118.

[12] J.W. McMurray, D. Shin, B.W. Slone, T.M. Besmann, J. Nucl. Mater. 452 (2014) 397–406.

[13] S. Yamanaka, K. Kurosaki, M. Katayama, J. Adachi, M. Uno, T. Kuroishi, M. Yamasaki, J. Nucl. Matter. 389 (2009) 115–118.

[14] M. Hirai, Annual meeting of Japan Atomic Energy Society. 34 (1988) 262.

[15] M. Amaya, K. Une, M. Hirai, J. Nucl. Sci. Tech. 41 (2004) 108–115.

[16] T. Ohmichi, S. Fukushima, A. Maeda, H. Watanabe, J. Nucl. Mater. 102 (1981) 40–46.

[17] J. Kim, J. Lee, Y.S. Youn, N. Liu, J.G. Kim, Y.K. Ha, S.E. Bae, D.W. Shoesmith, J.Y. Kim, Electrochimica Acta. 247 (2017) 942–948.

[18] S.H. Kim, Y.G. Kim, H.S. Kim, S.H. Na, Y.W. Lee, D.S. Surh, J. Nucl. Mater. 342 (2005) 119–124.

[19] J. Lee, J. Kim, Y.S. Youn, N. Liu, J.G. Kim, Y.K. Ha, D.W. Shoesmith, J.Y. Kim, J. Nucl. Mater. 486 (2017) 216–221.

[20] M. Durazzo, A.C. Freitas, A.E.S Sansone, N.A.M. Ferreira, E.F.U. de Carvalho, H.G. Riella, R.M.L. Neto, J. Nucl. Mater. 510 (2018) 603–612.

[21] R. Bès, J. Pakarinen, A. Baena, S. Conradson, M. Verwerft, F. Tuomisto, J. Nucl. Mater. 489 (2017) 9–21.

[22] M. Zinkevich, D. Djurovic, F. Aldinger, in Proc. 7th Euro. SOFC Forum 2006, J.Kilner ed., (Lucerie, Switzerland, 2006) P0512 (CD ROM).

[23] V.V. Kharton, F.M. Figueiredo, L. Navarro, E.N. Naumovich, A.V. Kovalevsky, A.A. Yaremchenko, A.P. Viskup, A. Carneiro, F.M.B. Marques, J.R. Frade, J. Mater. Sci. 36 (2001) 1105–1117.

[24] N.M. Sammes, Zhihong Cai, Solid State Ion. 100 (1997) 39–44.

CHAPTER 2

SAMPLE PREPARATION

2.1 Introduction

As mentioned in Section 1.1, in the present study I prepared two types of samples UO_2–$LnO_{1.5}$ and CeO_2–$LnO_{1.5}$ solid solutions. The CeO_2 sample is used as a surrogate material for UO_2 due to the limitation and the difficulty in preparing uranium sample. In addition, the use of CeO_2–$LnO_{1.5}$ was to compare its thermal and mechanical properties with those of UO_2–$LnO_{1.5}$.

On the other hand, for chemical properties, both U and Ce have the possible 4^+ valence state in its oxide forms. However, the possible valence states of U (4^+, 5^+, 6^+) in their oxide forms can make CeO_2 become an inappropriate surrogate material, and hence our comprehensive evaluation of the thermo-physical properties of UO_2–$LnO_{1.5}$ might have not been possible. That is an additional reason why I used both UO_2–$LnO_{1.5}$ and CeO_2–$LnO_{1.5}$ samples in this study for comparison.

The UO_2, CeO_2, and Ln_2O_3 powders, which have high purity were used to prepare UO_2–$LnO_{1.5}$ and CeO_2–$LnO_{1.5}$ disk-shaped samples. The $LnO_{1.5}$ content was from 0 to 40 mol %. Figure 5 shows the SEM images of the pure CeO_2, UO_2, Gd_2O_3, and Er_2O_3 powders used in the present study. It can be seen, these powders were fine with a particle size of a few μm.

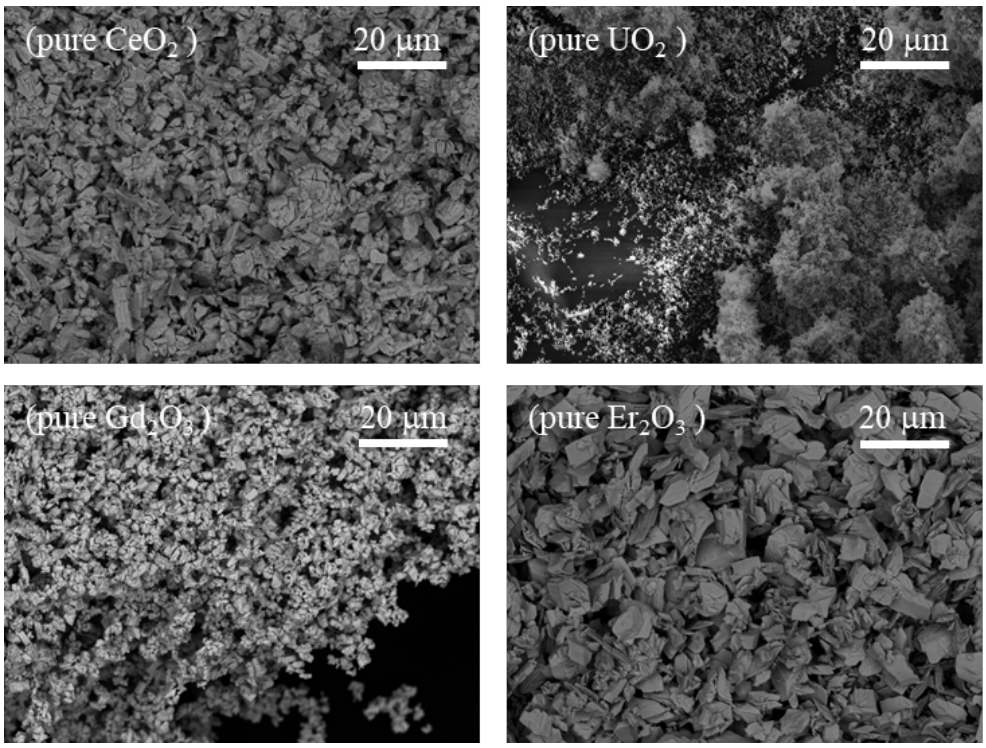

Figure 5. The SEM images of pure CeO_2, UO_2, Gd_2O_3, and Er_2O_3 powders used in the present study.

2.2 Phase diagrams

The phase relation of UO_2–$GdO_{1.5}$ solid solutions has been studied by previous investigators [1–5], and the phase diagrams are constructed by two different mechanical blending and coprecipitation methods. In these literature, XRD analysis indicates in both cases the presence of only F-type solid solution at $GdO_{1.5}$ contents up to 30–40 mol %. Liquidus temperatures from both studies decrease practically linearly with increasing $GdO_{1.5}$ content (from 3073 to 3033 K [1] or 3073 to 2973 K [2] for $GdO_{1.5}$ content up to 30 wt % (≈ 38.97 mol % $GdO_{1.5}$). However, it is assumed [2] that the solidus line would probably lie very close to the liquids line. On the other hand, there is little literature on the phase relation of UO_2–$ErO_{1.5}$ system [4]. In this relevant literature [4], the liquidus temperature of UO_2–$ErO_{1.5}$ decreases with increasing $ErO_{1.5}$ content up to 8 wt % $ErO_{1.5}$ (≈ 10.9 mol %). Summarizing the above investigations, it is concluded that the solidus line lies close to the liquidus even though it is difficult to specify the exact temperature difference between these lines. Data of literature shows a slight decrease in melting points of UO_2–$LnO_{1.5}$ with increasing $LnO_{1.5}$ content. In addition, although many reports have been published concerning the melting point of UO_2–$GdO_{1.5}$, the melting points of UO_2–$LnO_{1.5}$ solid solutions are still not yet finally established, due principally to the instability of samples over 3000 K and the difficulty of measuring the temperature at such a high level.

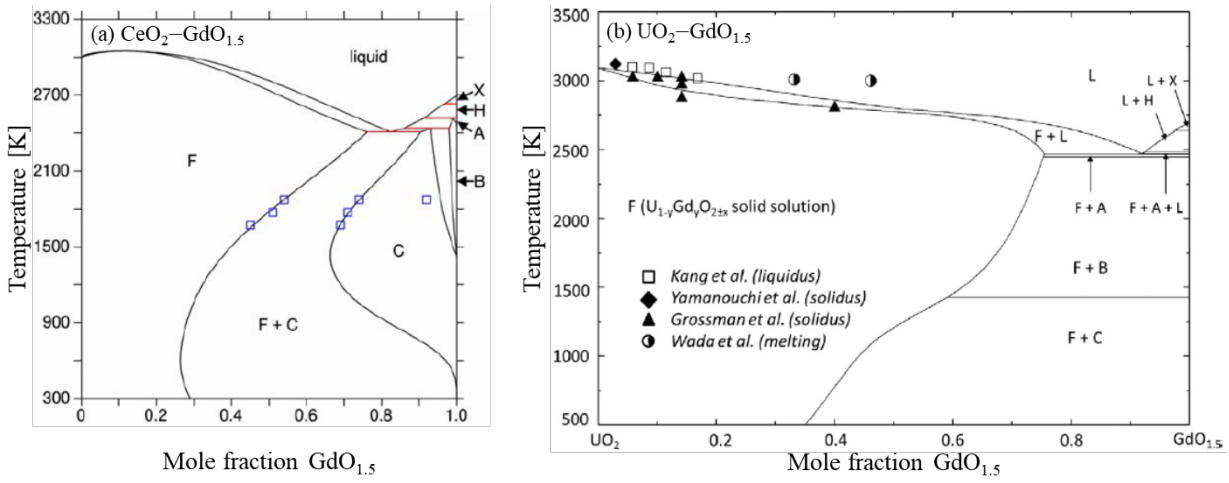

Figure 6. Proposed phase diagrams for the (a) CeO_2–$GdO_{1.5}$ [6] and (b) UO_2–$GdO_{1.5}$ systems [7]. C = low temperature cubic, B = monoclinic, A = low temperature hexagonal, H = high temperature hexagonal, X = high temperature cubic, L = liquid phase.

Figure 6 shows the phase diagrams for CeO_2–$GdO_{1.5}$ and UO_2–$GdO_{1.5}$ solid solutions suggested by M. Zinkevich et al. [6] and J.W. McMurray et al. [7], respectively. The phase relation behavior of $GdO_{1.5}$ was found to be different from those of UO_2 and CeO_2. In the case of the CeO_2–$GdO_{1.5}$ system, a monophasic F-type field is present throughout at 2700 K up to 40 mol % $GdO_{1.5}$. In the UO_2–$GdO_{1.5}$ system, the presence of a single-phase with F-type is observed up to 40 mol % $GdO_{1.5}$ at around 2700 K. Both these solid solutions have close melting points and their melting points decrease with increasing $GdO_{1.5}$ content. Although no phase diagrams data have been reported for UO_2–$ErO_{1.5}$ and CeO_2–$ErO_{1.5}$ solid solutions, with

a maximum of 40 mol % $LnO_{1.5}$ and sintered at temperatures of nearly 1973 K, it can be considered that both UO_2–$LnO_{1.5}$ and CeO_2–$LnO_{1.5}$ samples retained the same cubic fluorite structure in the present study.

2.3 The method used for the preparation of $U_{1-y}Ln_yO_{2-x}$ solid solutions

UO_2 powder was obtained by reducing U_3O_8 powder (Eq. (1)) in Ar-10% H_2 with a flow rate of 60 mL/min at 1273 K for 4 h. The crystal structure of the UO_2 powder was confirmed by XRD. The results showed that a cubic fluorite structure (CaF_2, hereafter F-type) was detected, and its lattice parameter (a = 0.5470 nm) was consistent with the reported value for UO_2 [8–12].

$$U_3O_8 + 2H_2 = 3UO_2 + 2H_2O. \quad (1)$$

UO_2–$LnO_{1.5}$ solid solution samples were prepared from UO_2 powder (the particle size of around 1 μm) and Ln_2O_3 powder (Gd_2O_3: Kanto Chemical, 99.95% purity, particle size of around 2 μm; Er_2O_3: Kanto Chemical, 99.95% purity, the particle size of around 5 μm), which were dry-milled, i.e., mechanical blending, together in a mortar for 30 min. The $LnO_{1.5}$ content was from 0 to 40 mol %. The mixed powders were uni-axially pressed into a disk-shaped pellet (7 mm in diameter and 1 mm thick) with a stainless-steel die at 10 MPa for 2 min. The green samples were sintered at 1973 K for 8 h under the following conditions: (i) samples A, A1–A5, and C1–C5: in an Ar flow (99.9999% purity, flow rate of 20 mL/min); and (ii) samples B, B1, B2, D1, and D2: in an Ar-10% H_2 flow (flow rate of 20 mL/min), and then cooled in the furnace. The Ar-10% H_2 atmosphere was more reducing than the Ar atmosphere. In addition, U_3O_8 and UO_3 samples were prepared for the XAFS measurements. The U_3O_8 powder was heat-treated at 1073 K in air for 4 h. The UO_3 sample was synthesized by heating $UO_2(NO_3)_2{\cdot}6H_2O$ at 500 K in air for 5 h. The crystal structures of these samples were confirmed by XRD. Fabrication and sintering of UO_2–$LnO_{1.5}$, U_3O_8 and, UO_3 samples, which are used for XRD and XAFS measurements were performed at Tohoku University.

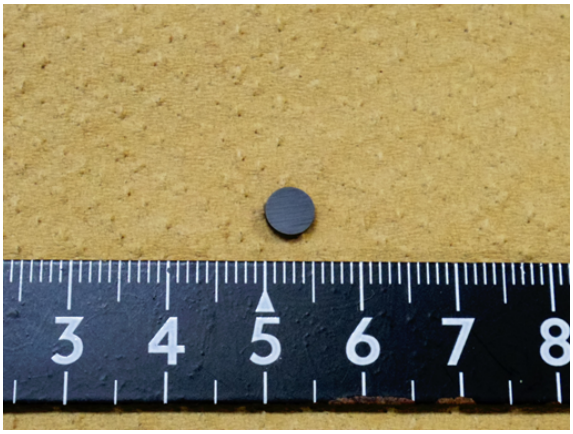

Figure 7. The image of sintered UO_2 pellet at 1973 K for 8 h.

On the other hand, the UO_2–$LnO_{1.5}$ samples, which are used for LFA and RS measurements were prepared at Kyushu University. The used powders are the same as above. The mixed powders were uni-axially pressed into a disk-shaped pellet (5.2 mm in diameter and 1 mm thick) with a stainless-steel die at 6 MPa

for 2 min. The green samples were sintered at 1973 K for 8 h in an Ar-10% H_2 flow (flow rate of 20 mL/min) and then cooled in the furnace. Figure 7 shows the image of the sintered UO_2–10 mol % $GdO_{1.5}$ pellet.

2.4 The method used for the preparation of $Ce_{1-y}Ln_yO_{2-x}$ solid solutions

UO_2–$LnO_{1.5}$ solid solution samples were prepared from CeO_2 (Kanto Chemical, 99.99% purity, the particle size of around 6 μm) and Ln_2O_3 powder (Gd_2O_3: Kanto Chemical, 99.95% purity, the particle size of around 2 μm; Er_2O_3: Kanto Chemical, 99.95% purity, particle size of around 5 μm), which were wet-milled together in a mortar with ethanol solution for 30 min to obtain a finer powder. Mixing the two oxides is very important to improve sample densities and to avoid the formation of agglomerates. If not properly mixed, the agglomerates might sinter together to form larger pores. The mixed powders were then dried by a drying oven (Model: ISUZU Hot Air Rapid Drying Oven "SS-K-1200") at 348 K for 24 h.

The calcined powders were uni-axially pressed into a disk-shaped pellet (5 mm in diameter and 0.95 mm thick) with a stainless-steel die at 6 MPa for 2 min. The compacted pellets or green pellets were sintered at 1873 K in air for 8 h with a rate of temperature rise (ramp rate) of 473K/h and naturally cooled with a maximum rate of temperature decrease of 473K/h in the electric furnace (Model: Morishiri Electric Furnace # 2416).

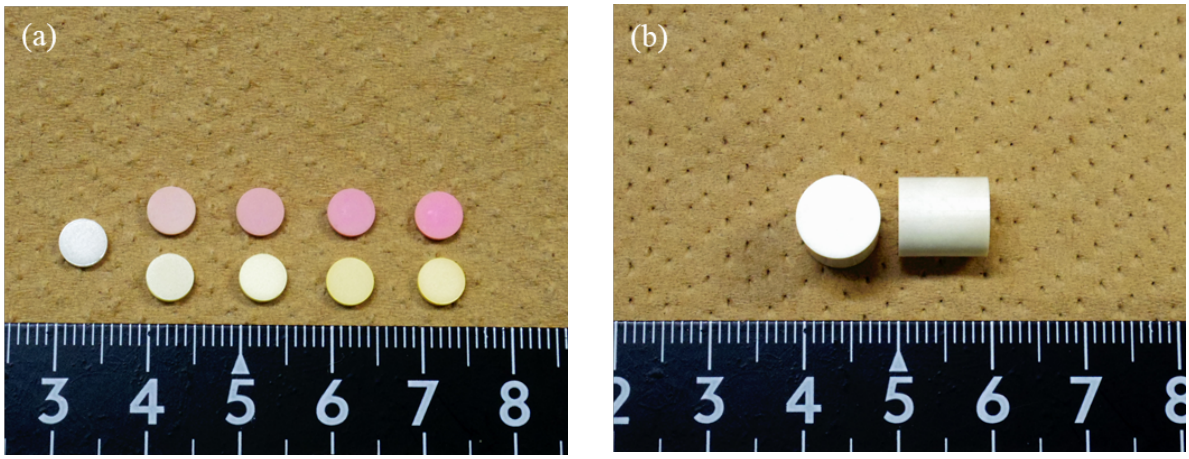

Figure 8. The image of two types of CeO_2–$LnO_{1.5}$ samples used for (a) XRD, Raman spectroscopy, XAFS, LFA, and MHT measurements; and (b) sound velocity measurements.

For sound velocities measurements, $Ce_{1-y}Gd_yO_{2-x}$ (y = 0.00, 0.05, 0.10, and 0.15) samples were prepared under the same method and conditions described above. However, the calcined CeO_2 powders were pressed into pellets at 1 MPa, 2 MPa, 3 MPa, 4 MPa, 5 MPa, 6 MPa, 7 MPa, 8 MPa, 9 MPa, and 10 MPa for 2 min. The purpose is to make pellets with various densities and thereafter systematically evaluate the effects of relative density of samples on the sound velocities. The compacted pellets were sintered at 1873 K in air for 8 h. The sintered pellets are approximately 9 mm in diameter and 7.5 mm in length in accordance with measuring conditions of sound velocity measurement. Figure 8 shows images of two types of CeO_2–$GdO_{1.5}$

samples with different sizes used in this study and Figure 9 presents the images of CeO_2–$LnO_{1.5}$ samples recorded by the camera. Here, the color of the samples is the real color.

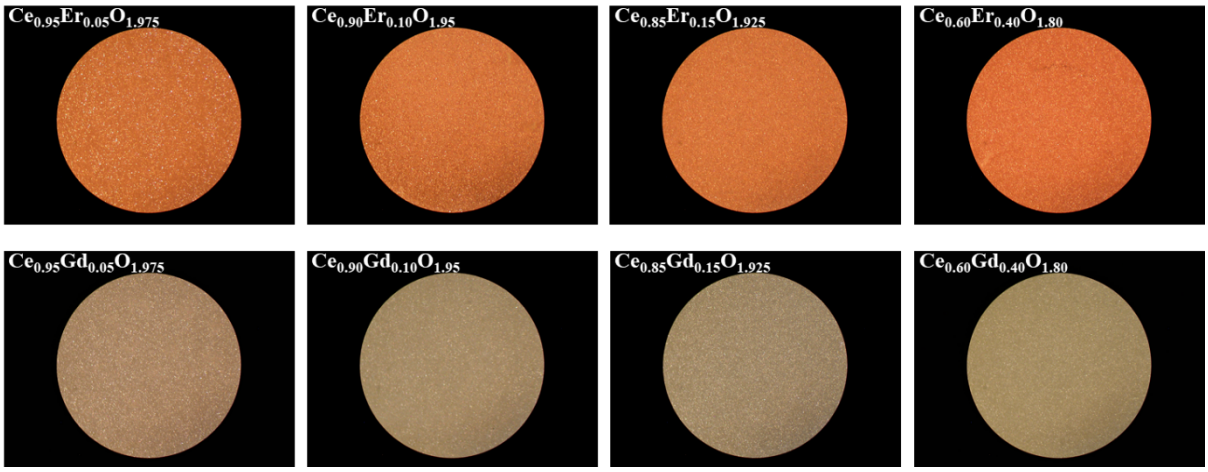

Figure 9. The images of CeO_2–$LnO_{1.5}$ samples taken by the camera.

2.5 Sample characteristics

For UO_2–$LnO_{1.5}$ samples, although the oxygen partial pressures were not measured, the atmosphere of Ar-10% H_2 was more reductive than that of Ar. Characteristics of UO_2–$LnO_{1.5}$ samples used for XRD and XAFS measurements are summarized in Table 1. Phase identifications and the lattice parameters were evaluated by XRD. The geometric properties of UO_2–$LnO_{1.5}$ samples used for LFA and RS measurements are given in Table 2.

The sintered densities of $U_{1-y}Ln_yO_{2-x}$ samples were calculated from the weight and the dimension of their samples. The theoretical density of the samples was calculated from the measured lattice parameters, which were derived from the XRD patterns while the crystal structure of the sample was confirmed to be F-type. For the assumed solid solutions $U_{1-y}Ln_yO_{2-x}$ with ($x = y/2$), the theoretical density is calculated by the following equation,

$$d_{th} = \left(\frac{4}{N_A a^3}\right)[(1-y)M_U + yM_{Ln} + (2-0.5y)M_O], \quad (2)$$

Where d_{th} is the theoretical density; N_A is Avogadro's constant; a is the lattice parameters; M_i refers to the atomic weight of uranium, gadolinium, erbium, and oxygen; and $y\times100$ is mol % of $LnO_{1.5}$ with $y = 0.00$, 0.0476, 0.05, 0.0954, 0.10, 0.1435, 0.15, 0.40 in UO_2–$LnO_{1.5}$ solid solutions. The relative density was the ratio of the sintered density to the theoretical one. The theoretical densities are given in Table 1. The relative densities of UO_2–$LnO_{1.5}$ solid solutions sintered at 1973 K for 8 h in an Ar-10% H_2 were around 81–94% TD (TD: theoretical density). The decrease in densities of UO_2–$LnO_{1.5}$ samples when the $LnO_{1.5}$ content increased was attributed to the increase of the pores (porosities) due to the dopant $LnO_{1.5}$. This observation was confirmed by SEM in Section 2.6.

Table 1. Sample characteristics and lattice parameters of UO_2–$LnO_{1.5}$ samples at room temperature (for XRD and XAFS measurements)

Sample name	$LnO_{1.5}$ content [mol %]	Sintering atmosphere	Apparent O/M ratio[(a)]	Theoretical density [g·cm^{-3}]	Phase	Lattice parameter [nm]
A	-, 0.0	Ar	2.000	10.958	fcc[(b)]	0.54707 ± 0.00009
B	-, 0.0	Ar-10% H_2	2.000	10.959	fcc	0.54706 ± 0.00005
A1	Gd, 4.76	Ar	1.976	10.844	fcc	0.54611 ± 0.00012
A2	Gd, 5.00	Ar	1.975	10.850	fcc	0.54586 ± 0.00002
A3	Gd, 9.54	Ar	1.952	10.720	fcc	0.54527 ± 0.00013
B1	Gd, 10.00	Ar-10% H_2	1.950	10.694	fcc	0.54542 ± 0.00010
A4	Gd, 14.35	Ar	1.928	10.586	fcc	0.54456 ± 0.00002
B2	Gd, 15.00	Ar-10% H_2	1.925	10.542	fcc	0.54491 ± 0.00013
A5	Gd, 40.00	Ar	1.800	9.860	fcc	0.54065 ± 0.00011
C1	Er, 4.76	Ar	1.976	10.884	fcc	0.54577 ± 0.00015
C2	Er, 5.00	Ar	1.975	10.883	fcc	0.54565 ± 0.00002
C3	Er, 9.54	Ar	1.952	10.833	fcc	0.54403 ± 0.00002
D1	Er, 10.00	Ar-10% H_2	1.950	10.803	fcc	0.54443 ± 0.00013
C4	Er, 14.35	Ar	1.928	10.731	fcc	0.54311 ± 0.00000
D2	Er, 15.00	Ar-10% H_2	1.925	10.683	fcc	0.54356 ± 0.00011
C5	Er, 40.00	Ar	1.800	10.264	fcc	0.53648 ± 0.00013

[(a)] I note that the apparent O/M ratio and theoretical density are calculated by assuming $x = y/2$ for $U_{1-y}Ln_yO_{2-x}$.

[(b)] fcc = face-centered cubic

Table 2. Geometric properties of UO_2–$LnO_{1.5}$ samples (for LFA and RS measurements)

$LnO_{1.5}$ content [mol %]	Sintering atmosphere	Sintered weight [g]	Diameter [mm]	Thickness [mm]	Sintered density [g·cm^{-3}]	Density [%TD[*]]
-, 0.0	Ar-10% H_2	0.1983	5.150	0.9300	10.2335	93.38
Gd, 5.00	Ar-10% H_2	0.1895	5.165	0.8920	10.1394	93.45
Gd, 10.00	Ar-10% H_2	0.1955	5.150	0.9563	9.8156	91.78
Gd, 15.00	Ar-10% H_2	0.1965	5.250	0.9548	9.5081	90.19
Gd, 40.00	Ar-10% H_2	0.1888	5.290	1.0703	8.0315	81.45
Er, 5.00	Ar-10% H_2	0.1930	5.190	0.9088	10.0387	92.24
Er, 10.00	Ar-10% H_2	0.1956	5.205	0.9283	9.9507	92.11
Er, 15.00	Ar-10% H_2	0.1952	5.195	0.9460	9.7390	91.16
Er, 40.00	Ar-10% H_2	0.1890	5.272	1.0320	8.3896	81.74

[(*)] Theoretical density

Table 3 summarizes the specimen composition, structures, characteristics, and lattice parameters for CeO_2–$GdO_{1.5}$ samples. The theoretical, sintered, and relative densities of CeO_2–$GdO_{1.5}$ solid solutions are also given in Table 3. The density of green pellets (green densities) was not measured in this study. The sintered density was measured by using Archimedes' principle with water and calculated from the weights and the dimensions of the samples. The measured densities were averaged values of five measurements. In all measurements, the standard deviations are less than approximately 2%. The purpose of preparing the ceramic powder using high purity reagent up to min.99.99% for CeO_2 and min.99.95% for $LnO_{1.5}$, and

sintering at high temperature was to obtain a highly sinterable fuel pellet, i.e. high-density pellet. As expected, the sintered pellets in this study could achieve high densities, as indicated in Table 3. For example, for CeO_2–10 mol % $GdO_{1.5}$ sample, the sintered density was 96.88% of theoretical density. Nearly complete theoretical density was reached. The theoretical densities of CeO_2–$LnO_{1.5}$ solid solutions were estimated from the measured lattice parameters, which were derived from the XRD patterns. The XRD measurements are provided in Section 3.2. Owing to the fact that, the density of a given substance depends upon the mass and volume, and the atomic weights of $GdO_{1.5}$ (181.25 g·mol^{-1}) and $ErO_{1.5}$ (191.26 g·mol^{-1}) are higher than that of CeO_2 (172.116 g·mol^{-1}), the density of CeO_2–$LnO_{1.5}$ increased as $GdO_{1.5}$ concentration increased.

Table 3. Sample characteristics and lattice parameters of CeO_2–$LnO_{1.5}$ samples at room temperature (for XRD and XAFS measurements)

$LnO_{1.5}$ content [mol %]	Sintering atmosphere	Apparent O/M ratio	Theoretical density [g·cm^{-3}]	Relative density [%TD*]	Phase	Lattice parameter [nm]
-, 0.0	Air	2.000	7.2196	95.2227 ± 1.9164	fcc	0.541074 ± 0.000005
Gd, 5.00	Air	1.975	7.2228	96.7476 ± 1.5034	fcc	0.541473 ± 0.000003
Gd, 10.00	Air	1.950	7.2302	96.8811 ± 1.1757	fcc	0.541764 ± 0.000003
Gd, 15.00	Air	1.925	7.2377	96.1079 ± 1.9781	fcc	0.542054 ± 0.000003
Gd, 40.00	Air	1.800	7.2980	96.3183 ± 1.5292	fcc	0.542918 ± 0.000004
Er, 5.00	Air	1.975	7.2682	95.7113 ± 1.7342	fcc	0.540864 ± 0.000003
Er, 10.00	Air	1.950	7.3193	95.4328 ± 1.6823	fcc	0.540596 ± 0.000002
Er, 15.00	Air	1.925	7.3655	95.0901 ± 1.1809	fcc	0.540450 ± 0.000004
Er, 40.00	Air	1.800	7.6386	94.3894 ± 1.6491	fcc	0.538755 ± 0.000010

On the other hand, the compositions, sizes, and sintered densities for CeO_2–$GdO_{1.5}$ specimens, which are used for sound velocities measurement are listed in Table 4. As mentioned earlier, for sound velocities measurement, CeO_2–$GdO_{1.5}$ pellets were prepared with various densities. Figure 10 shows the change in density of CeO_2 as a function of compacting pressure. The sintered density of CeO_2–$GdO_{1.5}$ samples increased linearly with the compacting pressure. As compacting pressure increased, the total porosity and the pore size decrease considerably. In addition, although the CeO_2–$GdO_{1.5}$ samples for sound velocities measurement were sintered at only 1873 K), the sintered density increases with sintering temperature and sintering duration as well. Furthermore, the density of samples depends somewhat on the grinding and mixing of the powders. In the present study, all samples were prepared under nearly the same grinding and mixing conditions.

Table 4. Geometric properties of CeO_2–$GdO_{1.5}$ samples (for sound velocities measurements)

$LnO_{1.5}$ content [mol %]	Sintering atmosphere	Sintered weight [g]	Diameter [mm]	Thickness [mm]	Sintered density [g·cm^{-3}]	Density [%TD*]
-, 0.0	Air	2.7593	8.850	7.257	6.5193	90.30
Gd, 5.00	Air	2.9430	8.985	7.827	6.9252	95.88
Gd, 10.00	Air	2.9257	9.017	7.877	6.8853	95.23
Gd, 15.00	Air	3.0233	9.025	7.192	6.9952	96.65

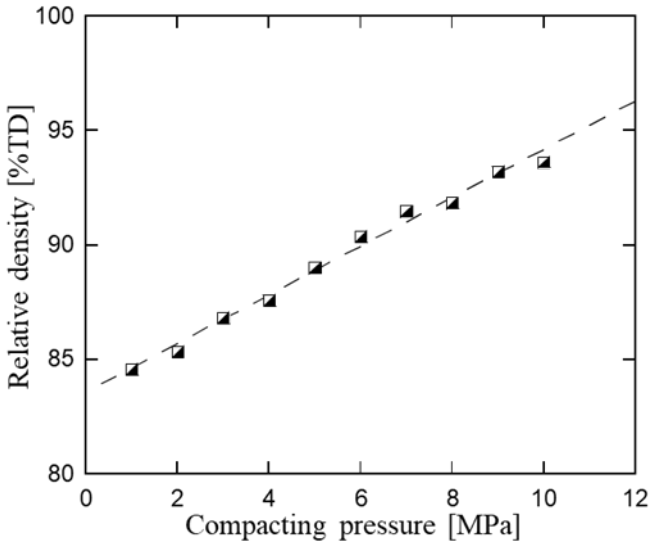

Figure 10. The change in sintered densities of CeO_2 at different compacting pressures. The dashed line is a guide to the eye.

The oxygen-to-metal (O/M) ratio (M = U or Ce + Ln) is an important parameter of nuclear fuel properties. The O/M ratio has not been confirmed experimentally. As given in Table 1, the apparent O/M ratio calculated from the chemical composition of the sample shows that the O/M ratio decreased from 2.000 for UO_2 to 1.800 for UO_2–40 mol % $LnO_{1.5}$. Note that the O/M ratios given in Table 1,3 do not correspond to actual ones because the oxygen contents were not obtained by the quantitative chemical analysis. The detailed discussion about the O/M ratio is given later.

2.6 Sample characterization

The surfaces of sintered samples were observed by scanning electron microscopy (SEM, Hitachi SU1510 and Hitachi TM3030 Plus Miniscope) to evaluate the grain size. In addition, the chemical composition and element distribution of sample surfaces were measured by the energy-dispersive X-ray spectroscopy (EDS). Figure 11 shows the EDS elemental maps for U, Gd, and Er of the samples B2 (UO_2–15 mol % $GdO_{1.5}$), A5 (UO_2–40 mol % $GdO_{1.5}$), D2 (UO_2–15 mol % $ErO_{1.5}$), and C5 (UO_2–40 mol % $ErO_{1.5}$). It can be noticed that there is a higher concentration of Gd and Er in samples A5 and C5 than B2 and D2, respectively, denoted by the light areas in Gd and Er mapping. In contrast, in U mapping, the areas of samples A5 and C5 are darker than those of samples B2 and D2.

Figures 12 and 13 show the SEM images of UO_2–$LnO_{1.5}$ surfaces. There were almost no microcracks on the surface of the samples. UO_2–$LnO_{1.5}$ samples prepared by mechanical blending in this study had good homogeneities. However, porosities appeared in the grain boundaries when $LnO_{1.5}$ is added into UO_2, and the number of porosities increased as the $LnO_{1.5}$ content increased up to 40 mol %. The sintered densities of UO_2–40 mol % $LnO_{1.5}$ samples were much smaller than that of UO_2 due to the pore formation. As the $LnO_{1.5}$ content increased, the pore sizes of these samples decreased.

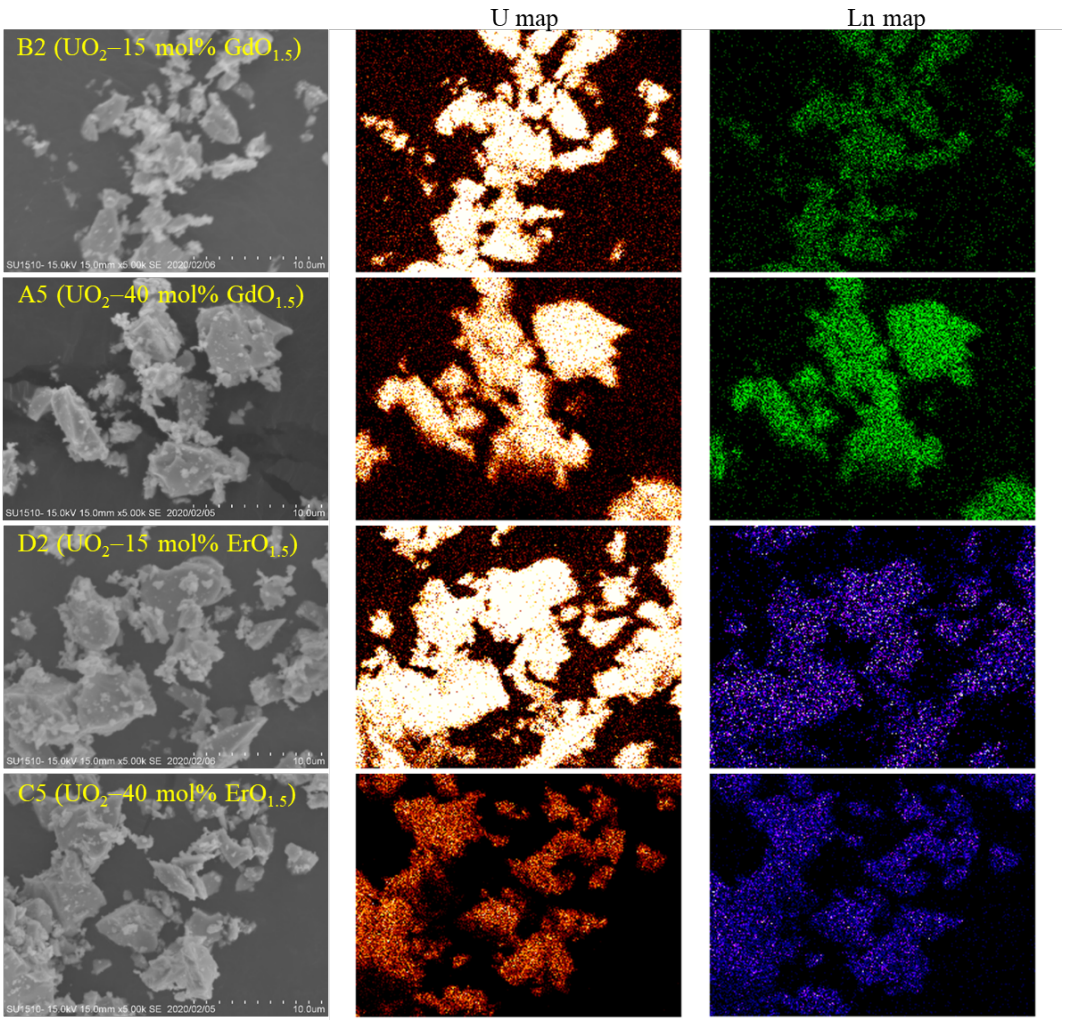

Figure 11. The EDS elemental mapping for U, Gd, and Er of the UO_2–15 mol % $LnO_{1.5}$ and UO_2–40 mol % $LnO_{1.5}$ samples sintered at 1973 K for 8 h.

From the SEM micrographs, the grain sizes were measured by the linear intercept method. In this method, a random straight line is drawn through the micrograph, the number of grain boundaries intersecting the line is counted, and then the average grain size is found by dividing the number of intersections by the actual line length. The measured results show that the grain growth was not observed for UO_2–$LnO_{1.5}$ samples. Instead, under the same sintering conditions, the grain size of sample surfaces decreased from around 10 µm for UO_2 to just approximately 1–2 µm for UO_2–40 mol % $LnO_{1.5}$ samples, though their grain boundaries were not clear because of the presence of porosity. This observation agreed well with the results observed in the literature [12,13]. The reduction in the grain size of UO_2–$LnO_{1.5}$ with the addition of $LnO_{1.5}$ probably caused the low densities of the samples. However, in the literature, Kogai et al. [14] explained the difference in grain growth rate between UO_2 and $(U,Gd)O_2$ through suppression of U atom diffusion in the $(U,Gd)O_2$ pellets. Littlechild et al. [15] also observed that the addition of small amounts of $GdO_{1.5}$ (less than 6 wt %) causes a decrease in grain size, but that, as $GdO_{1.5}$ content increases more than 6 wt %, grain size increases. It is clear that the grain size of the samples depends on the $LnO_{1.5}$ concentration, sintering atmosphere, oxygen potential, sintering temperature, and sintering duration. The difference from the

literature was, therefore, attributed to the differences in the method used for sample fabrication and sintering conditions.

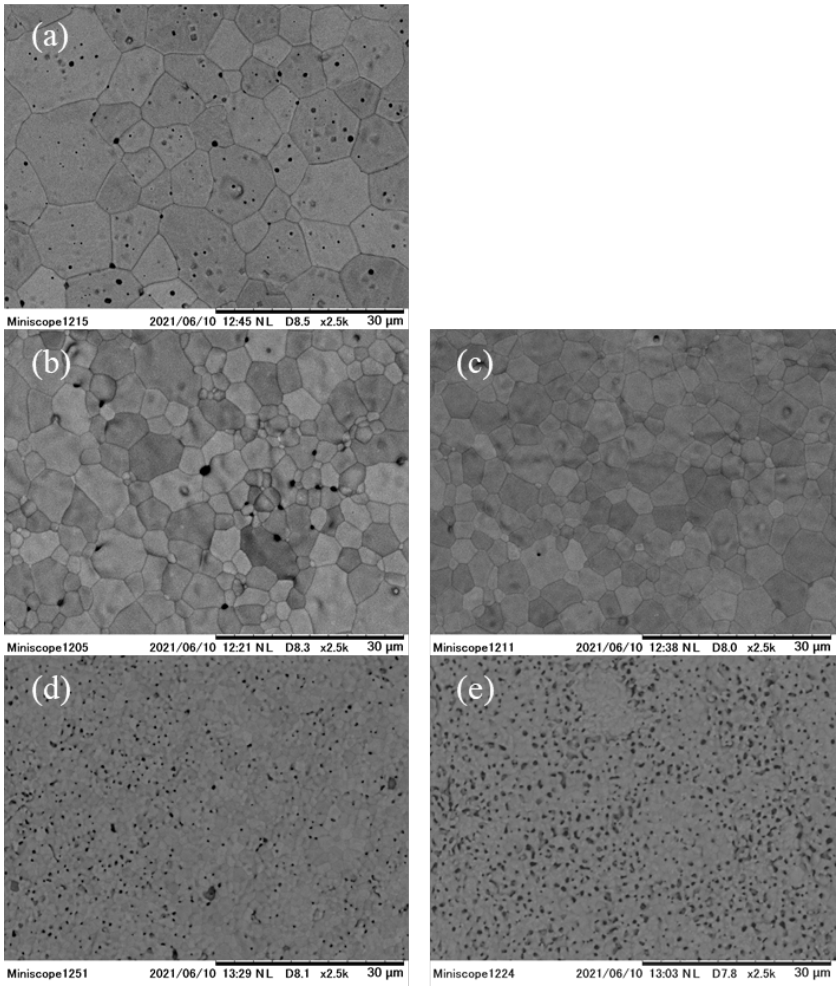

Figure 12. The SEM images of sintered $U_{1-y}Gd_yO_{2-x}$ sample surfaces with (a) $y = 0.00$, (b) $y = 0.05$, (c) $y = 0.10$, (d) $y = 0.15$, and (e) $y = 0.40$ sintered at 1973 K for 8 h.

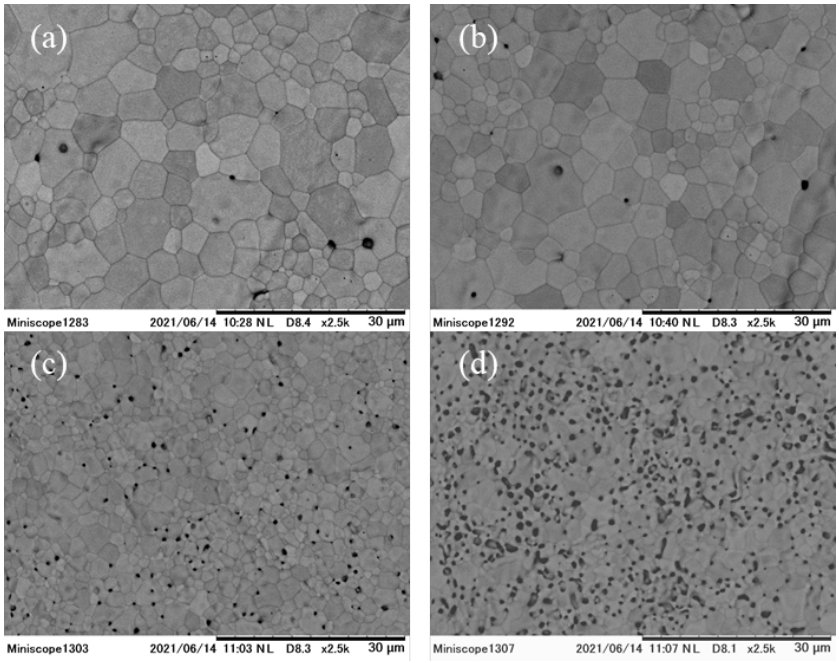

Figure 13. The SEM images of sintered $U_{1-y}Er_yO_{2-x}$ sample surfaces with (a) $y = 0.05$, (b) $y = 0.10$, (c) $y = 0.15$, and (d) $y = 0.40$ sintered at 1973 K for 8 h.

Figure 14 represents SEM images of surfaces for sintered CeO_2–$GdO_{1.5}$ pellets. Under the same sintering conditions, the average grain size of CeO_2 is about 30 µm while those of CeO_2–40 mol % $GdO_{1.5}$ and Gd_2O_3 are around 5 and 3.5 µm, respectively, though their grain boundaries were not clear because of the presence of porosity. It can be seen that pure CeO_2 shows a much bigger grain size compared with those of $GdO_{1.5}$-doped CeO_2 where the grain size slightly decreased with increasing $GdO_{1.5}$ content (3.5–9.5 µm). This suggests that $GdO_{1.5}$ doping into CeO_2 depressed the grain size of CeO_2–$GdO_{1.5}$. In addition, the CeO_2–$GdO_{1.5}$ samples were dense with low porosities up to 15 mol % $GdO_{1.5}$. In contrast, for CeO_2–40 mol % $GdO_{1.5}$ and $GdO_{1.5}$ samples shown in Figs. 14 (e) and (f), it was found that there were lots of black pores (porosities) in such pellets especially in $GdO_{1.5}$ because the pure $GdO_{1.5}$ powders were used to make pellets without grinding in a mortar with ethanol solution. The porosities and pore sizes in CeO_2–$GdO_{1.5}$ pellets increased with increasing $GdO_{1.5}$ content. For CeO_2–$ErO_{1.5}$ samples shown in Figure 15, the surfaces were not uniform, however, the CeO_2 powder and Er_2O_3 powder distributed separately. This observation indicated that the Er ions were not dissolved well in the Ce ion sites. The grain sizes of CeO_2–$ErO_{1.5}$ sample surfaces could not be estimated due to the poor crystallinity in the solid solutions. This observation suggested that under the same conditions, e.g. $LnO_{1.5}$ molar fraction and sintering conditions, $ErO_{1.5}$ seemed to be much more difficult to dissolve in the host Ce ions rather than $GdO_{1.5}$.

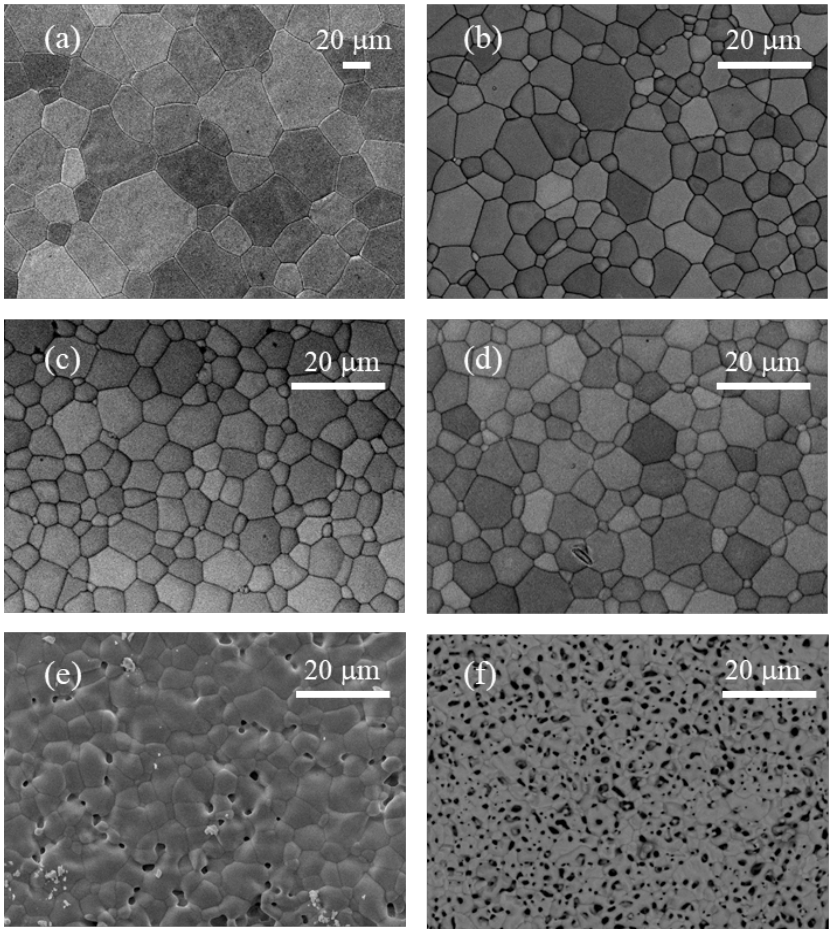

Figure 14. The SEM images of sintered $Ce_{1-y}Gd_yO_{2-x}$ sample surfaces with (a) $y = 0.00$, (b) $y = 0.05$, (c) $y = 0.10$, (d) $y = 0.15$, (e) $y = 0.40$, and (f) $y = 1.0$ sintered at 1873 K for 8 h.

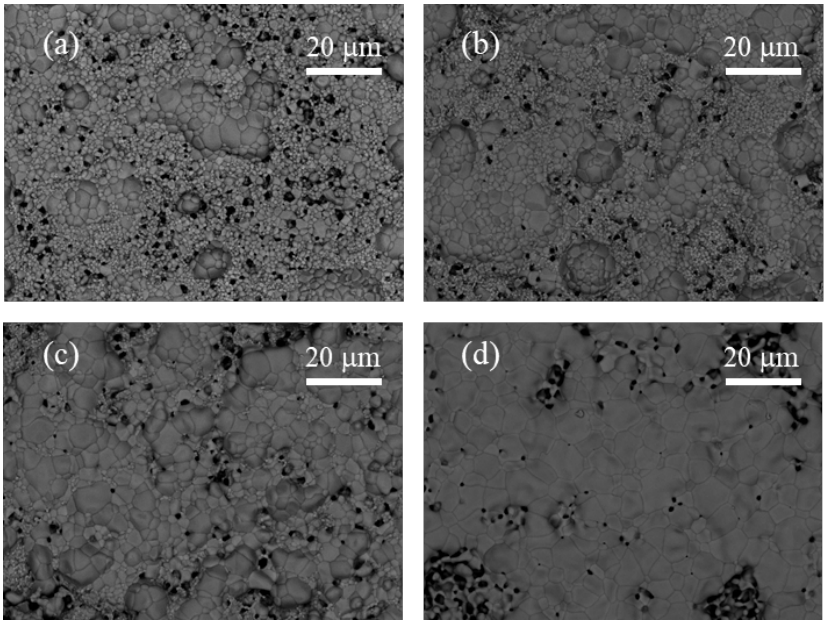

Figure 15. The SEM images of sintered $Ce_{1-y}Er_yO_{2-x}$ sample surfaces with (a) $y = 0.05$, (b) $y = 0.10$, (c) $y = 0.15$, and (d) $y = 0.40$ sintered at 1873 K for 8 h.

On the other hand, the chemical compositions were clearly identified by the EDS analysis. It was confirmed by the EDS analyses that the element segregation was not found on sample surfaces and the chemical composition remained almost unchanged during sintering. Figure 16 and Table 5 show the results obtained from the analysis of the chemical compositions by EDS for CeO_2–14.35 mol % $GdO_{1.5}$ sintered at 1873 K for 8 h. The $GdO_{1.5}$ accounted for 14.86 wt % (13.65 mol %) of the total. The observed results show that the chemical composition was only $(Ce,Gd)O_{2-x}$ and the powders had almost no other impurities.

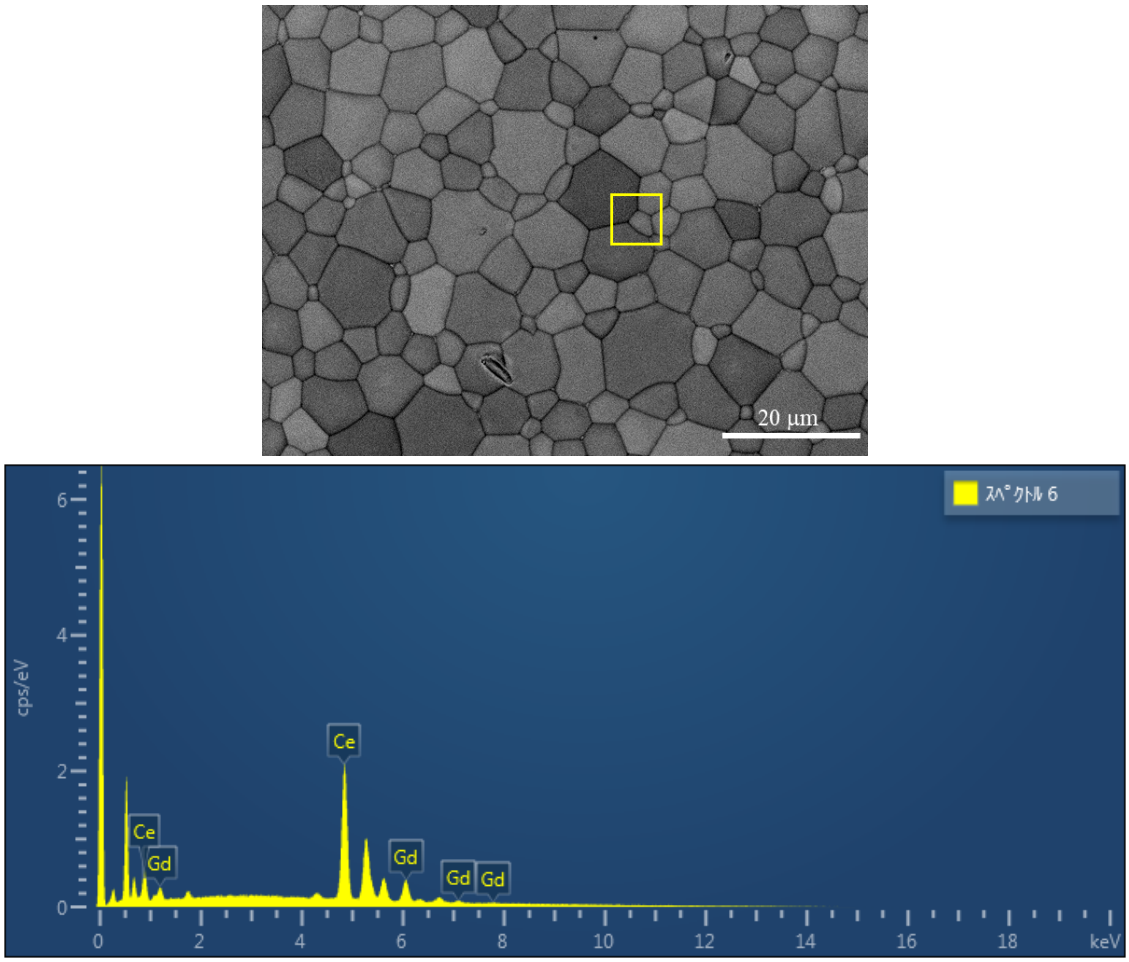

Figure 16. Chemical compositions analysis by EDS for CeO_2–14.35 mol % $GdO_{1.5}$ sintered at 1873 K for 8 h.

Table 5. EDS chemical compositions analysis results for CeO_2–14.35 mol % $GdO_{1.5}$ sample

Chemical element	Weight [%]	Weight error σ [%]	Atomic number [%]	Oxide composition	Oxide [%]	Oxide error σ [%]
Ce	72.69	0.41	34.54	CeO_2	85.14	0.49
Gd	12.89	0.41	5.46	Gd_2O_3	14.86	0.47
O	14.42	0.26	60.00			
Total	100.00		100.00		100.00	

2.7 Summary

UO_2–$LnO_{1.5}$ solid solution samples were prepared from UO_2 and Ln_2O_3 powders. CeO_2–$LnO_{1.5}$ solid

solution samples were a mixture of CeO_2 and Ln_2O_3 powders. The $LnO_{1.5}$ content was from 0 to 40 mol %. The green UO_2–$LnO_{1.5}$ samples were sintered at 1973 K under Ar and Ar-10% H_2 atmospheres for 8 h, whereas CeO_2–$LnO_{1.5}$ samples were sintered at 1873 K in air for 8 h. The oxygen potential pressure was not measured in this study, the Ar-10% H_2 was more reducing than the Ar atmosphere.

The surfaces of sintered samples were observed SEM. The chemical composition and element distribution of sample surfaces were analyzed by EDS. The observed results show that the element segregation was not found on sample surfaces, the chemical composition remained almost unchanged during sintering and the powders had almost no other impurities. In addition, $LnO_{1.5}$ doping into UO_2 decreased the grain sizes of UO_2–$LnO_{1.5}$ samples. Likewise, the grain size of CeO_2–$GdO_{1.5}$ sample decreased as $GdO_{1.5}$ content increased. The porosities of these samples increased and their pore sizes increased with increasing $LnO_{1.5}$ content.

The surfaces of CeO_2–$ErO_{1.5}$ samples were not uniform indicating Er ions were not dissolved well in the Ce ion sites. This observation suggested that under the same conditions, $ErO_{1.5}$ seemed to be much more difficult to dissolve in the host Ce ions rather than $GdO_{1.5}$.

2.8 References

[1] R.Y. Beals, J.H. Handwerk, B.Y. Wrona, J. Am. Ceram. Soc. 51 (1969) 578–581.

[2] T. Wada, K. Noro, K. Tsukui, Proc. Int. Conf. BNES on Nuclear fuel performance. (15-19 Oct. 1973, London, UK) 63.1–63.3.

[3] K.W. Kang, J.H. Yang, J.H. Kim, Y.W. Rhee, D.J. Kim, K.S. Kim, K.W. Song, Thermochimica Acta 455 (2007) 134–137.

[4] Matsuoka, Fall meeting of the Atomic Energy Society of Japan (1990).

[5] L.N. Grossman, Colloques Int. CNRS 205 (1972) 453.

[6] M. Zinkevich, D. Djurovic, F. Aldinger, in Proc. 7th Euro. SOFC Forum 2006, J.Kilner ed., (Lucerie, Switzerland, 2006) P0512 (CD ROM).

[7] J.W. McMurray, D. Shin, B.W. Slone, T.M. Besmann, J. Nucl. Mater. 452 (2014) 397–406.

[8] S. Fukushima, T. Ohmichi, A. Maeda, H. Watanabe, J. Nucl. Mater. 105 (1982) 201–210.

[9] M. Hirai, J. Nucl. Mater. 173 (1990) 247–254.

[10] R.J. Beals, J. H. Handwerk, J. Am. Ceram. Soc. 48 (1965) 271–274.

[11] K. Minato, T. Shiratori, H. Serizawa, K. Hayashi, K. Une, K. Nogita, M. Hirai, M. Amaya, J. Nucl. Mater. 288 (2001) 57–65.

[12] L.Z. Evins, A. Valls, L. Duro, Proceedings of the Second Meeting of the EURATOM, (27-29 May 2019, Cologne, Germany) 75–88.

[13] S. Yamanaka, K. Kurosaki, M. Katayama, J. Adachi, M. Uno, T. Kuroishi, M. Yamasaki, J. Nucl. Mater. 389 (2009) 115–118.

[14] K. Iwasaki, T. Matsui, K. Yanai, R. Yuda, Y. Arita, T. Nagasaki, N. Yokohama, I. Tokura, K. Une, K. Harada, J. Nucl. Sci. Tech. 46 (2009) 673–676.
[15] T. Kogai, J. Nucl. Sci. Tech. 28 (1989) 744–751.
[16] J.E. Littlechild, G.G. Butler, G.W. Lester, Proc. Int. Conf. BNES on Nuclear Fuel Performance, (15-19 October 1973, London, UK) 65.1–65.4.

CHAPTER 3

EVALUATION OF THE STRUCTURAL PROPERTIES OF $U_{1-y}Ln_yO_{2-x}$ AND $Ce_{1-y}Ln_yO_{2-x}$ SOLID SOLUTIONS

3.1 Introduction

The structure properties such as the crystal structure and lattice parameter are very important. In order to evaluate these properties, the XRD method was used in the present study. From the obtained XRD patterns, the powder crystallinity and the lattice parameter, *a*, can be evaluated. Diffraction peak smoothing was performed by using Fityk software. A simple method for the determination of lattice parameters of the crystals with known crystal structure from obtained powder XRD data was used. This estimation is based on the Nelson-Riley (N-R) extrapolation function and the least-squares analysis. And also, the full pattern fitting through the Rietveld method was carried out for structural refinement and characterization. Rietveld refinement analysis was performed for the XRD patterns collected at room temperature from high resolution grazing angle using PDXL (Integrated X-ray powder diffraction) software. In addition, the Raman spectroscopy technique was efficiently used as complementary to XRD in studying phase identification.

On the other hand, XAFS measurements were also performed for UO_2–$LnO_{1.5}$ and CeO_2–$LnO_{1.5}$ samples. The structural parameters, such as oxidation state, coordination number CN, the interatomic distances corresponding to the nearest cation-oxygen pair were determined by curve fitting analyses.

3.2 X-ray diffraction (XRD)

XRD is one of the most important non-destructive tools to analyze all kinds of matter, ranging from fluids to powders and crystals. XRD techniques are used for the identification of crystalline phases of various materials and the quantitative phase analysis after the identification. XRD techniques are superior in elucidating the three-dimensional atomic structure of crystalline solids. The properties and functions of materials largely depend on the crystal structures. X-ray diffraction technique has, therefore, been widely used as an indispensable means in materials research, development, and production.

XRD is based on constructive interference of monochromatic X-rays and a crystalline sample. These X-rays are generated from a cathode ray tube, filtered to produce monochromatic radiation, collimated to concentrate, and directed towards the sample. The interaction of incident rays with the sample produces constructive interference when conditions satisfy Bragg's Law. Figure 17 shows the schematic principle of a typical X-ray diffractometer and a picture of Rigaku MiniFlex 600 instruments used in the present study. In principle, when an incident X-ray beam interacts with the planes of atoms, a part of the beam is transmitted, a part is absorbed by the sample, a part is refracted and scattered, and a part is diffracted. X-rays are diffracted, depending on what atoms make up the crystal lattice and how these atoms are arranged.

When an X-ray beam hits a sample and is diffracted, the distance between the planes of the atoms that constitute the crystalline materials can be measured based on Bragg's Law. In the XRD, the general relationship between the wavelength of the incident X-rays, diffraction angle, and lattice spacing between the crystal lattice planes of atoms is known as Bragg's Law, expressed as:

$$n\lambda = 2d\,sin\,\theta, \tag{3}$$

where n (an integer) is the other of reflection, λ is the characteristic wavelength of the incident X-rays impinging on the crystallize sample, d is the interplanar spacing between rows of atoms in a crystalline sample, and θ is the angle of the X-ray beam with respect to these planes.

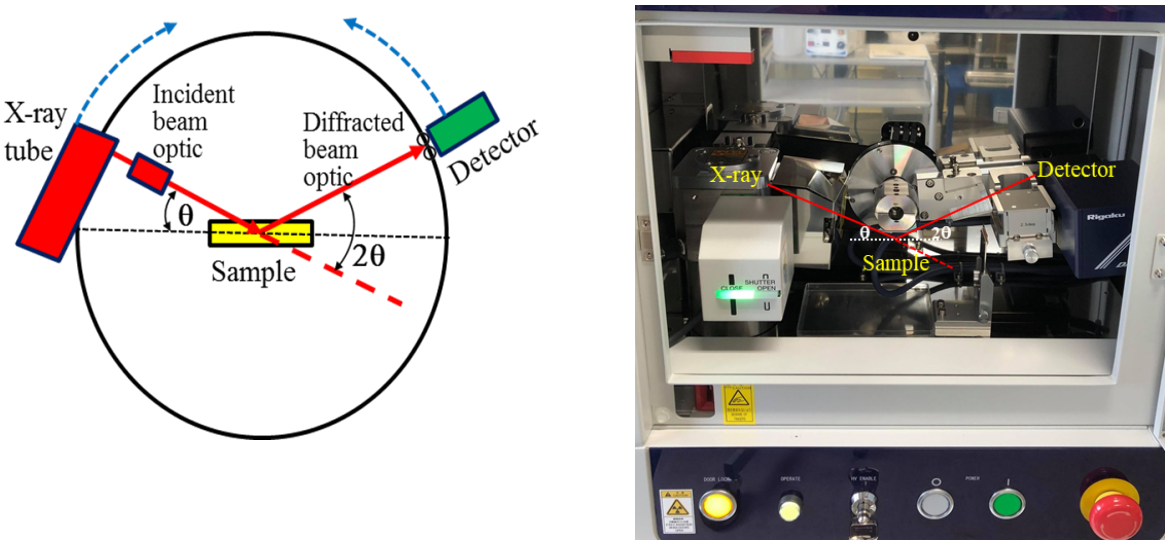

Figure 17. Schematics of a typical X-ray diffractometer, and the image of Rigaku MiniFlex 600 instruments.

Bragg's law of diffraction is shown in Fig. 18. When Eq. (3) is satisfied, X-rays scattered by the atoms in the plane of a periodic structure are in phase and diffraction occurs in the direction defined by the angle θ. In the simplest instance, an XRD experiment consists of a set of diffracted intensities and the angles at which they are observed. This diffraction pattern can be thought of as a chemical fingerprint, and chemical identification can be performed by comparing this diffraction pattern to a database of known patterns. In general, the positions and intensity magnitude of the diffraction peaks are used for identifying the underlying structure (or phase) of crystalline materials. This phase identification is important because the structure of materials is mostly dependent on the crystal structure.

The Cu-Kα consists, in part, of $K\alpha_1$ and $K\alpha_2$. $K\alpha_1$ has a slightly shorter wavelength and twice the intensity as $K\alpha_2$. Copper is the most common target material for single-crystal diffraction, with Cu-Kα, $K\alpha_1$, and $K\alpha_2$ are 0.1541838 nm, 0.1540562 nm, and 0.1544390 nm, respectively.

XRD (MiniFlex 600, Rigaku) was used to identify the phase and determine the lattice parameters. The sintered UO_2–$LnO_{1.5}$ and CeO_2–$LnO_{1.5}$ samples were ground into powder and measured at room

temperature using Cu-Kα radiation (λ = 0.154056 nm) in the 2θ range of 20–140° with a scan speed of 5°/min, step 0.02 at 40 kV and 15 mA. The XRD patterns were fitted by Rietveld refinement.

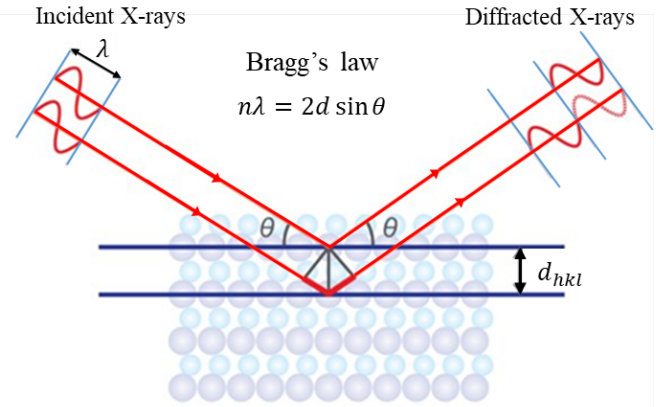

Figure 18. Schematic illustration of Bragg's law reflection.

3.3 Raman spectroscopy

As mentioned in Section 3.2, XRD is the most widely used technique for identifying the phase and for studying phase changes in crystalline materials. However, XRD is considered to be insensitive to microscopic phase changes, which caused by oxygen displacement. This is because the X-ray scattering efficiency of oxygen is significantly lower than that of lanthanide ions, which have high atomic numbers. Moreover, it is more complicated when the dopant species have very similar XRD patterns due to the similarity in the crystal structure. Micro-Raman spectroscopy becomes useful in such cases because of its sensitivity.

The Raman scattering technique is vibrational molecular spectroscopy, which derives from an inelastic light scattering process. The photons from the laser interact with the molecules of the sample and are scattered inelastically. The scattered photons are collected and a spectrum is generated from the scattered photons. In general, a laser light (photon) interacting with molecules most commonly scatters elastically. This is called Rayleigh scattering. In Rayleigh scattering, Rayleigh scattered photons have the same energy (wavelength) as the incident photons. However, very few photons are inelastically scattered in which the scattered photons have different energies from that of the incident light. This is called Raman scattering.

With Raman scattering, in principle, the incident light interacts with molecular vibrations, phonons, or other excitations in the systems, resulting in the energy of the laser photons being shifted up or down. The photons' wavelength is either shifted higher or lower (red or blue shifted, respectively). The amount of energy lost is seen as a change in the energy of the incident photon. The loss of energy is characteristic of a particular bond in the molecule. This energy loss is directly related to the functional group, the structure of the molecule to which it is attached, the types of atoms in that molecule, and the molecule's environment. A Raman spectrum thus enables the identification of molecules and their functional groups with visible range light. This Raman spectroscopy technique, therefore, has been efficiently used as complementary to XRD

in studying phase identification.

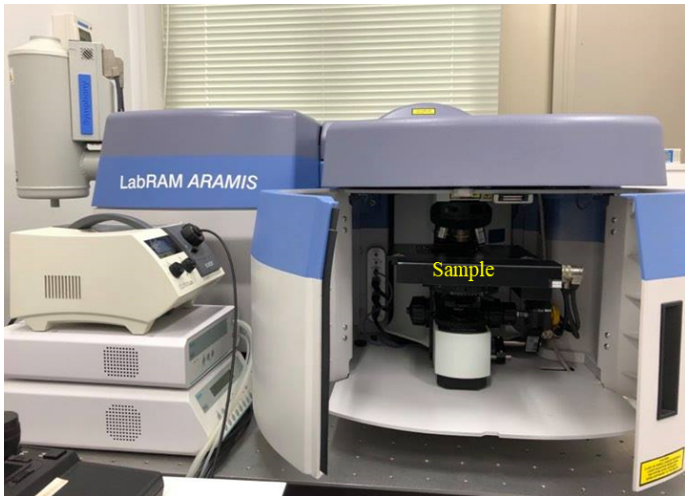

Figure 19. The image of LabRAM ARAMIS instruments used in this study.

In the present study, the Raman spectroscopy measurements were carried out for UO_2–$LnO_{1.5}$ and CeO_2–$LnO_{1.5}$ samples at room temperature. Raman spectra were obtained using LabRAM ARAMIS. The scattered Raman signals were analyzed in a backscattering geometry using a single monochromator spectrometer equipped with a CCD detector (microscope objective lens 20x). The LabRAM ARAMIS operated with a laser source emitting visible continuous laser radiation. Raman spectra of UO_2–$LnO_{1.5}$ samples were collected using He-Ne laser radiation (wavelength of 633 nm) without filter, confocal hole size of 100 µm, a grating of 600 g/mm (spectral range of 0–2856 nm), continuous mode time of 1 s, snapshot time of 10 s, and a number of accumulations of 10 times, at a frequency range from 200–1600 cm^{-1}. The sintered disk-shaped UO_2–$LnO_{1.5}$ pellets were used.

For CeO_2–$GdO_{1.5}$ samples, Raman spectra were acquired with 532 nm laser, a grating of 600 g/mm, confocal hole size of 100 µm, filter D2 (transparency of 1%) for CeO_2–$GdO_{1.5}$ samples, and confocal hole size of 30 µm, filter D3 (transparency of 0.1%) for CeO_2–$GdO_{1.5}$ samples, continuous mode time of 1 s, snapshot time of 3 s, and a number of accumulations of 5 times, over a frequency range of 50–2000 cm^{-1}. The sintered CeO_2–$LnO_{1.5}$ powder samples prepared for XRD measurements were also used here.

3.4 X-ray absorption fine structure (XAFS)

XAFS measurements were mainly performed at the beamline BL-27B station (energy range of 4–20 keV) of the Photon Factory in the High Energy Accelerator Research Organization (KEK, Japan). XAFS measurements were also performed at the beamline BL22XU station (energy range of 5–70 keV) in the Super Photon ring-8 GeV (SPring-8, Japan). In general, the X-ray absorption spectrum is typically divided into two regimes: the X-ray absorption near edge structure (XANES) and the extended X-ray absorption fine structure (EXAFS). XANES is used to determine the oxidation state of U and Ce in the samples because it is strongly sensitive to the formal oxidation state and coordination chemistry of the absorbing atom.

EXAFS is used to determine the interatomic distances, CN, and species of the neighbors of the absorbing atom. The continuous X-ray beam from synchrotron radiation was monochromatized by a double Si(111) crystal monochromator. The X-ray absorption measurements near the U L_3 edge, Gd L_3 edge, and Er L_3 edge of UO_2–$LnO_{1.5}$ solid solution samples were carried out at room temperature with synchrotron radiation in transmission modes. And, for CeO_2–$LnO_{1.5}$ samples, the X-ray absorption measurements near the Ce L_3, Gd L_3, and Er L_3 edges were carried out at room temperature with synchrotron radiation by both transmission and fluorescence modes. Step-scanning XAFS with transmission geometry was performed for the U L_3 edge (E_0 = 17.166 keV), Gd L_3 edge (E_0 = 7.243 keV), Er L_3 edge (E_0 = 8.358 keV), and Ce L_3 edge (E_0 = 5.600 keV). Figure 20 shows the schematics of XAFS measurements at the beamline BL-27B station.

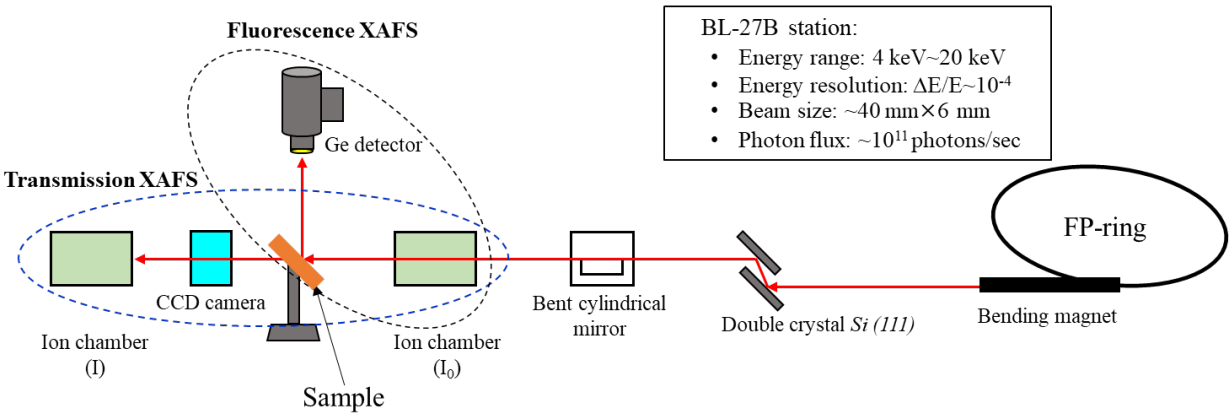

Figure 20. Schematics of XAFS measurement at the beamline BL-27B station.

The X-ray intensity incident on the sample (I_0) and the intensity transmitted through the sample (I) were measured. According to Beer's Law, the X-ray absorption is expressed as:

$$I = I_0 e^{-\mu t}, \tag{4}$$

where μ is the X-ray absorption coefficient, t is the sample thickness. The standard EXAFS equation is given by,

$$\chi(k) = \sum_j \frac{N_j e^{-2k^2\sigma_j^2} e^{-2R_j/\lambda(k)} f_j(k)}{kR_j^2} \sin[2kR_j + \delta_j(k)], \tag{5}$$

where $f_j(k)$ is backscattering amplitude for each of the N_j atoms in the jth shell neighboring absorption atom, N is the number of neighboring atoms, R_j is the distance to the neighboring atom, λ is the mean free path of the photo-electrons for inelastic scattering, σ^2 is the mean square radial displacement of the atom about R_j, $\delta_j(k)$ is the phase shift due to center atom.

The XAFS data were analyzed using WinXAS Ver. 3.2 developed by Resslert [1] to obtain EXAFS function, $k^3\chi(k)$, and the Fourier transform magnitude, $|FT(k^3\chi(k))|$ [2]. The structural parameters, such as CN, interatomic distances, and the Debye-Waller factor (DW) were determined by curve fitting analyses. The phase shift and back-scattering amplitude were calculated using FEFF ver. 8.4 [3].

3.5 Powder crystallinities and lattice parameters of UO_2–$LnO_{1.5}$ and CeO_2–$LnO_{1.5}$ solid solutions

(a) UO_2–$LnO_{1.5}$ solid solutions

Figure 21 shows the XRD patterns for UO_2–$LnO_{1.5}$, with the reflection positions of the single F-type phase UO_2 reported by Desgranges et al. [4] and the single C-type phases of $GdO_{1.5}$ and $ErO_{1.5}$ reported by Saiki et al. [5]. The F-type phase was detected for UO_2–$LnO_{1.5}$ for $LnO_{1.5}$ contents up to 40 mol %. These XRD patterns agreed well with literature patterns [6-9]. All peaks were indexed with the ICSD code 246851 of UO_2 (No.: 01-078-6742) [4]. All the diffraction peaks were assigned to the Miller indices (111), (200), (220), (311), (222), (400), (331), (420), (422), (511), (440), (531), (600), (620), (533), and (622) for the F-type structure. There were no peaks from the XRD patterns for the C-type structure of $GdO_{1.5}$ and $ErO_{1.5}$. Therefore, Gd and Er were dissolved in UO_2 and the dopant Gd and Er were mostly substituted for host U ions in the cation sublattice of the F-type structure below 40 mol % $LnO_{1.5}$.

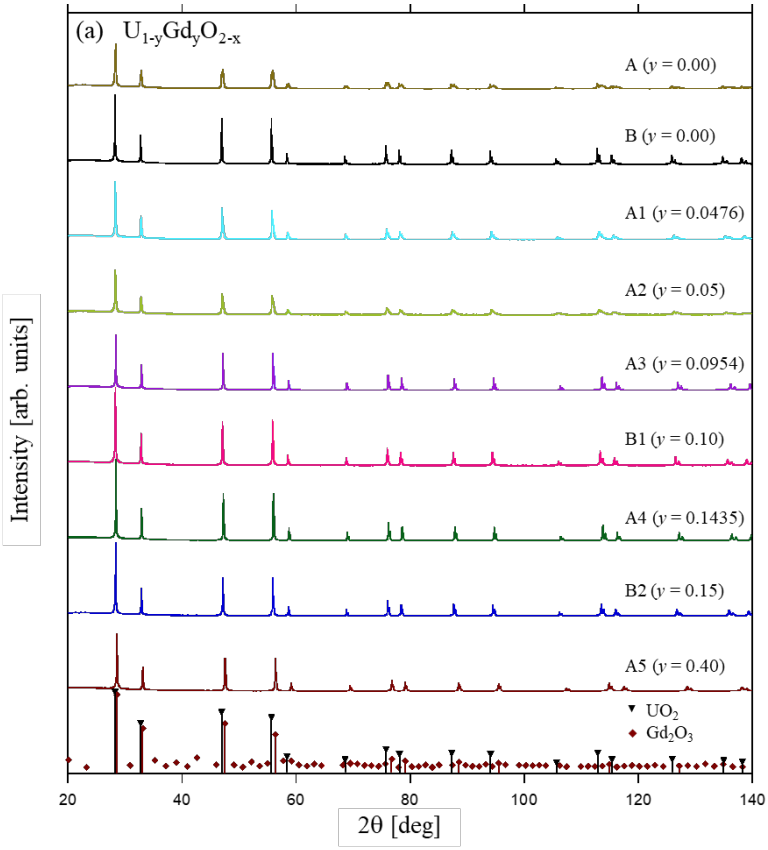

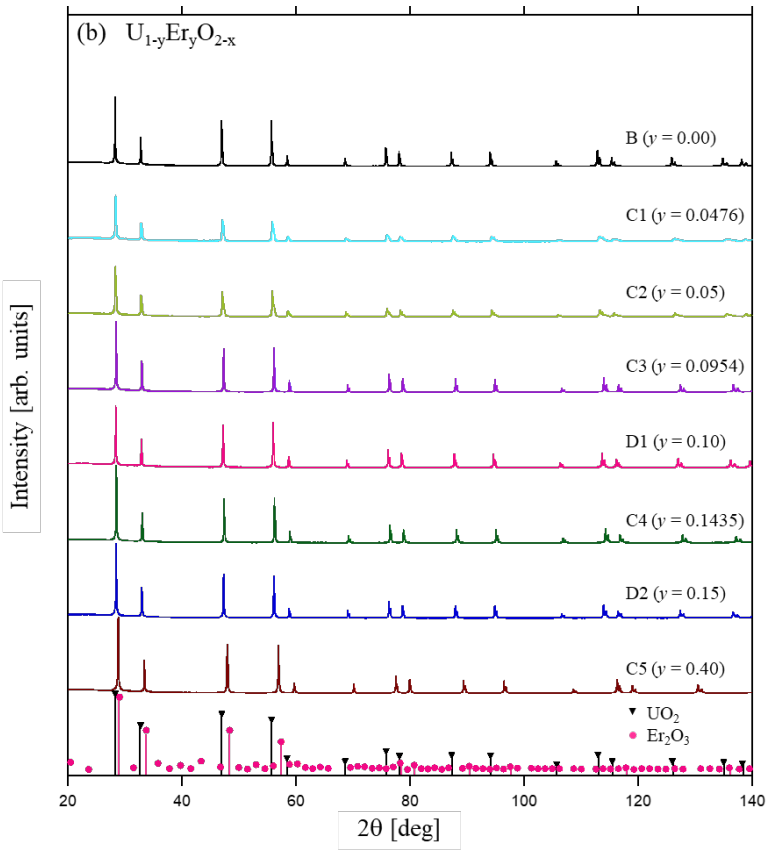

Figure 21. XRD patterns for (a) UO_2–$GdO_{1.5}$ and (b) UO_2–$ErO_{1.5}$ solid solution samples.

Figure 22 shows the XRD patterns of UO_2–$LnO_{1.5}$ in the high diffraction angle region of 85–100°. In samples A, A1, A2, C1, and C2, the second phase peaks were observed at high angles. In the diffraction pattern of sample A sintered in Ar, the broad diffraction peaks of a second phase, identified as U_4O_9 [10,11], were detected at 88° and 94.5°. These second phase peaks also appeared on the right of the diffraction peaks for samples A1 and C1 (UO_2–4.76 mol % $LnO_{1.5}$) and A2 and C2 (UO_2–5 mol % $LnO_{1.5}$).

The major diffraction peaks for UO_2–$LnO_{1.5}$ were shifted slightly to higher diffraction angles compared with those for pure UO_2. Thus, the lattice parameters of UO_2–$LnO_{1.5}$ decreased when $LnO_{1.5}$ was added to UO_2, and the decrease was proportional to the increase in $LnO_{1.5}$ content up to 40 mol % $LnO_{1.5}$. The diffraction peaks of samples A3 and C3 sintered in Ar were close to those of B1 and D1 sintered in Ar-10% H_2, and the peaks for samples A4 and C4 were close to those of and B2 and D2, respectively. Therefore, reducing conditions during sintering increased the lattice parameter of UO_2–$LnO_{1.5}$ solid solutions.

Rietveld refinement was performed using integrated X-ray powder diffraction software on high-resolution grazing angle XRD patterns collected at room temperature. Table 1 and Fig. 23 show the estimated lattice parameters of UO_2–$LnO_{1.5}$, together with literature data [7,12–14]. The lattice parameters of UO_2–$LnO_{1.5}$ decreased as the $LnO_{1.5}$ content increased to 40 mol %. The lattice parameters of UO_2–$ErO_{1.5}$ were smaller than those of UO_2–$GdO_{1.5}$ at the same $LnO_{1.5}$ concentration. Furthermore, the lattice sizes of the UO_2–$LnO_{1.5}$ samples sintered in Ar-10% H_2 were larger than those of the samples sintered in Ar.

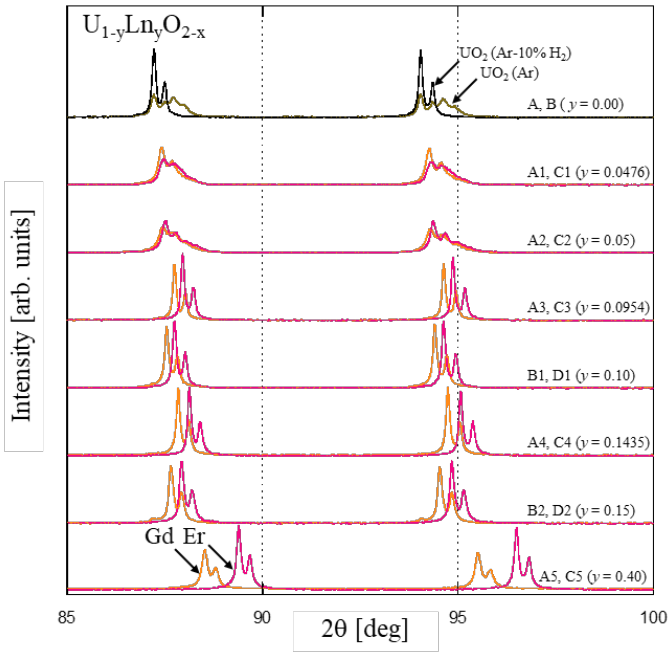

Figure 22. XRD patterns in the higher diffraction angle region from 85° to 100° for UO_2–$LnO_{1.5}$ solid solution samples (black and grey: UO_2; orange: UO_2–$GdO_{1.5}$; pink: UO_2–$ErO_{1.5}$).

The lattice parameters obtained from the refinement for UO_2–$LnO_{1.5}$ agreed well with the literature data [7,12–16]. The lattice parameter of a cubic solid solution varied nearly linearly with the increase of y (up to $y = 0.4$) and x in $U_{1-y}Ln_yO_{2-x}$. The lattice contraction factors, $\partial a/\partial y$, of UO_2–$GdO_{1.5}$ (–0.0156 nm for Ar and –0.0146 nm for Ar-10% H_2) obtained from Fig. 23 are close to –0.0162 nm reported by Fukushima et al. [12] and –0.0173 nm measured for the near stoichiometric samples (T-series) by Ohmichi et al. [13]. The lattice parameters of hypo-stoichiometric samples (G-series) are also given by Ohmichi et al. [13]; however, these values were not similar to our results. Likewise, for UO_2–$ErO_{1.5}$, the contraction factors for Ar and Ar-10% H_2 were –0.0263 and –0.0237 nm, respectively, which were close to those measured by Yamanaka et al. (–0.0270 nm [7]) and Kim et al. (–0.0264 nm [14]). These literature data were obtained for solid solutions with O/M ≈ 2.00.

The lattice parameter of UO_2–$GdO_{1.5}$ solid solution decreases as the O/M ratio increases or oxygen vacancy decreases [13,17], and the lattice contraction factor, $\partial a/\partial y$, for UO_2–$GdO_{1.5}$ depends on stoichiometry. For hypo-stoichiometric $U_{1-y}Gd_yO_{2-x}$, the contraction factor is much smaller than that of stoichiometric $U_{1-y}Gd_yO_{2.00}$ [13,17]. The larger lattice parameters of UO_2–$LnO_{1.5}$ sintered in Ar-10% H_2 compared with those of UO_2–$LnO_{1.5}$ sintered in Ar indicated that the samples sintered under more reducing conditions had a smaller O/M ratio than the samples sintered in Ar. However, the lattice parameters of UO_2–$LnO_{1.5}$ sintered in both atmospheres in this study were close and they were also close to the literature data for near-stoichiometric $U_{1-y}Ln_yO_{2.00}$ [7,12–14]. Thus, the UO_2–$LnO_{1.5}$ solid solutions formed in this study were near-stoichiometric $U_{1-y}Ln_yO_{2.00}$. Although UO_2–$LnO_{1.5}$ sintered in Ar-10% H_2 had a smaller O/M ratio compared with UO_2–$LnO_{1.5}$ sintered in Ar, I estimated the O/M ratios of the solid solution samples in this study to be close to 2.00.

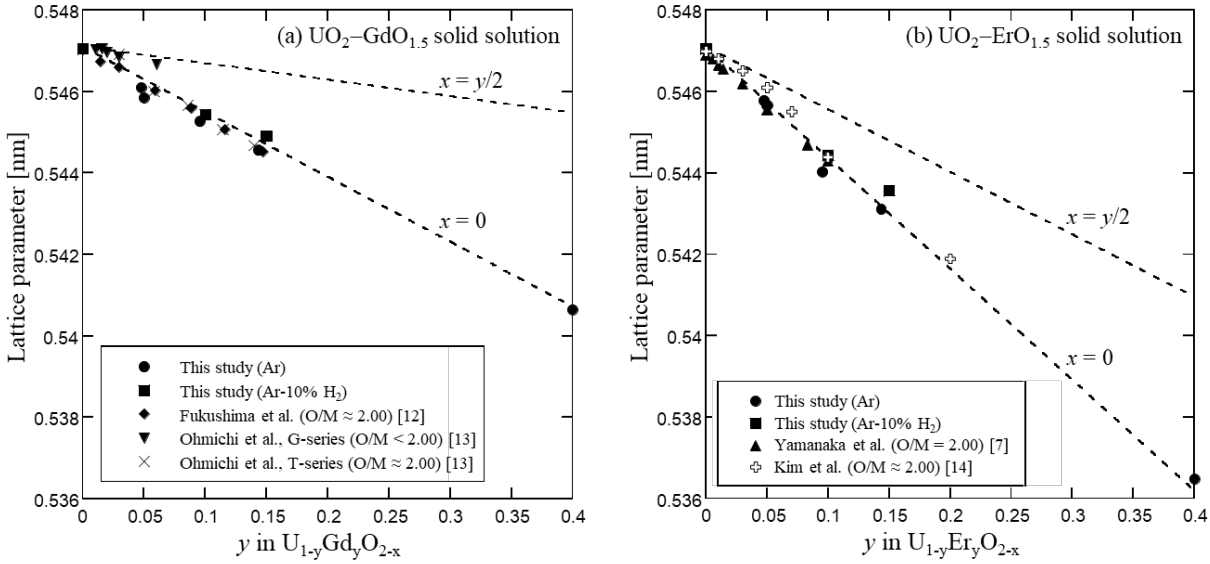

Figure 23. Lattice parameters for UO_2–$LnO_{1.5}$ as a function of $LnO_{1.5}$ content compared with other experimental data. Dashed lines are plotted according to Eq. (6) [13].

When Ln^{3+} ions are substituted for U^{4+} ions in the host cation sites, either oxygen vacancies are created or some of the U^{4+} are oxidized to U^{5+} or U^{6+} ions to maintain electrical neutrality. The type of solid solution, i.e., stoichiometry or non-stoichiometry, formed possibly depends on the oxygen partial pressure during sintering. In the case of the creation of the oxygen vacancies, if U ions in the UO_2–$LnO_{1.5}$ remain in the U^{4+} state, the charge balance in UO_2–$LnO_{1.5}$ solid solutions will be maintained by oxygen vacancies. Under full reduction, when Ln^{3+} ions are substituted for U^{4+} ions, the number of oxygen ions decreases leading to the formation of oxygen vacancies. In fact, according to literature relevant to $U_{1-y}Ln_yO_{2-x}$, full reduction, however, seems to be difficult, that is $x < y/2$ for this solid solution because UO_2 is easily oxidized. In the latter case, i.e., for more oxidizing conditions, the addition of $LnO_{1.5}$ into UO_2 could also lead to the existence of U^{5+} or U^{6+} ions. The change in the lattice parameter of these non-stoichiometric oxides can be estimated by assuming that Ln^{3+} is substituted for U^{4+} randomly. Another assumption is that the oxygen vacancies around U^{4+} decrease the average CN around the U atoms. Considering this effect, Ohmichi et al. [13] calculated the lattice parameter, a, of $(U^{4+}_{1-2y+2x}U^{5+}_{y-2x}Ln^{3+}_{y})O_{2-x}$ with

$$a = \frac{4}{\sqrt{3}}\left\{(1-2y+2x)r_{U^{4+}} + (y-2x)r_{U^{5+}} + yr_{Ln^{3+}} + \frac{2-x}{2}r_{O^{2-}} + \frac{x}{2}r_{OV^{*}}\right\}. \quad (6)$$

The ionic size of these species in Eq. (6) would determine the lattice size of a solid solution. In other words, ionic radii of the host U ion (r_U), the dopant Ln ion (r_{Ln}), the oxygen ion (r_O), and the oxygen vacancy (r_{OV^*}) determine the lattice parameters of UO_2–$LnO_{1.5}$ samples. The ionic radii used in this study are summarized in Table 6. Here, the corrected radius of the oxygen vacancy is $r_{OV^*} = 0.109 \pm 0.005$ nm and much smaller than that of oxygen [13]. The cation ionic radii, $r_{U^{4+}}$, $r_{U^{5+}}$, $r_{Gd^{3+}}$, and $r_{Er^{3+}}$, decrease as the CN decreases [18]. This effect is reflected in r_{OV^*} [13]. According to Eq. (6), the Ln^{3+} content dependence of lattice parameter, $\partial a/\partial y$, was negative irrespective of y and the lattice parameter decreased as x increased. The lattice parameters for $x = y/2$ and $x = 0$ are represented by the dashed lines in Fig. 23. The

reduction in the lattice parameters of UO_2–$LnO_{1.5}$ samples with increasing $LnO_{1.5}$ content was observed in this study. Similar results are reported earlier for Dy doped UO_2 in the literature [19], where the calculated lattice volume decreases with increasing Dy content in the UO_2 matrix. In addition, the change in structural properties for different Ln atoms doped UO_2 lattice is evaluated by Vazhappilly et al. [20]. In this literature, the reduction in the volume per unit lattice of these samples is explained by the lanthanide contraction. As given in Table 6, the Shannon ionic radius of Er^{3+} is closer to U^{4+} than that of Gd^{3+}. Therefore, the smaller lattice parameter of UO_2–$ErO_{1.5}$ compared to UO_2–$GdO_{1.5}$ at the same $LnO_{1.5}$ content is also expected due to the lanthanide contraction. On the other hand, the larger ionic radius of Gd^{3+} than U^{4+} will tend to increase the lattice parameter of UO_2–$GdO_{1.5}$. However, the presence of U^{5+}, which has a smaller ionic radius than that of U^{4+} in the solid solution, resulted in the reduction in the lattice parameter of UO_2–$GdO_{1.5}$ solid solution.

Although it is difficult to measure the accurate O/M ratio of the rare-earth-doped uranium dioxides, Ohmichi et al. [13] deduced the relationship between the lattice parameter, a, and the value of x in $U_{1-y}Gd_yO_{2-x}$ as $\partial a/\partial x = -0.024 \pm 0.006$ nm. Using this relationship and substituting the lattice parameters and the values of y into Eq. (6), the O/M ratios of UO_2–$LnO_{1.5}$ were estimated as 2.00, 1.990, 1.981, 1.986, 1.988, 1.992, 2.00, 1.992, and 2.002 for samples A, A1, A2, A3, A4, A5, B, B1, and B2, respectively. Because samples B, B1, and B2 were sintered in Ar-10% H_2, oxygen was probably lost. However, the O/M ratios of all the samples were close to 2.00, which indicated that the number of oxygen atoms changed by a small amount in the present experimental conditions.

Table 6. Ionic radii used in the present study

Ion (CN)	Radius [nm]	Reference
U^{4+} (8)	0.1001	[12]
U^{5+} (8)	0.0880	[12]
Gd^{3+} (8)	0.1053	[27]
Er^{3+} (8)	0.1004	[27]
O^{2-} (4)	0.1368	[12]

(b) CeO_2–$LnO_{1.5}$ solid solutions

The XRD patterns for CeO_2–$LnO_{1.5}$ oxides are shown in Fig. 24. The single F-type phase was detected for CeO_2–$LnO_{1.5}$ at the range of $LnO_{1.5}$ content from 0 to 40 mol % $LnO_{1.5}$. These XRD patterns agreed well with those given in the literature [21,22]. All the diffraction peaks can be assigned to the Miller indices (111), (200), (220), (311), (222), (400), (331), (420), (422), (511), (440), (531), (442), (620), and (533) for the F-type structure. There were no peaks from the XRD pattern for the C-type structure of Ln_2O_3 for $Ce_{1-y}Gd_yO_{2-y/2}$ samples with $y \leq 0.15$. This indicated that the dopant Gd ion is fully substituted for the host Ce ion on the cation sublattice of the F-type structure below 15 mol % of $LnO_{1.5}$. Although the peaks for the C-type structure of Ln_2O_3 appeared and the broad peaks formed in CeO_2–40 mol % $LnO_{1.5}$ samples, the F-type lattice was mainly retained until 40 mol % of $LnO_{1.5}$.

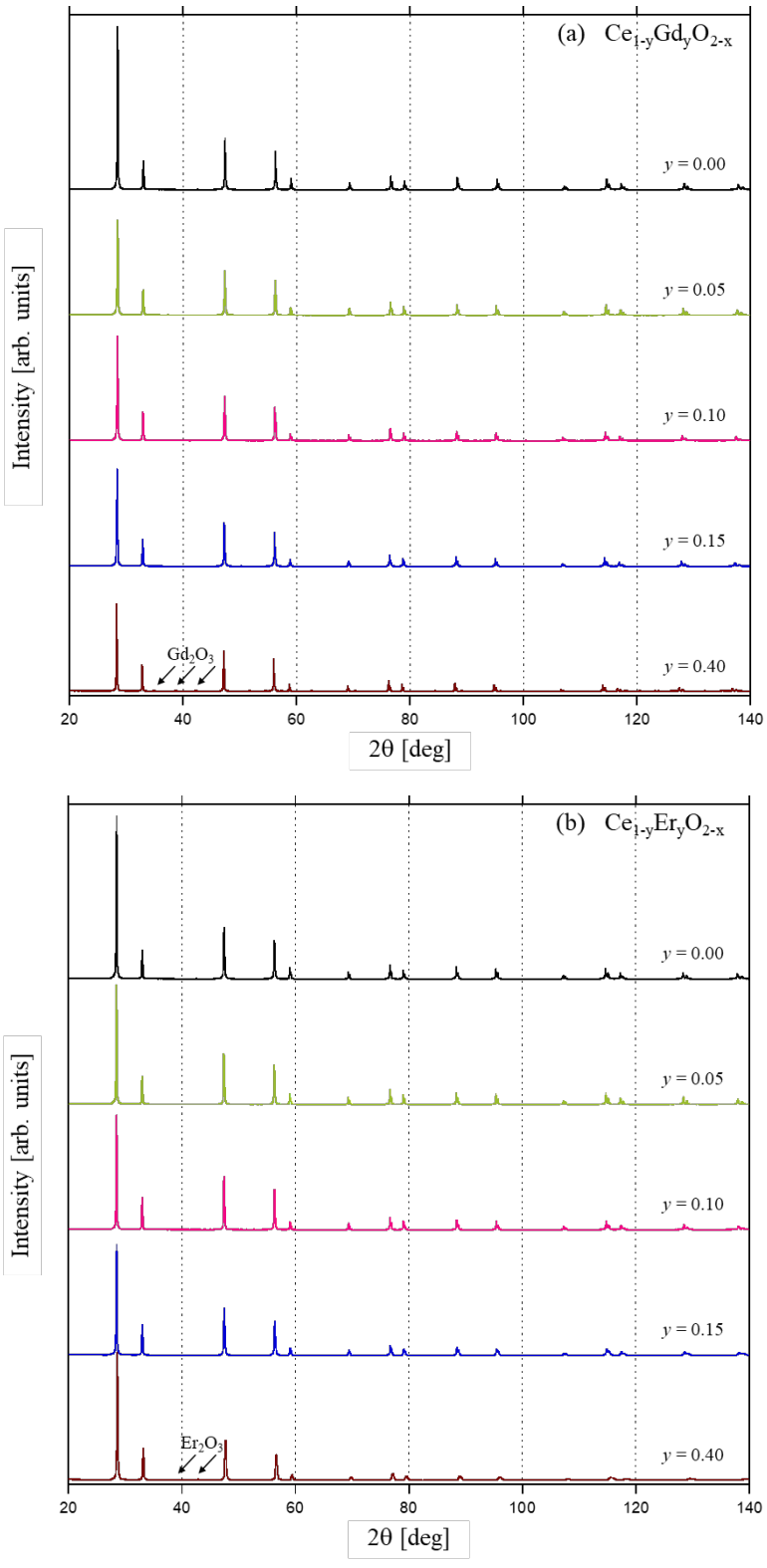

Figure 24. XRD patterns for (a) CeO_2–$GdO_{1.5}$ and (b) CeO_2–$ErO_{1.5}$ solid solution samples.

Figure 25 shows the XRD patterns of CeO_2–$LnO_{1.5}$ at a high diffraction angle region from 85–100°. The diffraction peaks for CeO_2–$GdO_{1.5}$ slightly shifted to a lower diffraction angle compared with those for pure CeO_2 when $GdO_{1.5}$ content increased. Whereas those of CeO_2–$ErO_{1.5}$ slightly shifted to higher

diffraction angles. It is obvious that the position of diffraction peaks is related to the lattice spacing, *d*, in crystalline samples which determines the crystal lattice size of materials. The trend of the shift to lower angles illustrates that the lattice parameters of CeO_2–$GdO_{1.5}$ increased when $GdO_{1.5}$ is added.

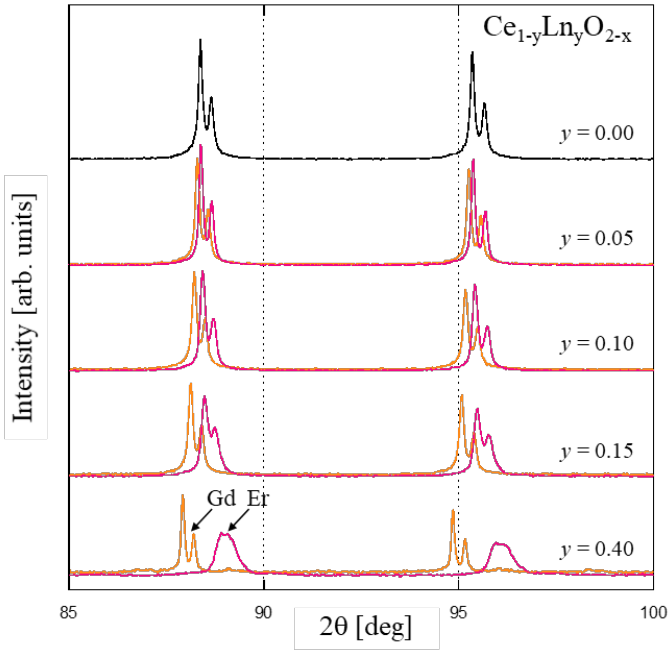

Figure 25. XRD patterns in the higher diffraction angle region from 85° to 100° for CeO_2–$LnO_{1.5}$ solid solution samples (black: CeO_2, orange: CeO_2–$GdO_{1.5}$, purple: CeO_2–$ErO_{1.5}$).

A simple method for the determination of lattice parameters of the crystals with known crystal structure from XRD data was also performed. This estimation is based on the Nelson-Riley extrapolation function and the least-squares analysis. In cubic systems, such as simple cubic, body-centered cubic, and face-centered cubic lattices, the interplanar spacing is given by the following expression,

$$d_{hkl} = \frac{a}{\sqrt{h^2 + k^2 + l^2}}. \quad (7)$$

In the above equation, the term *a* is the FCC lattice parameter, and *h,k,l* are the Miller indices of a family of atomic-planes *(hkl)* where *h,k,l* are three integers. The lattice parameter, *a*, of CeO_2–$LnO_{1.5}$ solid solutions was determined by Eq. (7). It is considered that the lattice parameter can be plotted against $\cos^2\theta$, $\cos^2\theta/\sin\theta$, and also it is proportional to the Nelson-Riley extrapolation function of $\cos^2\theta/\sin\theta + \cos^2\theta/\theta$. The following function of θ is plotted (on the X-axis) against the lattice parameter (Y-axis) estimated at a given diffraction angle θ.

$$N - R\ extrapolation\ function = cos^2\theta/sin\theta + cos^2\theta/\theta, \quad (8)$$

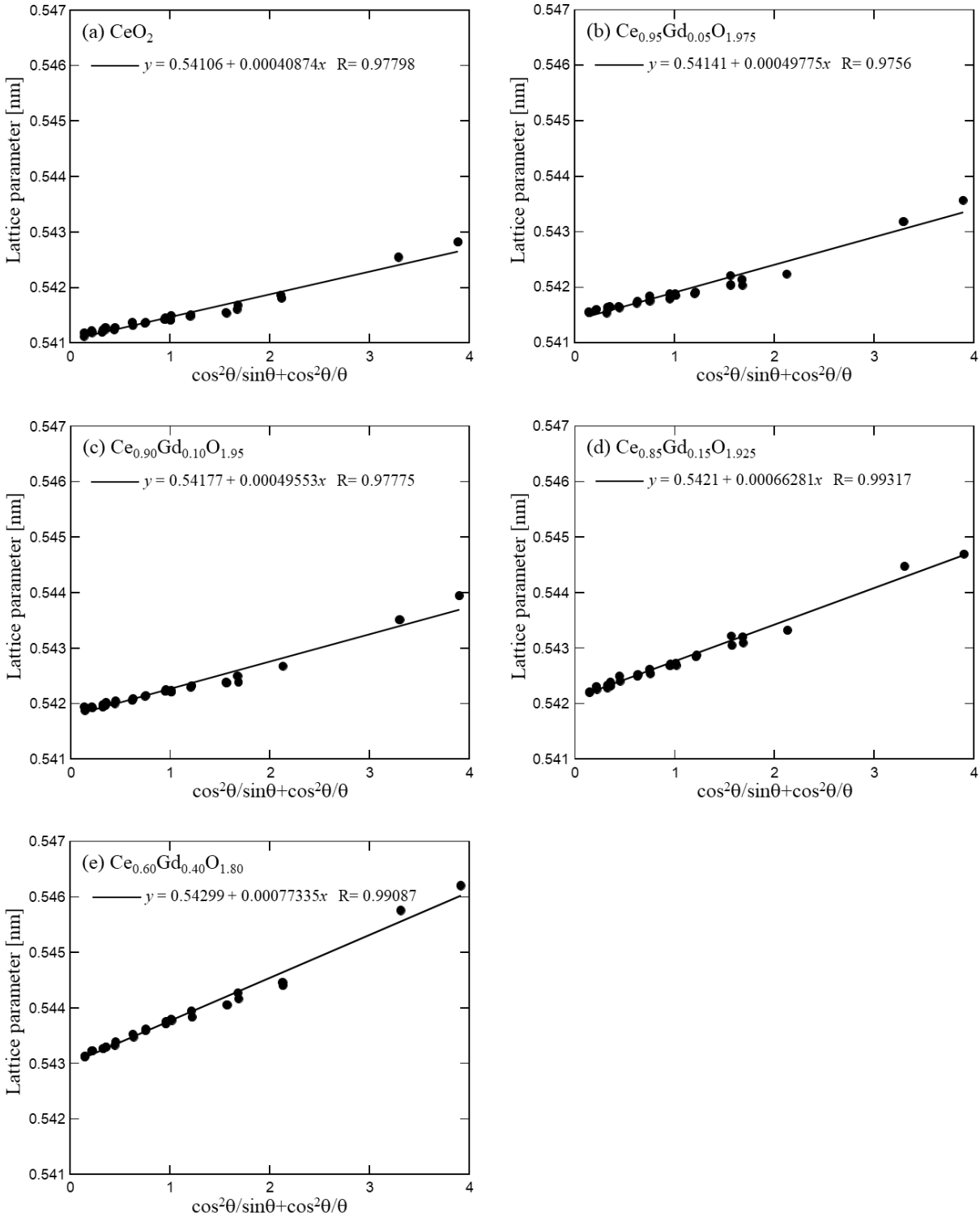

Figure 26. The estimated lattice parameter for CeO_2–$GdO_{1.5}$ as a function of Nelson-Riley extrapolation function.

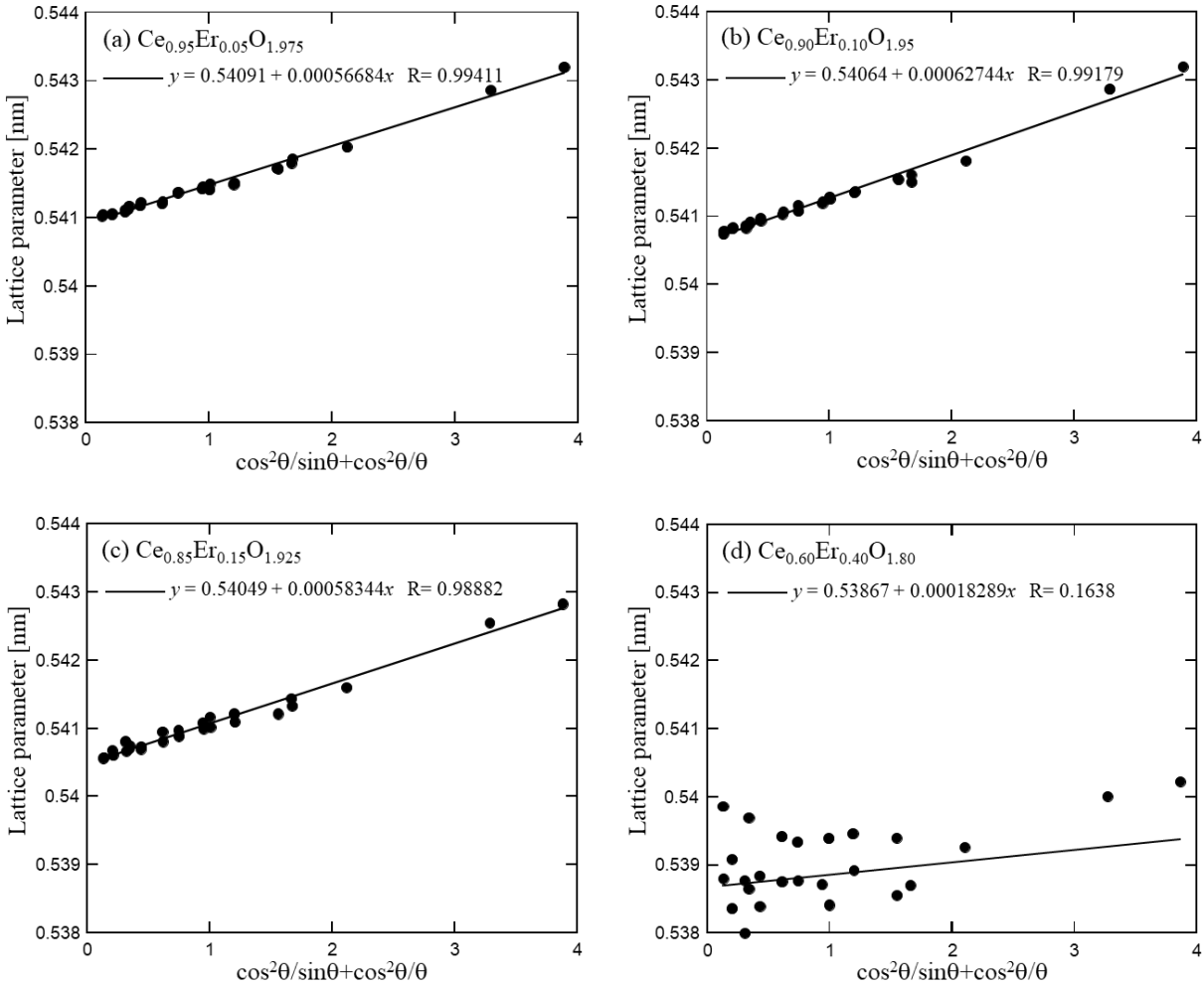

Figure 27. The estimated lattice parameter for CeO_2–$ErO_{1.5}$ as a function of Nelson-Riley extrapolation function.

The estimated lattice parameters for CeO_2–$LnO_{1.5}$ as a function of the Nelson-Riley extrapolation function are plotted in Figs. 26-27. The extrapolated values for the lattice parameter of CeO_2–$LnO_{1.5}$ by the Nelson-Riley extrapolation function and the least-squares analysis were close to those of Rietveld refinement analysis, which are given in Table 3. The lattice parameters estimated by Rietveld refinement analyses for CeO_2–$LnO_{1.5}$ are given in Table 3 and plotted in Fig. 28 together with those from the available literature data [21–24].

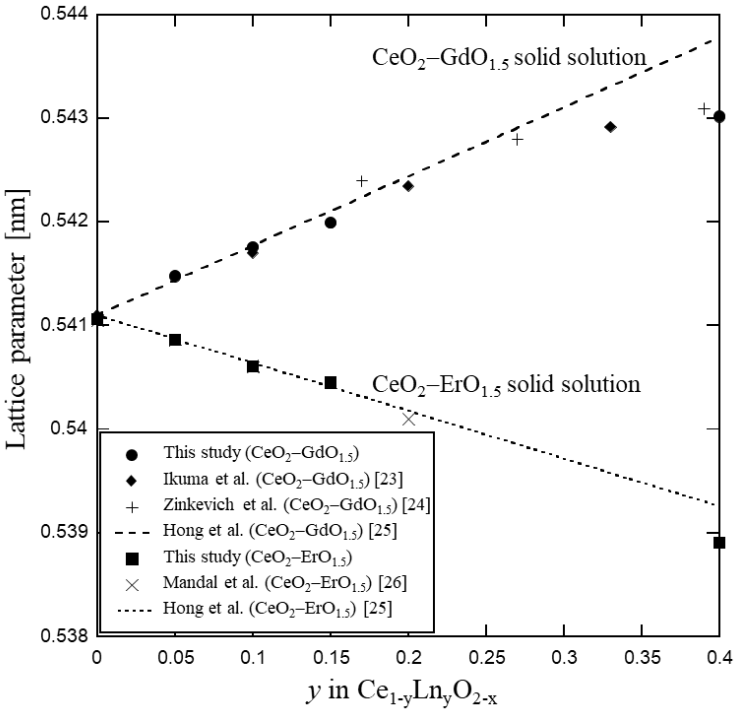

Figure 28. Lattice parameter data obtained for CeO_2–$LnO_{1.5}$ compared to other experimental data as a function of $LnO_{1.5}$ content.

As shown in Fig. 28, our results were in good agreement with the available literature data [23–26]. The lattice parameters of CeO_2–$GdO_{1.5}$ were higher than that of CeO_2 powder (standard data for CeO_2 powder is 0.5411 nm). The lattice parameters of CeO_2–$GdO_{1.5}$ increased gradually with increasing $GdO_{1.5}$ content up to 40 mol %. In contrast, the lattice size of CeO_2–$ErO_{1.5}$ dropped when $ErO_{1.5}$ increased. These experimental results can be explained as follows:

For the CeO_2–$LnO_{1.5}$ solid solution, assuming that Shannon's ionic radius of O^{2-} is equal to that of oxygen vacancy, which is randomly distributed on anion sites, the lattice parameter of $Ce_{1-y}Ln_yO_{2-y/2}$ solid solution is,

$$a = \frac{4}{\sqrt{3}}\{(1-y)r_{Ce^{4+}} + yr_{Ln^{3+}} + r_{O^{2-}}\}, \quad (9)$$

which increases with increasing $LnO_{1.5}$ content. Here, cation ionic radii, $r_{Ce^{4+}}$, $r_{Gd^{3+}}$ and $r_{Er^{3+}}$ vary as a function of oxygen CN [18]. Furthermore, EXAFS measurement shows that the interatomic distances, $d_{cation-anion}$, of Ce–O and Gd–O in $Ce_{1-y}Gd_yO_{2-y/2}$ solid solution decrease with increasing $GdO_{1.5}$ content [27,28]. This was also confirmed by our results of XAFS measurements, which are given in Section 3.7. Thus, it is oversimplified and inconsistent that the lattice parameter of $Ce_{1-y}Gd_yO_{2-y/2}$ oxide is estimated from the following equation,

$$a = \frac{4}{\sqrt{3}}\{d_{cation} - d_{anion}\}. \quad (10)$$

On the other hand, Hong et al. [22] derived the empirical formulation for the lattice parameter of F-type $Ce_{1-y}Ln_yO_{2-y/2}$ oxide as follows:

$$a = \frac{4}{\sqrt{3}}\left\{(1-y)r_{Ce^{4+}} + yr_{Ln^{3+}} + \frac{2-0.5y}{2}r_{O^{2-}} + \frac{0.5y}{2}r_{OV^*}\right\} \cdot 0.9971. \quad (11)$$

The ionic size of these species in Eq. (11) would determine the lattice parameter. In other words, ionic radii of the host ion (r_{Ce}), the dopant ion (r_{Ln}), the oxygen ion (r_O), and the oxygen vacancy (r_{OV}) determine the lattice size of a solid solution. The ionic radii in Eq. (11) [25] are given in Table 7. For a given solid solution, the radius of oxygen vacancy is assumed to be a unique value with respect to dopant concentration and dopant cation radius. The corrected radius of oxygen vacancy is determined as $r_{OV^*} = 0.1164$ nm [25]. The calculated results by Hong [25] and Kim et al. [29] were consistent with the experimental ones. Therefore, it is supposed that Ln^{3+} ions and oxygen vacancies are not randomly distributed on cation and anion sites, respectively, but defect clusters, e.g. Ln^{3+}–V_O–Ln^{3+}, might be formed in CeO_2–$LnO_{1.5}$ solid solution [27,30]. And, the radius of oxygen vacancy is considered to be smaller than that of oxygen.

Thus, the increase in lattice parameters of CeO_2–$GdO_{1.5}$ with increasing $GdO_{1.5}$ content can be considered to be due to the replacement of Gd^{3+} ion having a larger ionic radius than that of Ce^{4+} ion into CeO_2 structure. When $GdO_{1.5}$ dissolves into CeO_2, Gd^{3+} ions occupy Ce^{4+} sites, and oxygen vacancies are formed. The ionic radii of Gd^{3+} and Ce^{4+} ions for both CN = 8 are 0.1053, and 0.097 nm, respectively. Therefore, based on the consideration of relative ionic radii, the increase in the cubic lattice parameters of CeO_2–$GdO_{1.5}$ solid solutions can be explained. According to this idea, because Gd^{3+} ion has a larger ionic radius than that of Ce^{4+} ion, the lattice parameter increases with $GdO_{1.5}$ addition. Therefore, the ionic repulsion between excess anions seems to be a plausible reason for the increase in lattice parameters of CeO_2–$GdO_{1.5}$ solid solutions with $GdO_{1.5}$ addition. And, the decrease in lattice parameter of CeO_2–$ErO_{1.5}$ while $ErO_{1.5}$ content increased can be mostly attributed to the increase of oxygen vacancies, which is caused by the incorporation of the dopant Er in the CeO_2 lattice. In most cases, when $LnO_{1.5}$ is doped into CeO_2 lattice, phase changes from F-type to C-type when $LnO_{1.5}$ content is higher than 40 mol % [26]. Lattice parameter and other thermo-physical properties of the sample tend to change with composition as well. From the experimental results, it becomes even more interesting that when the dopant Ln^{3+} ion is slightly bigger in size than the host Ce^{4+} ion, the dopant ion tries to expand the lattice, whereas the oxygen vacancies tend to shrink it.

I assumed that the substitution of Ln^{3+} ion for Ce^{4+} ion takes place randomly and the presence of oxygen vacancies around the Ce^{4+} ion results in the reduction in the average coordination number around the Ce atoms. The change in coordination number of the nominal composition $Ce_{1-y}Ln_yO_{2-y/2}$ is given by the following equation based on the random model,

$$CN(Ln^{3+}) = 8 - 2x = 4 \cdot O/M. \quad (12)$$

Table 7. Cation ionic radii with different oxygen CN [18]

Ion	Charge	Coordination number (CN)	Crystal radius [nm]	Ionic radius [nm]
Ce	3	6	0.115	0.101
		7	0.121	0.107
		8	0.1283	0.1143
		9	0.1336	0.1196
		10	0.139	0.125
		12	0.148	0.134
	4	6	0.101	0.087
		8	0.111	0.097
		10	0.121	0.107
		12	0.128	0.114
U	3	6	0.1165	0.1025
	4	6	0.103	0.089
		7	0.109	0.095
		8	0.114	0.100
		9	0.119	0.105
		12	0.131	0.117
	5	6	0.090	0.076
		7	0.098	0.084
	6	2	0.059	0.045
		4	0.066	0.052
		6	0.087	0.073
		7	0.095	0.081
		8	0.100	0.086
Gd	3	6	0.1078	0.0938
		7	0.100	0.100
		8	0.1053	0.1053
		9	0.1107	0.1107
Er	3	6	0.103	0.089
		7	0.1085	0.0945
		8	0.1144	0.1004
		9	0.1202	0.1062
O	-2	4	0.1240	0.1380

3.6 Raman spectra of UO_2–$LnO_{1.5}$ and CeO_2–$LnO_{1.5}$ solid solutions

(a) UO_2–$LnO_{1.5}$ solid solutions

Figure 29 shows the changes in the Raman spectra of UO_2–$LnO_{1.5}$ over the frequency range of 200–1300 cm^{-1} as a function of $LnO_{1.5}$ content. The Raman spectrum of pure UO_2 showed two fundamental vibrational peaks corresponding to $UO_{2.00}$. The first peak appeared at 445 cm^{-1} (band (1) in Fig. 29 (a)). This peak was assigned to the triply degenerate T_{2g} Raman-active vibration for the U-O symmetric stretching mode, which arises due to oxygen-breathing vibrations around U^{4+} in the fluorite structure [31,32]. And the second peak appeared at around 1150 cm^{-1} (band (3) in Fig. 29 (a)). This peak was attributed to overtone 2L-O of the

first order longitudinal optical L-O at 575 cm^{-1} phonon mode (band (2) in Fig. 29 (a)) [33,34]. The Raman spectrum of UO_2 agreed well with those of literature [35–37].

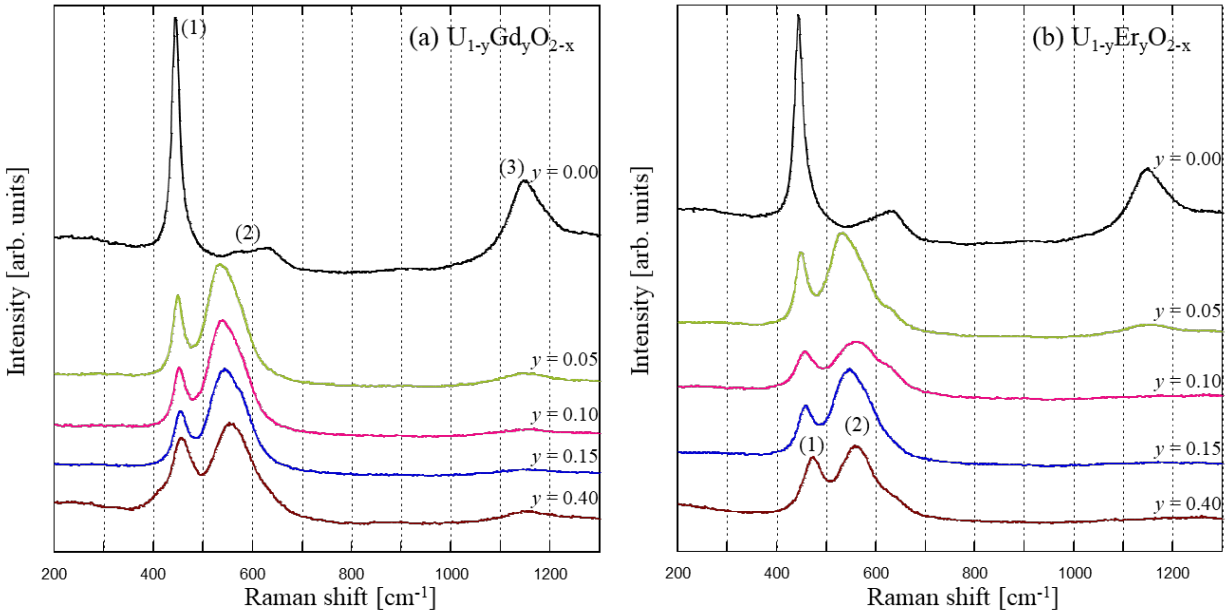

Figure 29. Raman spectra of UO_2–$LnO_{1.5}$ samples as a function of $LnO_{1.5}$ content.

In the Raman spectra of UO_2–$LnO_{1.5}$ samples, the broad peaks noted by two peaks were detected at around 455 cm^{-1} and 550 cm^{-1}. These scattering peaks were shifted slightly to higher frequencies (higher energies, or lower wavelengths) compared with that of pure UO_2 as $LnO_{1.5}$ content increased up to 40 mol %. This observation indicated that the peak at 445 cm^{-1} of UO_2 was split into the broad peaks at 455 cm^{-1} and 550 cm^{-1} when $LnO_{1.5}$ is added into UO_2. These broad peaks were substantially different from those of UO_2 and were close to those of U_4O_9 at 455 cm^{-1} (band (1) in Fig. 29 (b)), and 630 cm^{-1} (band (2) in Fig. 29 (b), identified as A_{1g} stretch) [37], suggesting that the oxidation state of U in UO_2–$LnO_{1.5}$ system was not solely tetravalent U^{4+}, however, some U^{4+} ions were oxidized to U^{5+} or U^{6+} ions. This was also confirmed by XAFS results in Section 3.7. The changes in the Raman spectra for UO_2–$LnO_{1.5}$ were similar to the results observed for hyper-stoichiometric UO_{2+x} due to the defects introduced by hyper-stoichiometric oxygen [36,37], and for La-doped UO_2 due to the distortion of lattice structure induced by La doping [38]. The Raman spectra of UO_2–$GdO_{1.5}$ (Fig. 29 (a)) were similar to those of the literature [39]. In addition, the peak of band 1 at 445 cm^{-1} in Raman spectra of UO_2–$LnO_{1.5}$ specimens shifted to higher wavenumbers is accompanied by a remarkable decrease in intensity as the $LnO_{1.5}$ content increased. Especially the intensities of the peaks at 1150 cm^{-1} were very weak compared with that of UO_2. This observation indicated the degradation of the lattice structure in the fluorite structure UO_2–$LnO_{1.5}$ due to the dopant $LnO_{1.5}$. A shift in the T_{2g} and 2L-O modes to higher wavenumbers caused by the contraction of the UO_2–$LnO_{1.5}$ lattices, which can be attributed to the formation of oxygen vacancies to maintain electrical neutrality when $LnO_{1.5}$ is added into UO_2. Moreover, the shift in the T_{2g} and 2L-O modes of UO_2–$ErO_{1.5}$ seemed to be bigger than those of UO_2–$GdO_{1.5}$ at the same $LnO_{1.5}$ content. These results were consistent with the changes in lattice

parameters of UO_2–$LnO_{1.5}$, where their lattice parameters decreased as $LnO_{1.5}$ content increased, and the UO_2–$ErO_{1.5}$ lattice parameters were smaller than those of UO_2–$GdO_{1.5}$.

(b) CeO_2–$LnO_{1.5}$ solid solutions

Figure 30 shows the changes in the Raman spectra for CeO_2–$LnO_{1.5}$ over the frequency range of 100–1200 cm^{-1} as a function of $LnO_{1.5}$ content. Pure CeO_2 showed only a first order Raman peak at around 465 cm^{-1}. It is known that fluorite structure CeO_2 has only a single allowed Raman mode with a frequency of 465 cm^{-1}, which can be assumed as symmetric F_{2g} breathing mode of the O atoms around each cation. The Raman active mode at 465 cm^{-1} involved the vibration of the eight surrounding oxygen atoms with the center Ce atom. Similarly, the only first order band was observed in the CeO_2–$GdO_{1.5}$ samples in the present study. The Raman spectrum for Gd_2O_3 was not observed in the present study. However, the result from [40] shows that the C-type for Gd_2O_3 is observed for CeO_2–$GdO_{1.5}$ with $GdO_{1.5}$ content ≥ 80% at ~354 cm^{-1}. The F_{2g} Raman peak (~465 cm^{-1}) mainly existed in the range of y = 0.0–0.4. The existence of only F_{2g} Raman peak indicated that the F-type lattice in CeO_2–$GdO_{1.5}$ was maintained up to 40 mol % $GdO_{1.5}$. The Raman spectra and the mode frequencies of CeO_2–$GdO_{1.5}$ in the present study agreed quite well with the reported values in the literature [40,41].

As shown in Fig.30, it was observed that when the $GdO_{1.5}$ content doping into CeO_2 lattice increased, the Raman spectra changed considerably with an increase in width and a decrease in intensity of the peak at 465 cm^{-1}. The intensity of the peak depends on the number of oxygen vacancies [41]. In other words, when $GdO_{1.5}$ is doped into CeO_2, oxygen vacancies are formed. The increase of oxygen vacancies, namely the reduction in average oxygen CN around Ce atoms due to the addition of $GdO_{1.5}$ led to the reduction in intensity.

In addition, Raman spectra peaks for CeO_2–$GdO_{1.5}$ slightly shifted to lower frequencies (lower energies, or higher wavelengths) compared with those for pure CeO_2 when $LnO_{1.5}$ content increased up to 15 mol %. This trend is called red shift. This slight red shift was in good agreement with the results reported by Banerji [40] and Bridge et al. [41]. For CeO_2–40 mol % $GdO_{1.5}$ sample, the Raman spectrum peak significantly shifted to a higher frequency (blue shift). As the mount of $GdO_{1.5}$ increases, this blue shift is also experimentally confirmed up to the addition of 70 mol % $GdO_{1.5}$ [40]. As mentioned in Section 3.6, when $GdO_{1.5}$ is doped into CeO_2 lattice, oxygen vacancies are simultaneously generated to keep electrical neutrality. The presence of oxygen vacancies resulted in the reduction in oxygen CN around Ce atoms, which can induce some softening effect in the Ce–O vibrational mode. This resulted in a red shift when $LnO_{1.5}$ content increased. When the $GdO_{1.5}$ content in the CeO_2–$GdO_{1.5}$ system increases, the lattice size becomes bigger, which consequently results in a blue shift. The blue shift is observed when the $LnO_{1.5}$ content is more than 30 mol % [40]. Therefore, the change in the Raman shift can be attributed to the cumulative effects of the reduction in CN and the expansion of the lattice size [26].

In the CeO_2–$ErO_{1.5}$ samples (y = 0.05–0.15), the Raman spectra changed with the appearance of peaks at about 260 cm^{-1}, 500 cm^{-1}, 680cm^{-1}, and 960 cm^{-1}. The first order Raman peak at around 465 cm^{-1} disappeared in CeO_2–$ErO_{1.5}$ samples. Moreover, there were the second order spectra in CeO_2–$ErO_{1.5}$ samples noted by the appearance of peaks at around 960 cm^{-1}. Our results are different from those of Mandal et al. [26]. In that literature, the F_{2g} Raman peak (~465 cm^{-1}) existed in the range of y = 0–0.7, which means that F-type lattice is retained until the addition of 70 mol% $ErO_{1.5}$. And, the C-type for Er_2O_3 is observed for CeO_2–$ErO_{1.5}$ with $ErO_{1.5}$ content > 70% at ~375 cm^{-1} and ~650 cm^{-1}. When $ErO_{1.5}$ is doped into CeO_2, the translational symmetry of the crystal is lost due to the formation of oxygen vacancies and lattice defects. Thus, the phonons contribute to the optical spectra, thereby leading to broad peaks and weak intensity bands [26]. My results showed the peaks with broadened shoulders, those can be attributed to the Er–O complexation within the system. These results can be considered to be due to the poor homogeneity and crystallinity in CeO_2–$EO_{1.5}$ solid solution.

Although the low intensity of CeO_2–40 mol % $ErO_{1.5}$ made it difficult to determine, the trend of the peak moving to higher frequencies or wavenumbers with increasing $ErO_{1.5}$ content can be seen up to the addition of 40 mol% $ErO_{1.5}$. All of the peaks showed that when $ErO_{1.5}$ content in CeO_2–$ErO_{1.5}$ solid solution increased, the intensity of the peaks decreased and the peaks shifted toward higher frequencies (blue shift). It was also confirmed by Mandal et al [26] that the blue shift is observed with y > 0.1. The apparent blue shift may be attributed to the contraction of the lattice parameter in CeO_2–$ErO_{1.5}$ solid solution with increasing $ErO_{1.5}$ content.

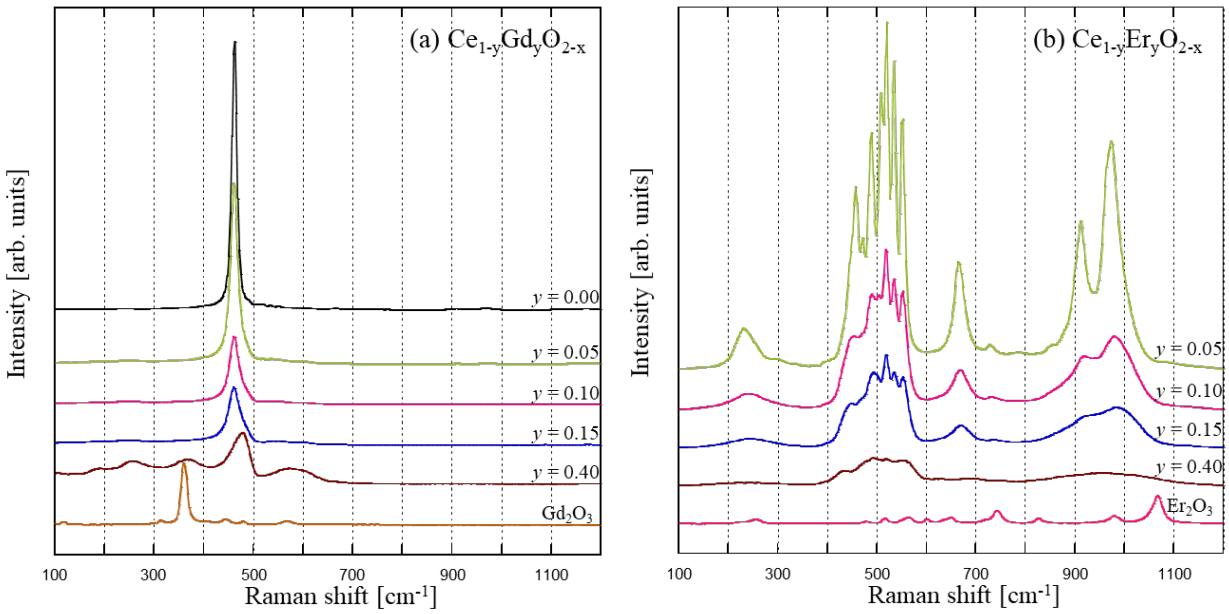

Figure 30. Raman spectra of CeO_2–$LnO_{1.5}$ samples as a function of $LnO_{1.5}$ content.

3.7 Local structure in UO_2–$LnO_{1.5}$ and CeO_2–$LnO_{1.5}$ solid solutions

(a) UO_2–$LnO_{1.5}$ solid solutions

Figure 31 shows the X-ray absorption near edge structure (XANES) and EXAFS spectra of the U L_3 absorption edges of UO_2, U_3O_8, and UO_3 solid solutions. The energies of the edge and the absorption peak increase with an increase in the valence of U because the higher charge of the cation increases the electron binding energy [42]. The absorption peaks for UO_2 (17.176 keV), U_3O_8 (17.181 keV), and UO_3 (17.179 keV) were close to those reported by Leinders et al. [43].

The XRD pattern for sample B (UO_2 sintered in Ar-10% H_2) only contained single-phase peaks and agreed well with that of the standard UO_2 obtained from the reducing reaction. Thus, sample B was the same as the reference sample. The deviations of the XANES and EXAFS spectra for UO_2 (sintered in Ar), U_3O_8, and UO_3 from reference sample B are also shown in Fig. 31 (lower half). Here, I_{Std} and I_i are the absorption intensities at each incident X-ray energy of sample B and the other samples, respectively. The differences in U_3O_8 and UO_3 from sample B were indicated by the increase in absorption edges and the decrease in their peak heights, which were caused by the increase in the valence of the U ions.

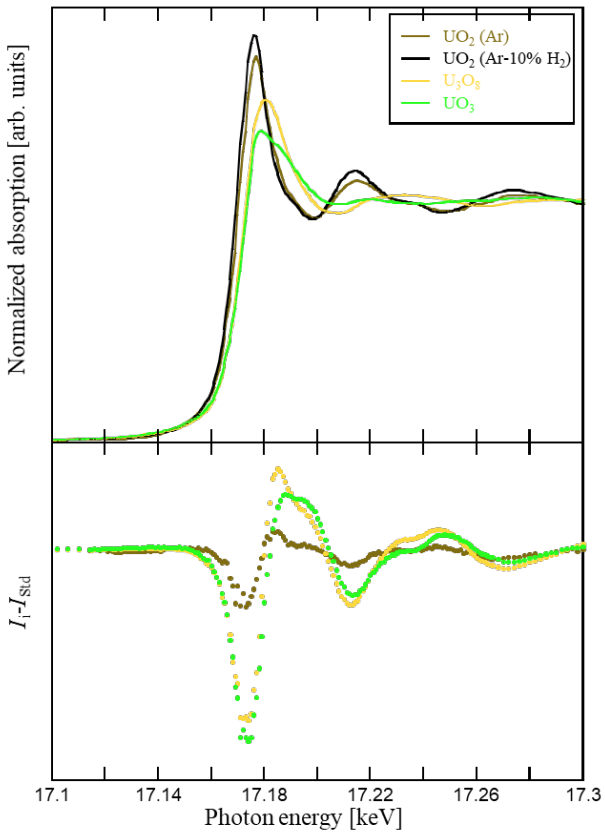

Figure 31. XANES and EXAFS spectra of the U L_3 edge of UO_2, U_3O_8, and UO_3 solid solutions.

Figure 32 shows the XANES and EXAFS spectra of the U L_3 edge of UO_2–$LnO_{1.5}$ solid solutions, U_3O_8, and UO_3. The XANES spectra of UO_2–$LnO_{1.5}$ were shifted slightly to higher photon energies as the $LnO_{1.5}$ content increased. The oxidation of U was evaluated from the shape and the peak position of XANES

spectra. The XANES spectra of the U L_3 edge of UO_2–$LnO_{1.5}$ were different from that of pure UO_2 because in UO_2–$LnO_{1.5}$ there were U oxidation states other than the tetravalent U^{4+} cation present. There were almost no oxygen deficiencies, x, in our solid solutions (Fig. 23); thus, it is reasonable that some U ions had an ionic charge greater than 4+ (i.e., 5+ or 6+) based on the electroneutrality condition. In particular, the spectrum for UO_2–40 mol % $LnO_{1.5}$ was shifted substantially compared with that of UO_2 and was close to that of U_3O_8. This observation suggested that some U^{4+} was oxidized to U^{5+} or U^{6+}. For the UO_2–$GdO_{1.5}$ system, a similar shift in the absorption peaks for $U_{1-y}Gd_yO_2$ (y = 0.04–0.14) was confirmed by XAFS measurements [44]. However, no XAFS data has been reported for the UO_2–$ErO_{1.5}$ system. Thus, this is the first observation of the oxidation of U from U^{4+} to U^{5+} or U^{6+} in the UO_2–$ErO_{1.5}$ system.

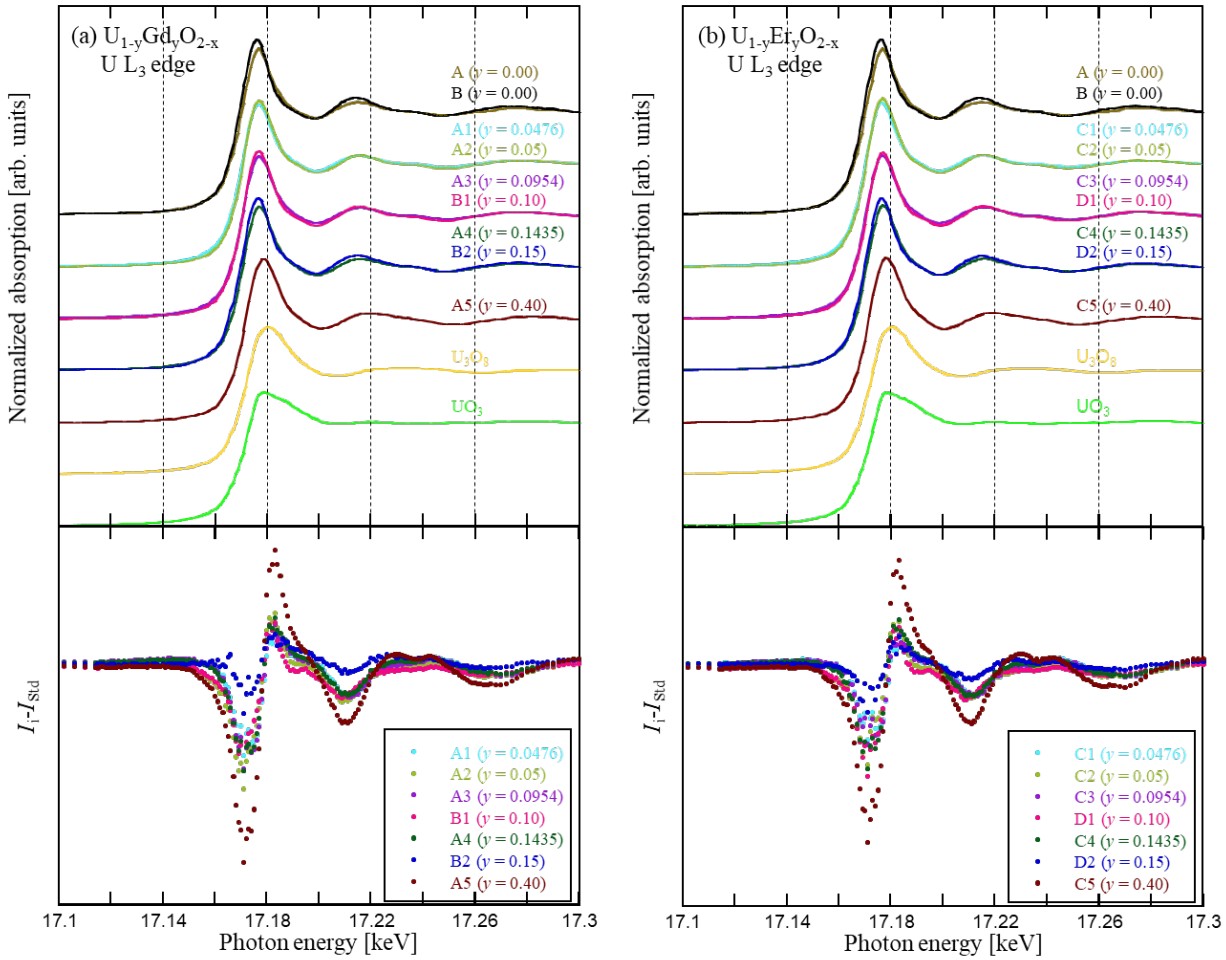

Figure 32. X-ray absorption spectra near the U L_3 edge of $U_{1-y}Ln_yO_{2-x}$, U_3O_8, and UO_3 solid solutions.

Figures 33 (a) and (c) show the U L_3 edge EXAFS functions for UO_2–$LnO_{1.5}$ samples. For UO_2–$GdO_{1.5}$ samples, EXAFS functions in the k-space of UO_2–$GdO_{1.5}$ up to 15 mol % $GdO_{1.5}$ were close to that of UO_2, whereas the EXAFS function of sample A5 was shifted slightly to a higher k-space. Likewise, the EXAFS functions in the k-space for UO_2–$ErO_{1.5}$ were similar. The UO_2–$LnO_{1.5}$ samples retained the cubic fluorite structure up to 40 mol % $LnO_{1.5}$.

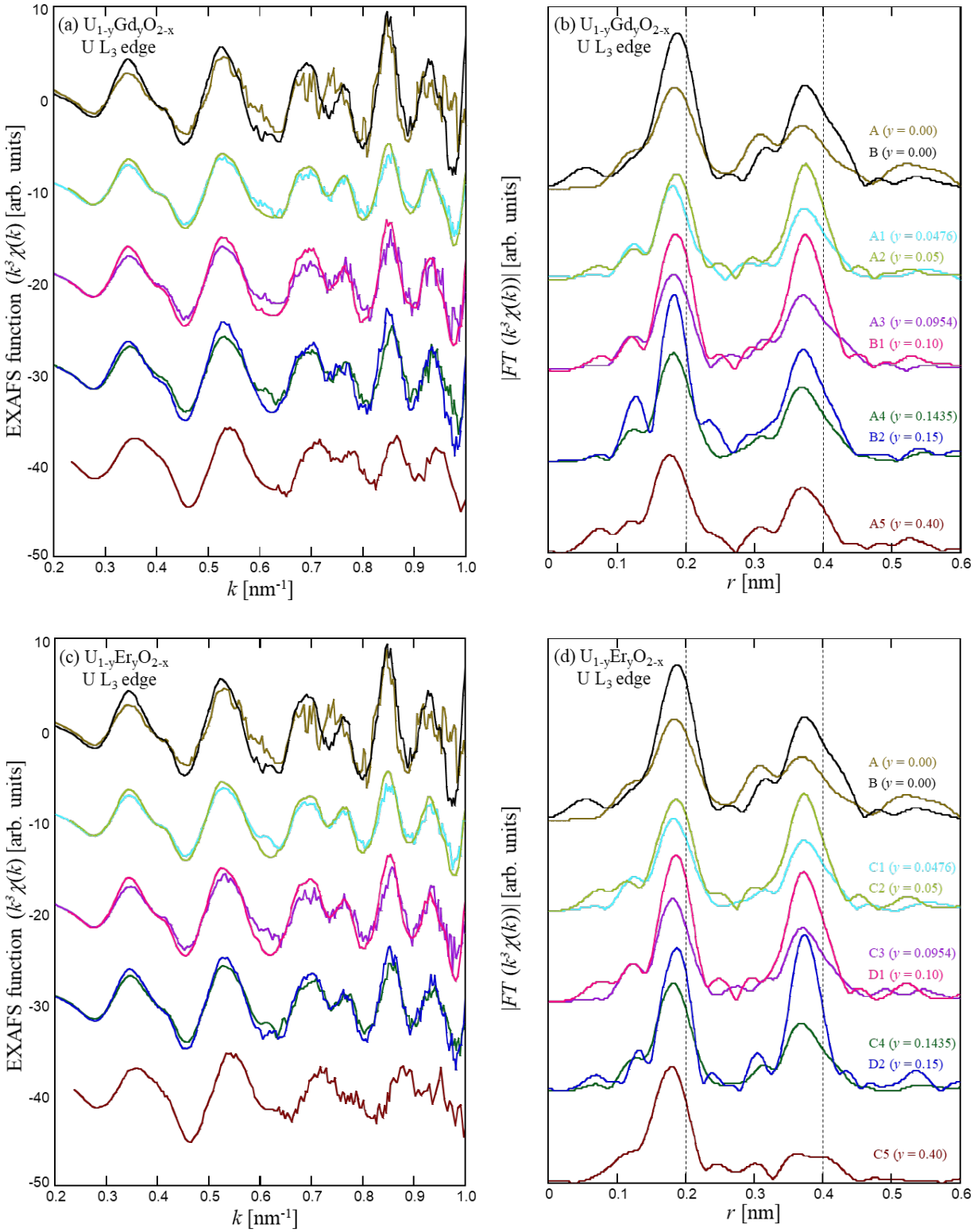

Figure 33. U L_3 edge EXAFS functions and FT magnitude functions of UO_2–$LnO_{1.5}$ samples.

It was confirmed that Fourier transformation, $FT(k^3\chi(k))$, of EXAFS functions, $k^3\chi(k)$, results in the atomic radial distribution function around the absorber atoms [45]. The radial distribution is defined in r-space. Hence, the Fourier transform magnitude presents the interatomic distances of the nearest cation-oxygen,

and cation-cation pairs in UO_2–$LnO_{1.5}$ samples. The shorter distance determined by the Fourier transformation than the actual distance is due to the energy dependence of the phase factors in the sine function [46]. Figures 6 (b) and (d) show the U L_3 edge FT magnitudes of UO_2–$LnO_{1.5}$ samples. Two major peaks were observed corresponding to the interatomic distances of U–O (first shell) and U–U, U–Ln (second shell), respectively. The position of the first peaks corresponding to the U–O interatomic distances decreased slightly as the $LnO_{1.5}$ content increased. For 40 mol % $LnO_{1.5}$, the interatomic U–O distance was substantially shorter than that of UO_2. In contrast, the interatomic distance between cations (U–U, U–Ln) did not change with the $LnO_{1.5}$ concentration.

Figure 34 shows the FT magnitude functions of the Gd L_3 and Er L_3 edges for the UO_2–$LnO_{1.5}$ samples. The first shell Gd–O and Er–O interatomic distances did not change with the addition of $LnO_{1.5}$.

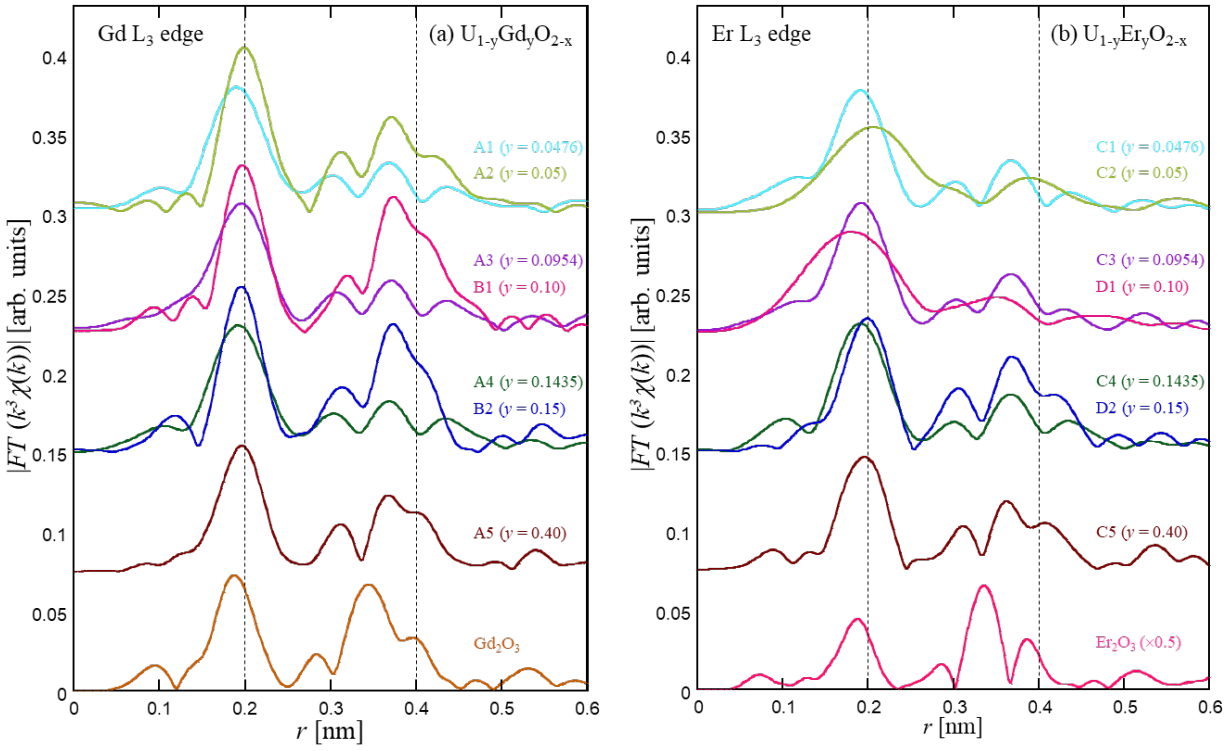

Figure 34. Ln L_3 edge FT magnitude functions for (a) UO_2–$GdO_{1.5}$ and (b) UO_2–$ErO_{1.5}$ samples.

Figures 34 (a) and (b) show the U–O and Ln–O interatomic distances for $U_{1-y}Ln_yO_{2-x}$ samples obtained from fitting the U L_3 and Ln L_3 edges, respectively. The U–O interatomic distance values for samples A (0.2337 nm), B (0.2336 nm), A1 (0.2319 nm), A2 (0.2334 nm), A3 (0.2317 nm), B1 (0.2331 nm), A4 (0.2320 nm), B2 (0.2312 nm), A5 (0.2282 nm), C1 (0.2330 nm), C2 (0.2333 nm), C3 (0.2316 nm), D1 (0.2329 nm), C4 (0.2319 nm), D2 (0.2322 nm), and C5 (0.2281 nm) decreased slightly with increasing $LnO_{1.5}$ content (Fig. 35 (a)). These fitting values were close to the value of 0.2340 nm (UO_2) and much longer than that of 0.2220 nm (U_3O_8) reported by Okamoto et al. [2]. The fitting values were also close to those of literature [44]. The Gd–O interatomic distance gradually decreased with increasing *y* (Fig. 35 (b))

[44], whereas the Er–O interatomic distance reached its maximum at y = 0.954–0.15. The Er–O distances could not be obtained for the C1 and D1 samples because fitting analyses did not work. Hence, more detailed analyses are needed to confirm the behavior of the Ln–O distance at small y values.

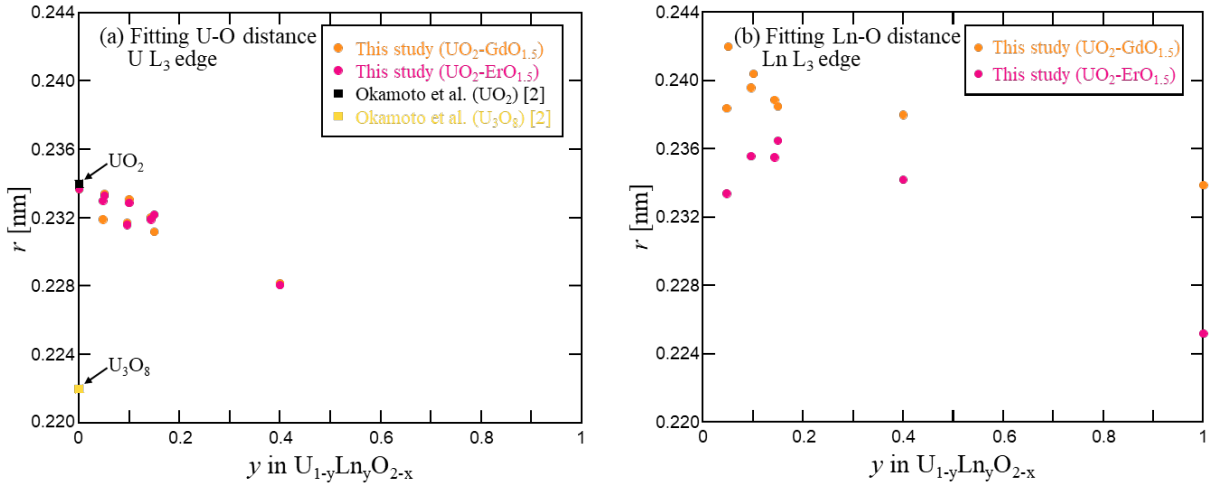

Figure 35. Fitting of the (a) U L_3 edge U–O and (b) Ln L_3 edge Ln–O interatomic distances for the UO_2–$LnO_{1.5}$ samples.

The relevant parameters of U L_3, Gd L_3, and Er L_3 edges obtained by curve fitting analyses for UO_2–$LnO_{1.5}$ samples are given in Appendices 1 and 2. Here, S_0^2 is the reduction factor, CN is the oxygen coordination number, r is the interatomic distances, σ is the Debye-Waller factor, ΔE is the absorption edge energy shift value, R is the residual.

(b) CeO_2–$LnO_{1.5}$ solid solutions

Figure 36 shows the XANES and EXAFS spectra of the Ce L_3 edge of CeO_2–$LnO_{1.5}$ solid solutions measured by fluorescence mode. In both CeO_2–$GdO_{1.5}$ and CeO_2–$ErO_{1.5}$ systems, the XANES spectra of CeO_2–$LnO_{1.5}$ were almost the same with increasing $LnO_{1.5}$ content up to 40 mol %. The shape and the peak position of XANES spectra did not change suggesting that cerium retained the tetravalent Ce^{4+} cation in these samples.

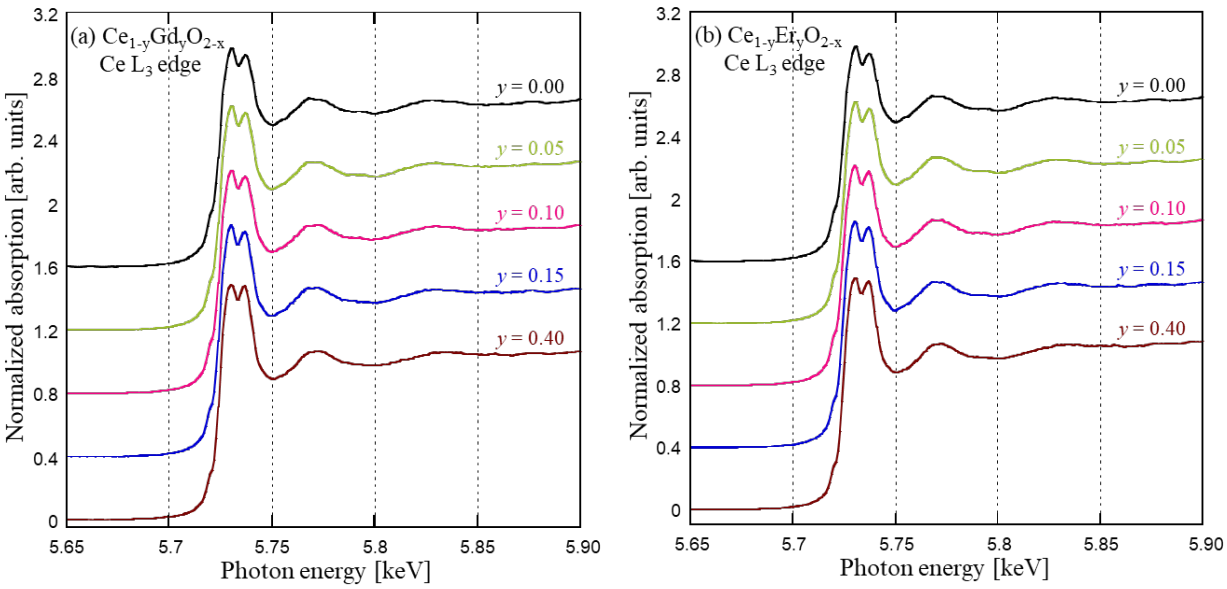

Figure 36. X-ray absorption spectra near the Ce L_3 edge of $Ce_{1-y}Ln_yO_{2-x}$ samples measured by fluorescence mode.

Figure 37 shows the Ce L_3 edge EXAFS functions and FT magnitudes for CeO_2–$LnO_{1.5}$ samples measured by fluorescence mode. Although the EXAFS function of CeO_2–40 mol % $LnO_{1.5}$ was shifted slightly to a higher k-space, the EXAFS functions in the k-space of CeO_2–$LnO_{1.5}$ samples (Fig. 37 (a, c)) were close to that of CeO_2. Thus, the CeO_2–$LnO_{1.5}$ samples retained the cubic fluorite structure up to 40 mol % $LnO_{1.5}$.

Two major peaks were observed corresponding to the interatomic distances of Ce–O (first peak) and Ce–Ce, Ce–Ln (second peak), respectively. The position of the first peaks corresponding to the Ce–O interatomic distances decreased slightly as the $LnO_{1.5}$ content increased up to 40 mol %. The Ce–(Ce,Gd) interatomic distances did not change with the $LnO_{1.5}$ concentration up to 40 mol % in CeO_2–$GdO_{1.5}$. Likewise, Ce–(Ce,Er) interatomic distances did not change with the $ErO_{1.5}$ content up to 15 mol %, whereas for CeO_2–40 mol % $ErO_{1.5}$, all interatomic distances (both major peaks) were substantially shorter than those of CeO_2.

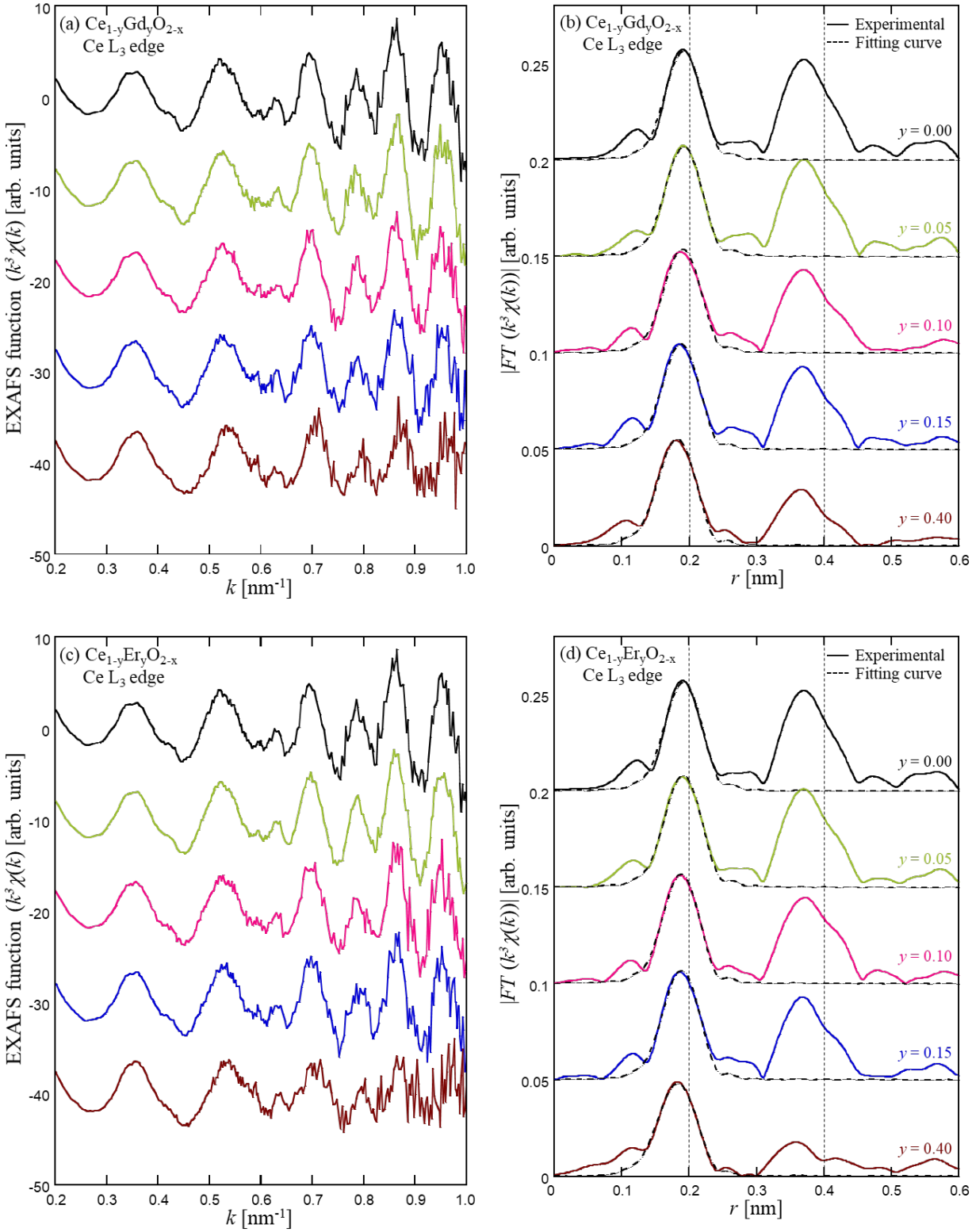

Figure 37. Ce L_3 edge EXAFS functions and FT magnitude functions of CeO_2–$LnO_{1.5}$ samples measured by fluorescence mode.

Figure 38 shows the FT magnitude functions of the Gd L_3 and Er L_3 edges for the CeO_2–$LnO_{1.5}$ samples measured by transmission mode. The first shell Gd–O and Er–O interatomic distances decreased gradually

with the addition of $LnO_{1.5}$. In conclusion, the Ce–O and Ln–O interatomic distances, $d_{cation-anion}$, of CeO_2–$LnO_{1.5}$ solid solutions decreased with increasing $GdO_{1.5}$ content up to 40 mol %. Our results agreed well with those of the literature [27,28]. The Ce–O and Ln–O interatomic distances in CeO_2–$LnO_{1.5}$ samples obtained in Figs. 37 and 38 are plotted as a function of $LnO_{1.5}$ dopant concentration in Fig. 39. The fitted parameters of Ce L_3, Gd L_3, and Er L_3 edges for CeO_2–$LnO_{1.5}$ solid solution samples are given in Appendices 3 and 4. The shortening in both Ce–O and Ln–O interatomic distances was in good agreement with the contraction of the lattice of CeO_2–$ErO_{1.5}$ due to the $ErO_{1.5}$ doping, however, it was inconsistent with the expansion of the lattice of CeO_2–$GdO_{1.5}$ as the $GdO_{1.5}$ content increased. This observation supposed that Gd^{3+} ions and oxygen vacancies were not randomly distributed on cation and anion sites, respectively, but defect clusters, e.g. Gd^{3+}–V_O–Gd^{3+}, were formed in CeO_2–$GdO_{1.5}$ sample.

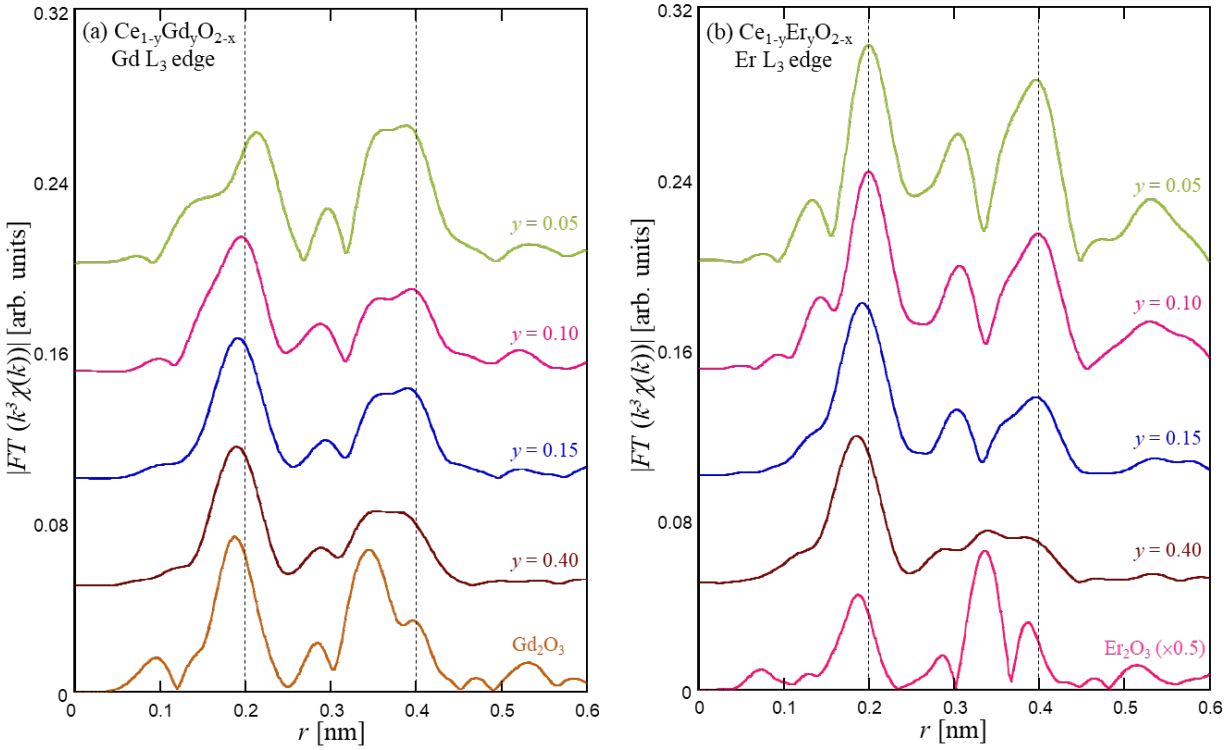

Figure 38. Ln L_3 edge FT magnitude functions for (a) CeO_2–$GdO_{1.5}$ and (b) CeO_2–$ErO_{1.5}$ samples measured by transmission mode.

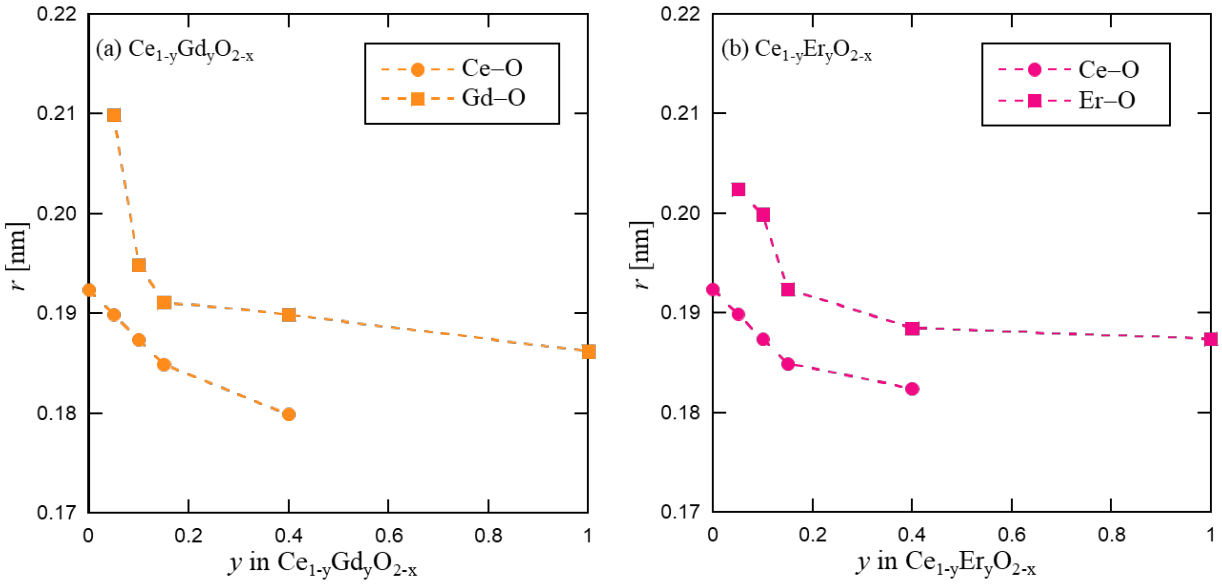

Figure 39. The Ce–O and Ln–O interatomic distances in CeO_2–$LnO_{1.5}$ as a function of $LnO_{1.5}$ content.

On the other hand, CeO_2, CeO_2–4.76 mol % $ErO_{1.5}$, CeO_2–9.54 mol % $ErO_{1.5}$, CeO_2–14.35 mol % $ErO_{1.5}$, and CeO_2–14.35 mol % $GdO_{1.5}$ solid solution samples sintered at 1873 K in air for 8 h were ground into powders. Then, these powders were mechanically blended with boron nitride (BN, 99.5% purity) in a mortar for 5 min. The mixed powders were uni-axially pressed into a disk-shaped pellet (7 mm in diameter and 1 mm thick). Sample compositions and characteristics are given in Table 8. XAFS measurements of these samples were performed at the beamline BL22XU station in the SPring-8. The X-ray absorption measurements near the Ce K, and Er K edges were carried out at room temperature with synchrotron radiation in transmission mode.

Table 8. Sample characteristics for CeO_2–$LnO_{1.5}$ solid solutions measured at SPring-8

$LnO_{1.5}$ content [wt %]	$LnO_{1.5}$ content [mol %]	Sintering atmosphere	CeO_2 weight [g]	BN weight [g]	CeO_2 [wt %]	BN [wt %]	Mixing time [min]
-, 0.0	-, 0.0	Air	0.00701	0.0502	7.25	92.75	5
Er, 5.00	Er, 4.76	Air	0.00910	0.0507	9.97	90.03	5
Er, 10.00	Er, 9.54	Air	0.00950	0.0502	10.02	89.98	5
Er, 15.00	Er, 14.35	Air	0.00850	0.0506	9.99	90.01	5
Gd, 15.00	Gd, 14.35	Air	0.0088	0.0507	10.00	90.00	5

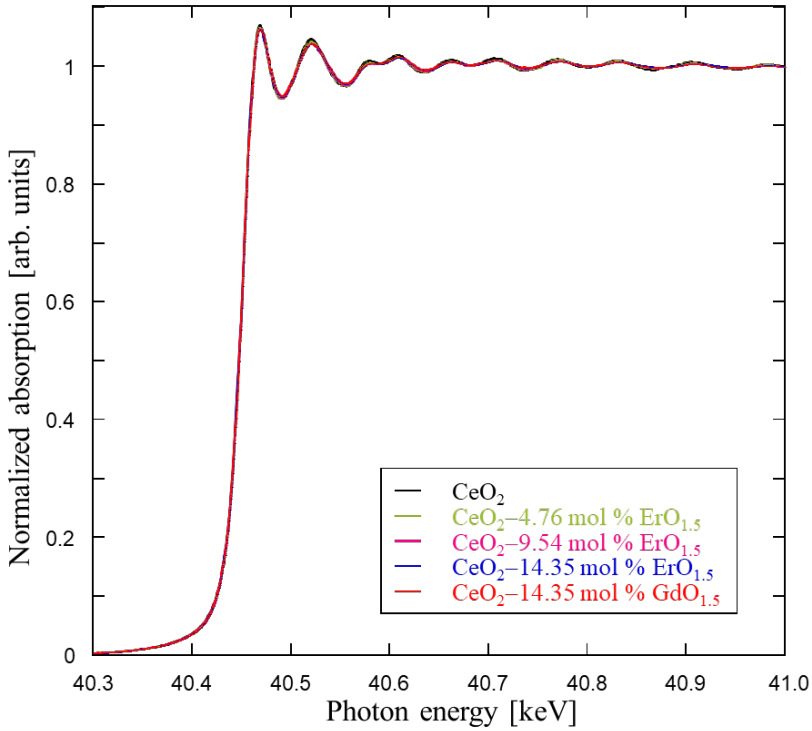

Figure 40. XANES and EXAFS spectra of the Ce K edge of $Ce_{1-y}Ln_yO_{2-x}$solid solutions.

Figure 40 shows the XANES and EXAFS spectra of the Ce K edge of CeO_2–$LnO_{1.5}$ samples measured by transmission mode. The shapes and the peak positions of XANES and EXAFS spectra here are different from those of spectra of Ce L_3 shown in Fig. 36 due to the difference in absorption edges. However, both observations showed the same tendency that, in both CeO_2–$GdO_{1.5}$ and CeO_2–$ErO_{1.5}$ systems, the XANES spectra of CeO_2–$LnO_{1.5}$ mostly did not change with increasing $LnO_{1.5}$ content up to 14.35 mol %. This observation confirmed again that Ce retained the tetravalent Ce^{4+} cation in these samples.

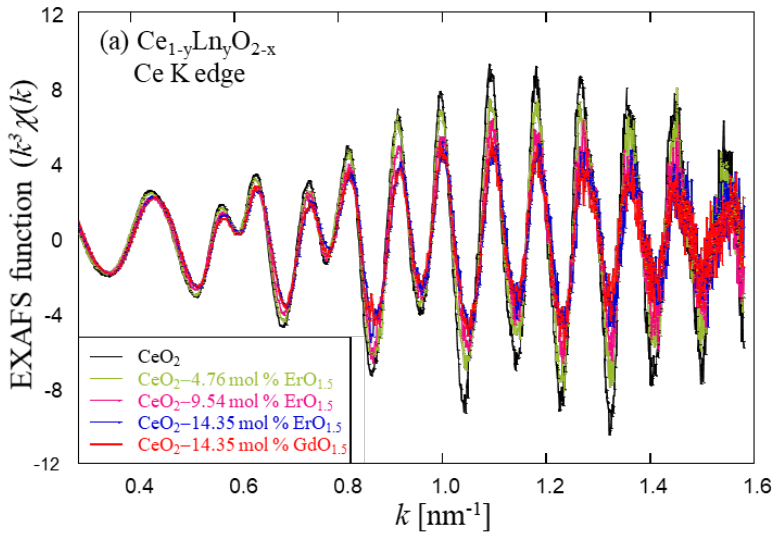

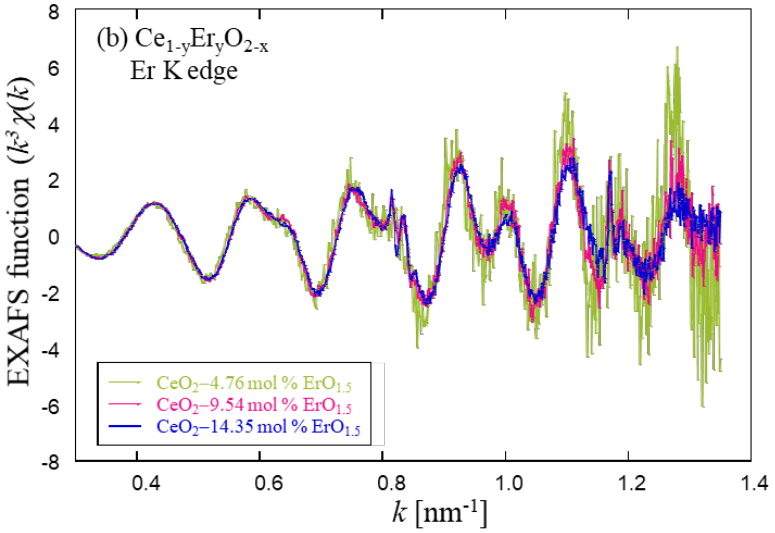

Figure 41. Ce K edge (a) and Er K edge (b) EXAFS functions of CeO_2–$LnO_{1.5}$ samples.

Figure 41 shows the EXAFS functions of Ce K edge, and Er K edge for CeO_2–$LnO_{1.5}$ samples. The EXAFS functions of both Ce K, and Er K edges for CeO_2–$LnO_{1.5}$ were shifted slightly to a higher k-space as the $LnO_{1.5}$ content increased. However, the change is very small. In addition, the EXAFS functions in the k-space decreased with increasing $LnO_{1.5}$ up to 14.35 mol %.

Figure 42 (a) shows the interatomic distances of Ce–O and Ce–(Ce,Ln), and figure 42 (b) shows the interatomic distances of Er–O and Er–(Ce,Er) in CeO_2–$LnO_{1.5}$ samples as a function of $LnO_{1.5}$ content. Similar to the results shown in Figs. 37 and 38, Ce–O and Er–O interatomic distances of CeO_2–$LnO_{1.5}$ solid solutions decreased with increasing $LnO_{1.5}$ content up to 14.35 mol %. Whereas, their Ce–(Ce,Ln) and Er–(Ce,Er) interatomic distances were almost unchanged with the addition of $LnO_{1.5}$.

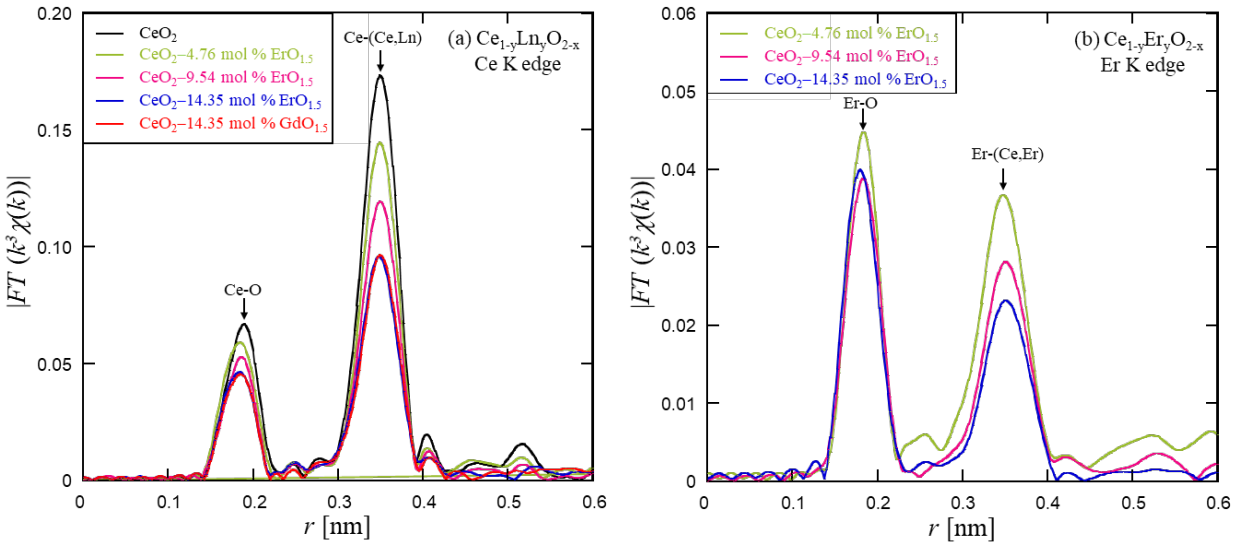

Figure 42. Ce K edge (a) and Er K edge (b) FT magnitude functions of CeO_2–$LnO_{1.5}$ samples.

3.8 Summary

The structural properties of UO_2–$LnO_{1.5}$ and CeO_2–$LnO_{1.5}$ solid solution samples were evaluated by various techniques, i.e., XRD, Raman spectroscopy, and XAFS. A single fluorite structure (F-type) was detected for most UO_2–$LnO_{1.5}$ samples sintered at 1973 K under Ar and Ar-10% H_2 atmospheres, indicating that Gd and Er were dissolved well in the UO_2 fluorite structure. For $LnO_{1.5}$ content of ≤ 5 mol %, a small amount of the U_4O_9 phase formed in the UO_2–$LnO_{1.5}$ samples. In the CeO_2–$LnO_{1.5}$ samples sintered at 1873 K in air, the F-type lattice was mainly retained until 40 mol % of $LnO_{1.5}$, though the small peaks of XRD pattern from C-type structure of Ln_2O_3 appeared and the small ones from the second phase formed in CeO_2–40 mol % $LnO_{1.5}$ samples.

The lattice parameters of UO_2–$LnO_{1.5}$ decreased as the $LnO_{1.5}$ content increased to 40 mol %. The UO_2–$LnO_{1.5}$ samples sintered in Ar-10% H_2 had a slightly larger lattice size than those sintered in Ar. Since the lattice parameter of UO_2–$LnO_{1.5}$ decreases as the O/M ratio increases, this observation indicated that the sample sintered under more reducing conditions with Ar-10% H_2 had a smaller O/M ratio than that sintered in Ar. However, the lattice parameters of UO_2–$LnO_{1.5}$ sintered under both conditions were close and they were also close to that of stoichiometric $(U,Ln)O_{2.00}$. When Ln^{3+} ions are substituted for U^{4+} ions in the host cation sites, either oxygen vacancies (V_O) are created or some of the U^{4+} are oxidized to U^{5+} or U^{6+} ions to maintain electrical neutrality. It was confirmed by XAFS that the oxidation state of U in the UO_2–$LnO_{1.5}$ was not solely tetravalent U^{4+}, partly oxidized to U^{5+}. The U–O interatomic distances decreased slightly and Ln–O interatomic distance did not change with increasing $LnO_{1.5}$ content. The shortening in the interatomic distances was in accordance with the contraction of the UO_2–$LnO_{1.5}$ lattices due to the dopant $LnO_{1.5}$. The presence of U^{5+} ions resulted in the reduction in the lattice parameter of UO_2–$LnO_{1.5}$.

For CeO_2–$LnO_{1.5}$ sintered in air, the lattice size of CeO_2–$GdO_{1.5}$ increased with increasing $GdO_{1.5}$ content, whereas that of CeO_2–$ErO_{1.5}$ decreased as the $ErO_{1.5}$ content increased. XAFS showed that Ce retained the Ce^{4+} cation, and both Ce–O and Ln–O interatomic distances decreased with increasing $LnO_{1.5}$ content. Therefore, the ionic radii of cations and V_O were supposed to determine the lattice sizes of these samples. The shortening in the interatomic distances was in good agreement with the contraction of the CeO_2–$ErO_{1.5}$ lattice, however, it was inconsistent with the expansion of the CeO_2–$GdO_{1.5}$ lattice. Based on MD (molecular dynamics) simulation results of the lattice parameters, it is supposed that Ln^{3+} ions and V_O are not randomly distributed on cation and anion sites, respectively, but defect clusters, e.g., Ln^{3+}–V_O–Ln^{3+}, formed in CeO_2–$LnO_{1.5}$ samples. Thus, MD analyses well explained the increase and decrease in lattice parameters of CeO_2–$GdO_{1.5}$ and CeO_2–$ErO_{1.5}$, respectively, with an increase of Ln^{3+} content at the atomic scale. Lattice parameters calculated by MD for CeO_2–$LnO_{1.5}$ suggested that the defect clusters, Ln^{3+}–V_O–Ln^{3+}, were formed in these solid solutions.

Raman spectra showed that pure UO_2 had one triply degenerate Raman-active mode (T_{2g}), which is the characteristic of the stoichiometric fluorite structure at 445 cm^{-1}, one first order longitudinal optical L-O phonon mode at 575 cm^{-1}, and one 2L-O phonon at 1150 cm^{-1}. In the Raman spectra of UO_2–$LnO_{1.5}$ samples, the broad peaks detected at around 455 cm^{-1} and 550 cm^{-1} were close to those of U_4O_9 at 455 cm^{-1} and 630 cm^{-1}, suggesting that some U ions in UO_2–$LnO_{1.5}$ system had an ionic charge greater than 4+ (i.e, 5+ or 6+). The Raman scattering peaks of UO_2–$LnO_{1.5}$ were shifted slightly to higher wavenumbers as $LnO_{1.5}$ content increased up to 40 mol %, indicating the degradation of the lattice structure in these fluorite structures due to the dopant $LnO_{1.5}$. A blue shift in the T_{2g} and 2L-O modes to higher wavenumbers caused by the contraction of the UO_2–$LnO_{1.5}$ lattices, which can be attributed to the formation of oxygen vacancies when $LnO_{1.5}$ is added into UO_2.

On the other hand, in the Raman spectra for CeO_2–$GdO_{1.5}$, only a Raman-active mode at F_{2g} 465 cm^{-1} was existed, indicating that the F-type lattice in CeO_2–$GdO_{1.5}$ was maintained up to 40 mol % $GdO_{1.5}$. Similar to UO_2–$LnO_{1.5}$ systems, the intensity of the peaks of CeO_2–$LnO_{1.5}$ decreased as the $LnO_{1.5}$ content increased due to the increase in oxygen vacancies. In the CeO_2–$ErO_{1.5}$ samples, the first order Raman peak at around 465 cm^{-1} disappeared. $ErO_{1.5}$ doping into CeO_2 shifted the Raman peaks to higher frequencies accompanied by a decrease in intensity in CeO_2–$ErO_{1.5}$ samples. The apparent blue shift may be attributed to the contraction of the lattice parameter in CeO_2–$ErO_{1.5}$ with increasing $ErO_{1.5}$ content. However, our observation showed the peaks with broadened shoulders, those can be attributed to the Er–O complexation within the system. These results can be considered to be due to the poor homogeneity and crystallinity in CeO_2–$EO_{1.5}$ solid solution.

3.9 References.

[1] T. Resslert, J. Synchr. Rad. 5 (1998) 118–122.

[2] Y. Okamoto, M. Takano, Progress in J. Nucl. Sci. Tech. 5 (2018) 200–203.

[3] A.L. Ankudinov, B. Ravel, J.J. Rehr, S.D. Conradson, Phys. Rev. B. 58 (1998) 7565–7576.

[4] L. Desgranges, G. Baldinozzi, G. Rousseau, J.C. Nièpce, G. Calvarin, Inorg. Chem. 48 (2009) 7585–7592.

[5] A. Saiki, N. Ishizawa, N. Mizutani, M. Kato, K. Yogyo, J. Ceram. Assoc. Jpn. 93 (1985) 649–654.

[6] K. Iwasaki, T. Matsui, K. Yanai, R. Yuda, Y. Arita, T. Nagasaki, N. Yokohama, I. Tokura, K. Une, K. Harada, J. Nucl. Sci. Tech. 46 (2009) 673–676.

[7] S. Yamanaka, K. Kurosaki, M. Katayama, J. Adachi, M. Uno, T. Kuroishi, M. Yamasaki, J. Nucl. Mater. 389 (2009) 115–118.

[8] J. Lee, J. Kim, Y.S. Youn, N. Liu, J.G. Kim, Y.K. Ha, D.W. Shoesmith, J.Y. Kim, J. Nucl. Mater. 486 (2017) 216–221.

[9] M. Durazzo, A.C. Freitas, A.E.S Sansone, N.A.M. Ferreira, E.F.U. de Carvalho, H.G. Riella, R.M.L. Neto, J. Nucl. Mater. 510 (2018) 603–612.

[10] J.P. Lauriat, G. Chevrier, J.X. Boucherle, J. Solid State Chem. 80 (1989) 80–93.

[11] S.R. Teixeira, K. Imakuma, J. Nucl. Mater. 178 (1991) 33−39.
[12] S. Fukushima, T. Ohmichi, A. Maeda, H. Watanabe, J. Nucl. Mater. 105 (1982) 201−210.
[13] T. Ohmichi, S. Fukushima, A. Maeda, H. Watanabe, J. Nucl. Mater. 102 (1981) 40−46.
[14] S.H. Kim, Y.G. Kim, H.S. Kim, S.H. Na, Y.W. Lee, D.S. Surh, J. Nucl. Mater. 342 (2005) 119−124.
[15] R.J. Beals, J. H. Handwerk, J. Am. Ceram. Soc. 48 (1965) 271−274.
[16] M. Amaya, K. Une, M. Hirai, J. Nucl. Sci. Tech. 41 (2004) 108−115.
[17] J. Kim, J. Lee, Y.S. Youn, N. Liu, J.G. Kim, Y.K. Ha, S.E. Bae, D.W. Shoesmith, J.Y. Kim, Electrochimica Acta. 247 (2017) 942−948.
[18] R.D. Shannon, Acta Cryst. A 32 (1976) 751−767.
[19] T. Vazhappilly, A.K. Pathak, Comput. Mater. Sci. 185 (2020) 109933.
[20] T. Vazhappilly, A.K. Pathak, J. Nucl. Mater. 519 (2019) 128−136.
[21] V. Grover, A.K. Tyagi, Mater. Res. Bull. 39 (2004) 859−866.
[22] C. Goulart, E. Djurado, J. Eur. Ceram. Soc. 33 (2013) 769−778.
[23] Y. Ikuma, K. Takao, M. Kamiya, E. Shimada, Mater. Sci. Eng. B99 (2003) 48−51.
[24] M. Zinkevich, D. Djurovic, F. Aldinger, in Proc. 7th Euro. SOFC Forum 2006, J.Kilner ed., (Lucerie, Switzerland, 2006) P0512 (CD ROM).
[25] S.J. Hong, A.V. Virkar, J. Am. Ceram. Soc. 78 [2] (1995) 433−439.
[26] B.P. Mandal, M. Roy, V. Grover, A.K> Tyagi, J. Appl. Phys. 103 (2008) 033506.
[27] T. Ohashi, S. Yamazaki, T. Tokunaga, Y. Arita, T. Matsui, T. Harami, K. Kobayashi, Solid State Ion. 113−115 (1998) 559−564.
[28] K. Kossoy, Q. Wang, R. Korobko, V. Grover, Y. Feldman, E. Wachtel, A.K. Tyagi, A.I. Frenkel, I. Lubomirsky. Phys. Rev. B 87 (2013) 054101.
[29] D.J. Kim, J. Am. Ceram. Soc. 72 [8] (1989) 1415−1421.
[30] S. Yamazaki, T. Matsui, T. Ohashi, Y. Arita, Solid State Ion. 136−137 (2000) 913−920.
[31] P.R. Graves, Appli. Spectrosc. 44 (1990) 1665−1667.
[32] G.C. Allen, I.S. Butler, J. Nucl. Mater. 144 (1987) 17−19.
[33] D. Manara, B. Renker, J. Nucl. Matter. 321 (2003) 233−237.
[34] T. Livneh, E. Sterer, Phys. Rev. B 73 (2006) 085118.
[35] J. Lee, J. Kim, Y.S. Youn, N. Liu, J.G. Kim, Y.K. Ha, D.W. Shoesmith, J.Y. Kim, J. Nucl. Mater. 486 (2017) 216−221.
[36] H. He, D. Shoesmith, Phys. Chem. Chem. Phys. 12 (2010) 8108−8117.
[37] L. Desgranges, G. Baldinozzi, P. Simon, G. Guimbretière, A. Canizares, J. Raman Spectrosc. 43 (2012) 455−458.
[38] Z. Talip, T. Wiss, P.E. Raison, J. Pailier, D. Manara, J. Somers, J. Am. Ceram. Soc. 98 (2015) 2278−2285.
[39] M. Razdan, D.W. Shoesmith, J. Electrochem. Soc. 161 (2014) H105−H113.
[40] A. Banerji, V. Grover, V. Sathe, S.K. Deb, A.K. Tyagi, Solid State Communications. 149 (2009) 1689−1692.

[41] J.R. McBride, K.c. Hass, B.D. Poindexter, W.H. Weber, J. Appl. Phys. 76 (1994) 2435−2441.
[42] S.D. Conradson, D. Manara, F. Wastin, D.L. Clark, G.H. Lander, L.A. Morales, J. Rebizant, V.V. Rondinella. Inorg. Chem. 43 (2004) 6922−6935.
[43] G. Leinders, R. Bes, K. O. Kvashnina, M. Verwerft, Inorg. Chem. 59 (2020) 4576−4587.
[44] R. Bès, J. Pakarinen, A. Baena, S. Conradson, M. Verwerft, F. Tuomisto, J. Nucl. Mater. 489 (2017) 9−21.
[45] D.E. Sayers, E.A. Stern, F.W. Lytle, Phys. Rev. Lett. 27 (1971) 1204−1207.
[46] D.C. Koningsberger, B.L. Mojet, G.E. van Dorssen, D.E. Ramaker, Top Catal. 10 (2000) 143−155.

CHAPTER 4

EVALUATION OF THE THERMAL PROPERTIES OF $U_{1-y}Ln_yO_{2-x}$ AND $Ce_{1-y}Ln_yO_{2-x}$ SOLID SOLUTIONS

4.1 Introduction

Thermal properties such as heat capacity, thermal diffusivity, and thermal conductivity of the nuclear fuel pellets are of great importance. They are dependent on the density of the sample, temperature, chemical composition, grain boundaries, oxygen-to-metal ratio (O/M), etc. Thermal diffusivity is the thermo-physical property that defines the speed of heat propagation by conduction during the changes of temperature and hence, the higher thermal diffusivity, the faster the heat propagation. The thermal diffusivity is related to the thermal conductivity, heat capacity, and density of materials. The thermal conductivities of these solid solution samples were determined from the thermal diffusivity and heat capacity measured by the laser flash method, and the density of the sample.

The heat capacity, thermal diffusivity, and thermal conductivity of UO_2–$LnO_{1.5}$ and CeO_2–$LnO_{1.5}$ solid solutions were simultaneously measured by laser flash analysis (LFA) and then the changes in their thermal conductivities was evaluated as functions of temperature and $LnO_{1.5}$ content. In the present study, the thermal conductivity was measured directly by LFA as well as was estimated using heat capacity calculated by the Neumann-Kopp rule (NKR).

4.2 Laser flash analysis (LFA)

Thermal conductivity is one of the most important transport properties of materials in general, nuclear fuels in particular. There are several presently existing methods, steady-state and non-steady-state (transient). In steady-state methods, the thermal conductivity is determined from the steady temperature gradient in the sample and usually, a large amount of sample is needed. Therefore, it is difficult to avoid the effects of thermal disturbances, especially at high temperatures. This leads to a long period of time is required to measure the thermal conductivity precisely.

In the case of transient methods, the time for measurement is much shorter than that in steady-state methods. The most effective method used for measuring the thermal diffusivity as well as the thermal conductivity is the laser flash method. LFA is one of the non-steady-state methods and does not require the signal to obtain a constant value. Instead, the signal is studied as a function of time. The LFA has been widely used as a convenient technique for measuring thermal diffusivity as well as the thermal conductivity of solid specimens. The advantages of this technique are that it can, in general, be performed more quickly (short measurement time) since there is no need to wait for a steady-state situation together with high accuracy.

LFA is used to directly measure the thermal diffusivity of a thin disk in the thickness direction and thereafter estimate the thermal conductivity of a sample. This method is based upon the measurement of the temperature rise on the rear face of the sample. Figure 43 indicates the principles and schematic of the LFA apparatus used in this study. In principle, a specimen is placed within a controlled atmosphere furnace, a laser energy pulse heats the front side of a thin-disk specimen. The laser beam energy is absorbed by the front surface of solid specimens. The transport of heat through the specimen, as a result of the laser impulse, causes a temperature rise on the rear surface of the specimen. The temperature rise on the backside of the specimen is measured by an infrared detector (IR).

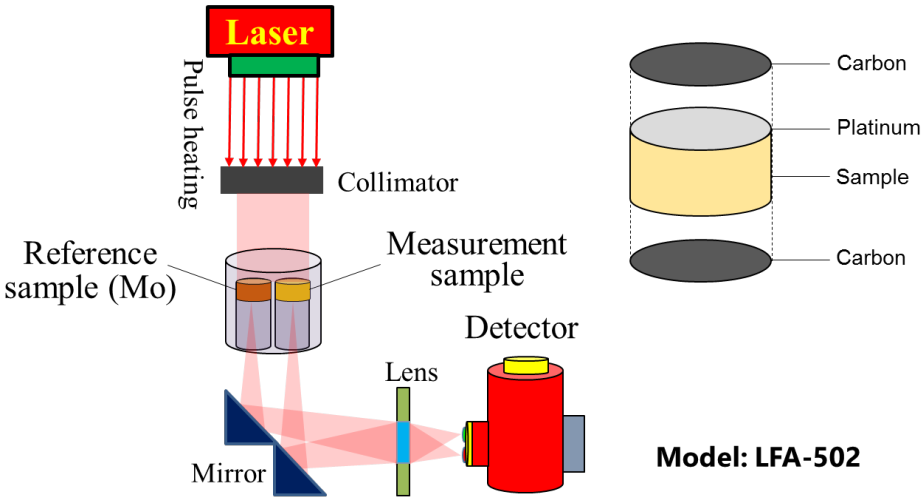

Figure 43. The principles and schematic of LFA apparatus.

LFA (Kyoto Electronics Manufacturing, LFA-502) is used to simultaneously measure the thermal diffusivity and heat capacity of a disk-shaped sample and thereafter to estimate its thermal conductivity. The measurements were carried out over the temperature range from 290 K to near 1700 K from three to five times at every temperature step in a vacuum of less than 5 Pa. The measurement precision of LFA-502 is within ±7% with a measurement temperature range from room temperature to 1773 K. In this method, the front surface of the sample is irradiated by the laser pulse, and the temperature rise on the rear face is measured by the radiation thermometer. The thermal diffusivity is determined by the temperature response of its rear surface. The heat capacity of the sample is estimated by comparing it with the thermal response of the molybdenum reference material of which the heat capacity is well-known. In general, the thermal conductivity, k, of the sample is written by:

$$k = \alpha \cdot C_p \cdot \rho, \tag{13}$$

where k is the thermal conductivity, in $W \cdot m^{-1} \cdot K^{-1}$, α is the thermal diffusivity, in $m^2 \cdot s^{-1}$, C_p is the heat capacity, in $J \cdot kg^{-1} \cdot K^{-1}$, and ρ is the density of the sample, in $kg \cdot m^{-3}$.

There are several available methods to determine the thermal diffusivity based on experiments. The simplest method is measuring the “half-rise time”, $t_{1/2}$, which is the time at which the experimentally

measured rear face temperature reaches half of its maximum value. Responses of the temperature rise on the back surface of specimens are shown in Fig. 44. This figure shows an example of transient temperature curves of CeO_2–10 mol % $GdO_{1.5}$ and molybdenum, as the test and the reference samples, respectively, in the simultaneous measurements of the thermal diffusivity and heat capacity after heating up to 570 K. Based on the time-dependent thermogram of the rear face and in a one-dimensional, adiabatic case with neglecting radiative heat losses, the thermal diffusivity, α, is calculated from this temperature rise as follows [1]:

$$\alpha \cong -\frac{ln\,0.25}{\pi^2} \times \frac{L^2}{t_{1/2}} = 0.1388 \times \frac{L^2}{t_{1/2}}, \tag{14}$$

where L is the thickness of the sample.

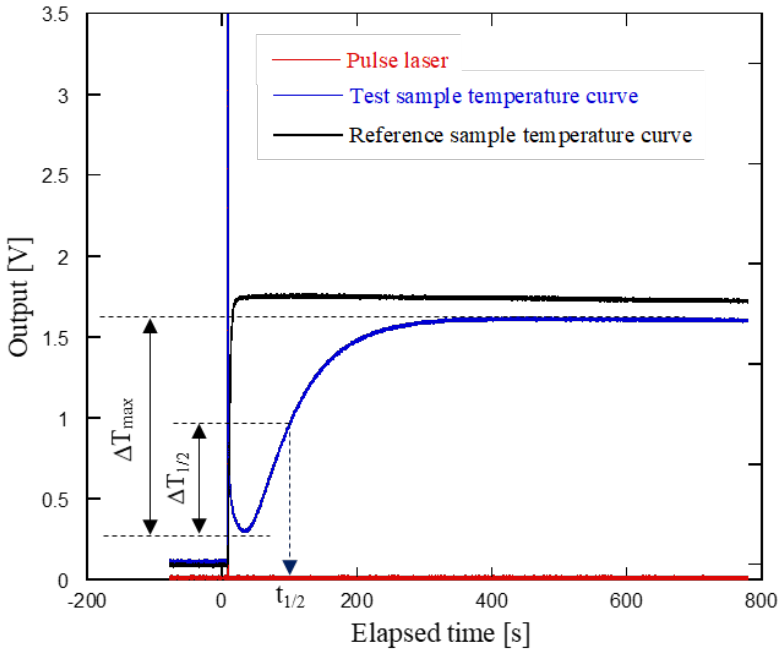

Figure 44. Examples of transient temperature curves observed for simultaneous measurements of thermal diffusivity and heat capacity of CeO_2–10 mol % $GdO_{1.5}$ and reference sample at 570 K.

In the different laser flash calorimetry, a reference sample and a test sample with the almost same diameter and thickness, which their front and back faces were covered with black coating under the same condition at the same temperature are set closely on a sample holder and irradiated uniformly by a homogenized laser beam, as shown in Fig.45. The temperature rises of both samples were measured by using a non-contact infrared radiation thermometer. The reference specimen was molybdenum with a known heat capacity of 10.28 g·cm^{-3}.

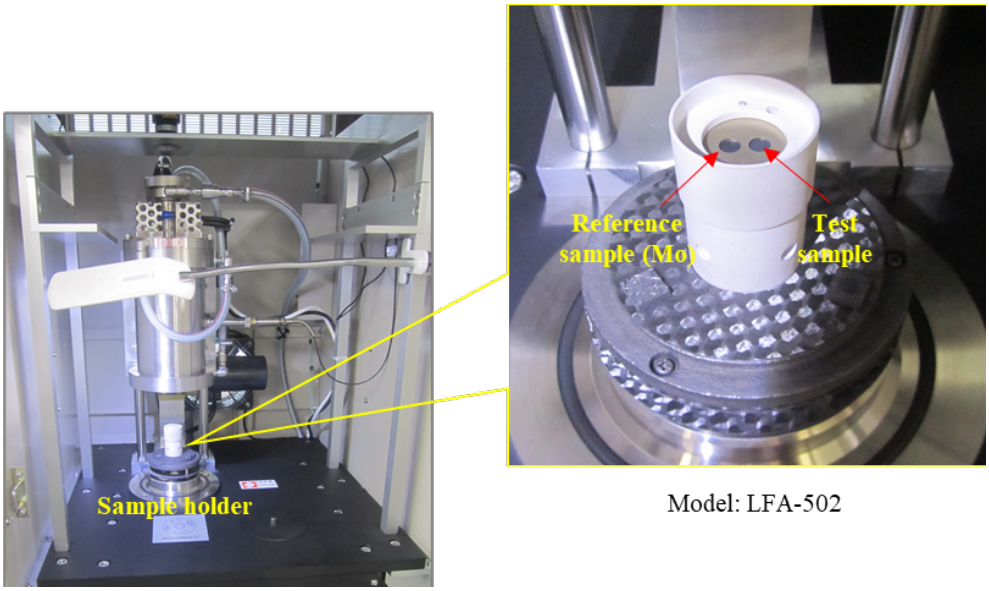

Figure 45. Photographs of LFA-502 apparatus with a magnified image of sample holders for 5 mm diameter.

In the present experiment, the thermal diffusivities of the samples were estimated by analyzing the transient temperature curves on the back surface of both test specimen and reference material using the temperature rise curve-fitting method [2], which took the radiative heat loss and the finite pulse time effects into consideration, followed by an evaluation of heat capacity by comparing the temperature rises between the test and reference samples. On the other hand, in the laser flash calorimetry, a test sample and a reference material with the almost same diameter and thickness are set closely on a sample holder and irradiated uniformly by a homogenized laser beam. Here, in measurements of CeO_2–$LnO_{1.5}$ samples, these front and rear faces of both test and reference samples were covered with a black coating (Dry Graphite Film Lubricant, Nihon Senpaku Kougu Ltd.) to allow the absorption of the laser pulse in the near-surface region and in order to obtain the same measurement conditions between the test and the reference samples. In addition, the front surface of the test sample was coated with a thin film of platinum by using a vapor deposition coater (Sanyu Electron, SC-701 MkII Advance) in order to reduce charging and to prevent the laser light from penetrating from the sample when the sample is measured by LFA.

4.3 Heat capacities

The specific heat capacities C_p of the samples were measured by LFA in this study and was given by,

$$C_p = \frac{Q}{m \cdot \Delta T}, \tag{15}$$

here, Q is the thermal energy absorbed by a specimen, m is its mass and ΔT is an increase in temperature by laser pulse heating. Assuming that Q of the specimen is equal to that absorbed by Mo reference sample, above C_p can be obtained.

At low-middle temperatures (much small than Debye temperature), the specific heat capacity at constant volume is given by,

$$C_v = 9Nk_B\left(\frac{T}{\Theta_D}\right)^3 \int_0^{\Theta_D/T} dx \frac{x^4 e^x}{(e^x-1)^2}, \tag{16}$$

where N is the number of atoms in the crystal or the specimen, k_B is the Boltzman constant, Θ_D is the Debye temperature, T is temperature. The Debye temperature of CeO_2 can be estimated using the lattice parameter and sound velocity which is discussed in detail in Section 5. From here, the specific heat capacity at constant pressure C_p is given by the following equation,

$$C_p = C_v + \frac{9VT\lambda_L^2}{\beta_T}, \tag{17}$$

where V is the volume, λ_L is the linear thermal expansion coefficient, β_T is the isothermal compressibility which is inversely related to the bulk modulus in a solid phase. The bulk modulus for CeO_2 at room temperature estimated from the sound velocities measured by the ultrasonic pulse-echo method is 193.1 GPa [3]. The linear thermal expansion coefficient for CeO_2 in the temperature range from 298 to 1273 K reported by Sameshima et al. is 11.8×10^{-6} K^{-1} [4].

The specific heat capacity obtained from LFA in this study and estimated one based on the Debye model by Eqs. (16,17) for CeO_2 are shown in Fig. 46, compared with other experimental data for CeO_2 [5–7]. The specific heat capacity for CeO_2 obtained from LFA agreed well with those of the literature [5–7]. The specific heat capacities for CeO_2 estimated by Eqs. (16,17) based on the Debye model are comparable with estimated values given by Koning et al. [7]. The heat capacity calculated by Koning et al. [7] agrees well (maximum deviation is around 3.5%) with the available literature data reported by [5–7]. Therefore, for more quantitative analysis, the specific heat capacity estimated based on NKR was also used to estimate the thermal conductivity as well as data obtained from LFA.

At middle and high temperatures, the total energy can be approximated as follows,

$$E \approx 3Nk_BT. \tag{18}$$

The heat capacity is thus obtained after differentiating this expression with respect to the temperature as,

$$C_v = \left(\frac{dE}{dT}\right)_v \approx 3Nk_B, \tag{19}$$

which is almost independent of temperature. This is known as the law of Dulong and Petit. The heat capacity data for CeO_2 were in good agreement with Dulong-Petit law from 400 K to 1000 K.

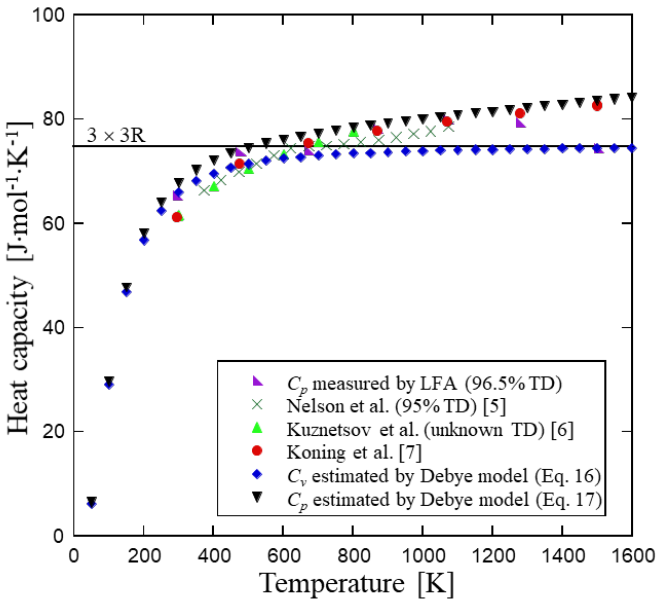

Figure 46. The heat capacity of CeO_2 in this study compared with other experimental data as a function of temperature.

The specific heat capacities of CeO_2–$LnO_{1.5}$ and UO_2–$LnO_{1.5}$ solid solutions were estimated by the Neumann-Kopp rule (NKR) by using data for CeO_2, UO_2, Gd_2O_3, and Er_2O_3 in order to compare with those obtained by LFA in this study. The NKR represents presumably the simplest approach for the estimation of mixed oxide heat capacity, C_{pm}, based on an extensive collection of experimental heat capacity data suggested by Kopp et al. [8], and other researchers such as Neumann and Renault, for solid substances. In this method, the molar heat capacity of the mixed oxide is calculated as a weighted sum of the heat capacities of the constituent oxides. Based on this rule, the molar heat capacity of a mixture is,

$$C_{pm(mixture)} = \sum_i C_{p(i)} x_i, \tag{20}$$

where $C_{p(i)}$ and x_i are the specific heat capacity and the mole fraction of component i of the mixture, respectively. The specific heat capacity of each component, namely CeO_2, UO_2, Gd_2O_3, and Er_2O_3 is estimated by the following equations which are suggested by Konings et al. [7], respectively.

$$C_{p(CeO_2)}(\mathrm{J \cdot mol^{-1} \cdot K^{-1}}) = 74.4814 + 5.83682 \times 10^{-3}(\mathrm{T/K}) - 1.29710 \times 10^{6}(\mathrm{T/K})^{-2}, \tag{21}$$

$$C_{p(UO_2)}(\mathrm{J \cdot mol^{-1} \cdot K^{-1}}) = 66.7437 + 43.1393 \times 10^{-3}(\mathrm{T/K}) - 35.64 \times 10^{-6}(\mathrm{T/K})^{2} + 11.655 \times 10^{-9}(\mathrm{T/K})^{3} - 1.16863 \times 10^{6}(\mathrm{T/K})^{-2}, \tag{22}$$

$$C_{p(Gd_2O_3)}(\mathrm{J \cdot mol^{-1} \cdot K^{-1}}) = 114.6104 + 15.2344 \times 10^{-3}(\mathrm{T/K}) - 1.24917 \times 10^{6}(\mathrm{T/K})^{-2}, \tag{23}$$

$$C_{p(Er_2O_3)}(\mathrm{J \cdot mol^{-1} \cdot K^{-1}}) = 123.2921 + 8.62245 \times 10^{-3}(\mathrm{T/K}) - 1.54433 \times 10^{6}(\mathrm{T/K})^{-2}. \tag{24}$$

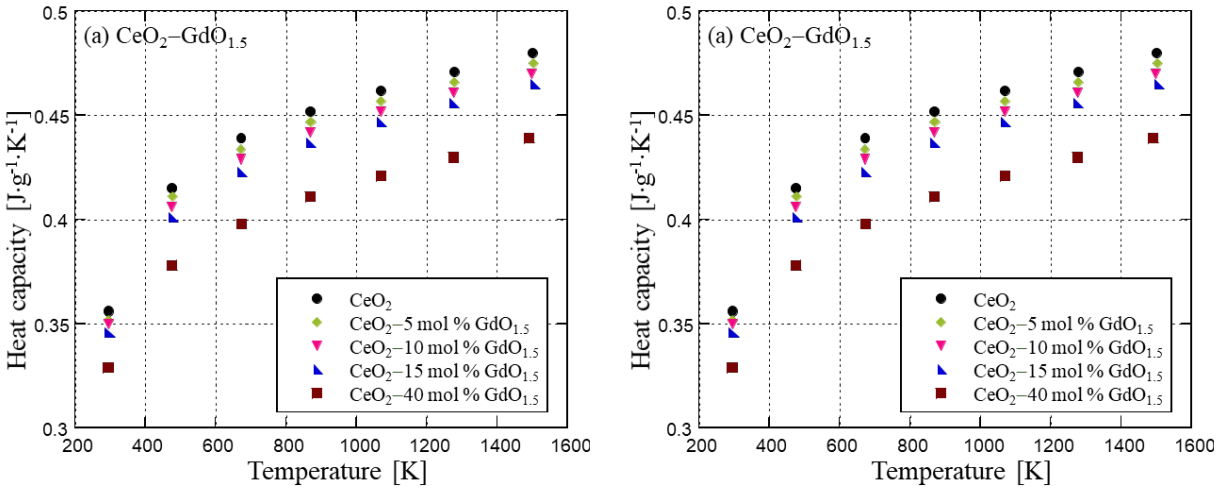

Figure 47. Heat capacities calculated by Neumann-Kopp rule for CeO_2–$LnO_{1.5}$ as functions of temperature and $LnO_{1.5}$ content.

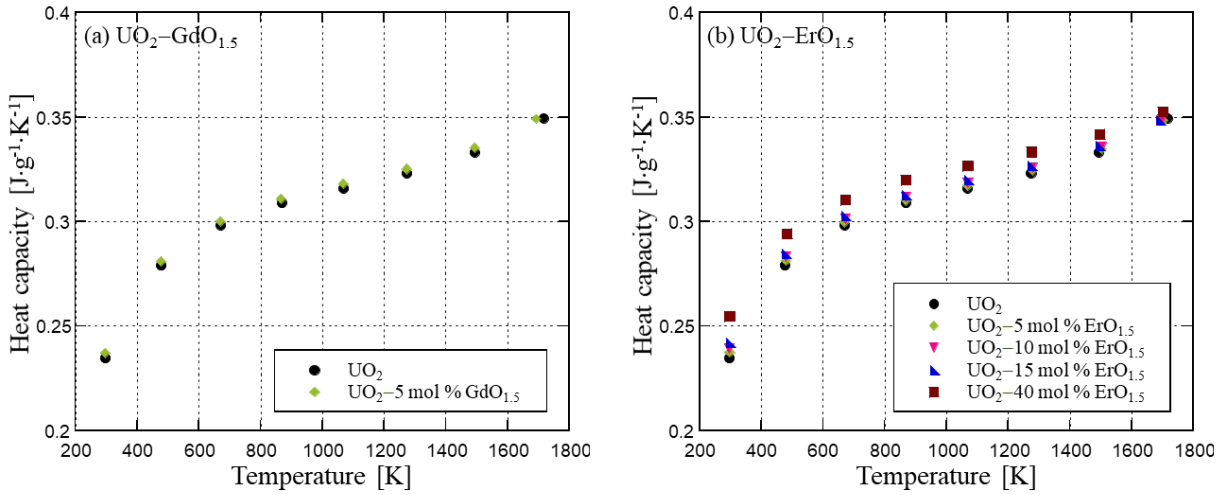

Figure 48. Heat capacities calculated by Neumann-Kopp rule for UO_2–$LnO_{1.5}$ as functions of temperature and $LnO_{1.5}$ content.

In the present study, the measured specific heat capacities of CeO_2–$GdO_{1.5}$ and UO_2–$LnO_{1.5}$ are the mean of three to five measurements with the relative standard deviations are less than ca. 1.5%. Figure 47 shows the heat capacities calculated by NKR for CeO_2–$LnO_{1.5}$ as functions of temperature and $LnO_{1.5}$ content. As an important thermo-physical property of materials, the heat capacity is defined as the amount of heat energy required to raise the temperature of a substance per unit of mass. Therefore, the heat capacity increased with temperatures. The effect of Ln doping was similar for both systems in that the specific heat capacity of CeO_2–$LnO_{1.5}$ decreased as $LnO_{1.5}$ content increased. Figure 48 shows the heat capacities of UO_2–$LnO_{1.5}$ estimated by NKR as functions of temperature and $LnO_{1.5}$ content. Heat capacity of UO_2–5 mol % $GdO_{1.5}$ was bigger than that of UO_2, and those of UO_2–$ErO_{1.5}$ samples increased with increasing $ErO_{1.5}$ up to 40 mol %. These results can be considered to be due to the heat capacities of $LnO_{1.5}$ solid

solutions are smaller than that of CeO_2 and greater than that of UO_2 at a temperature of less than 1800 K in this study.

4.4 Thermal diffusivities

Figure 49 shows the measured thermal diffusivities of CeO_2–$LnO_{1.5}$, which are averaged values of three to five measurements at each temperature over the temperature range from 290 K to 1500 K, as functions of temperature and $LnO_{1.5}$ content. These values were normalized to 96.5% TD. The thermal diffusivities of CeO_2–$LnO_{1.5}$ decreased with increasing $LnO_{1.5}$ content and temperature up to nearly 1500 K. For instance, the thermal diffusivity of CeO_2–5 mol % $GdO_{1.5}$ was about 39% lower than that of CeO_2 at a low temperature of nearly 300 K, while at a high temperature nearly 1500 K, the difference between the former and the latter is trivial. At high temperatures, thermal diffusivities of CeO_2–$LnO_{1.5}$ samples decreased gradually and slowly and seemed to be the same at above around 1200 K.

The errors in α values were determined through the propagation of error resulting from each of the three to five measurements. The specific values varied slightly for each temperature, but are indicated by the error bars in Fig. 49. In all cases, the calculated error was less than 5% so that the error bars were almost impossible to be seen in the figure.

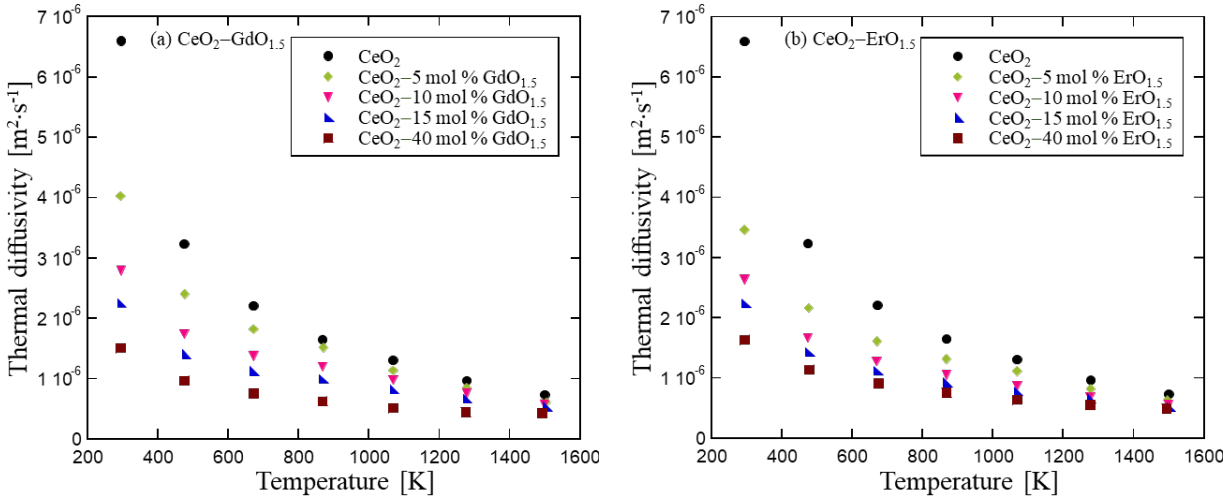

Figure 49. Thermal diffusivities of CeO_2–$LnO_{1.5}$ as functions of temperature and $LnO_{1.5}$ content (normalized to 96.5% TD).

Figure 50 shows the thermal diffusivity of CeO_2 compared with those of literature for CeO_2 as well as for UO_2. There were a few available literature data for CeO_2 measured by other investigators, but the temperature dependence observed was consistent. The thermal diffusivities of CeO_2 in this study were in good agreement with the experimental results reported by Khafizov et al. [9]. In addition, in comparison with experimental values measured by Hirai et al. [10], and Ronchi et al. [11], CeO_2 had a higher thermal diffusivity than that of UO_2 samples. In Fig. 50, it was found that there was a significant difference in the

thermal diffusivities between CeO_2 and UO_2 (also for PuO_2 reported by other researchers), especially at low-temperature regions whereas, the difference became small at high temperatures (> 1000 K).

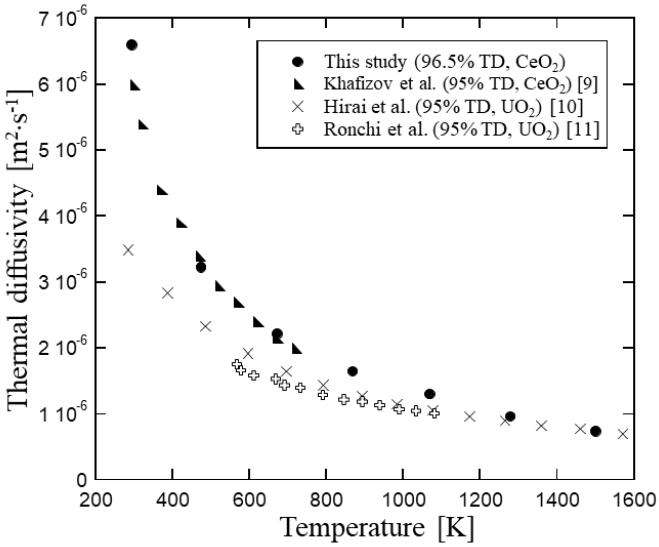

Figure 50. Thermal diffusivity of CeO_2 compared to other experimental data for CeO_2 [9] and UO_2 [10–11] as a function of temperature.

Figure 51 shows the measured thermal diffusivities of UO_2–$LnO_{1.5}$, which were normalized to 96.5% TD over the temperature range from 290 K to 1700 K, as functions of temperature and $LnO_{1.5}$ content. The thermal diffusivity of UO_2 agreed well with that of the literature [10]. Similar to the results obtained for CeO_2–$LnO_{1.5}$ systems, the thermal diffusivities of UO_2–$LnO_{1.5}$ decreased with increasing $LnO_{1.5}$ content and temperature up to 1700 K.

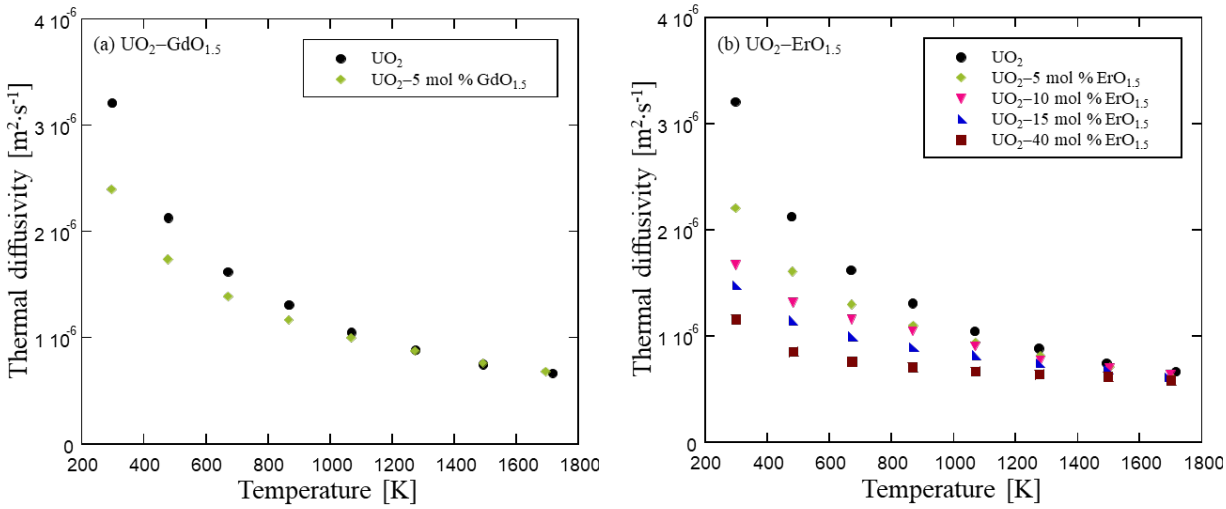

Figure 51. Thermal diffusivities of UO_2–$LnO_{1.5}$ as functions of temperature and $LnO_{1.5}$ content (normalized to 96.5% TD).

As indicated by Hirai et al. [10], the thermal diffusivity of a microcrack-free sample is higher than that of a micro cracked sample. Because of high thermal diffusivities, it is reasonable to assume that, our sintered

CeO_2–$LnO_{1.5}$ and UO_2–$LnO_{1.5}$ pellets had almost no microcracks. This was also confirmed by SEM observation. $LnO_{1.5}$ doping into CeO_2 and UO_2 reduced their grain sizes and formed pores. Thus, the decrease in the thermal diffusivities of CeO_2–$LnO_{1.5}$ and UO_2–$LnO_{1.5}$ as the $LnO_{1.5}$ content increased seems to be caused by geometrical effects such as oxygen vacancies, pores, and grain boundaries.

Although the thermal diffusivities of Gd_2O_3 and Er_2O_3 solid solutions have not been measured in the present study, it can be considered that the incorporation of Gd_2O_3 and Er_2O_3, those have lower thermal diffusivities into CeO_2 and UO_2 would considerably reduce the thermal diffusivities of such solid solutions. Another probable reason could lie in the difference in crystal structures between Gd_2O_3, Er_2O_3 and CeO_2, UO_2. As mentioned earlier that the structure of Gd_2O_3 and Er_2O_3 is C-type cubic, which is manifested out of ordering of a large anion vacancy i.e., oxygen vacancies in Ln_2O_3's hypothetical defective fluorite structure. It was known that the lattice vacancies in crystalline materials affect thermal expansion and the thermal diffusivity. As a result, as more Ln_2O_3 is added into CeO_2, and UO_2, the number of oxygen vacancies increased, which in turn decreased the thermal expansion coefficient, and the thermal diffusivity as well. The behaviors of the thermal diffusivities relating to temperature and $LnO_{1.5}$ content are discussed with those of the thermal conductivities in the next section.

4.5 Thermal conductivities

The thermal conductivities (k) of CeO_2–$LnO_{1.5}$ and UO_2–$LnO_{1.5}$ measured directly by LFA over the temperature range from room temperature to nearly 1700 K are summarized in Tables 9, and 10, together with heat capacity (C_p) and the thermal diffusivity (α) data, as the averaged values of three to five measurements at each temperature step. The relative standard deviations for the thermal conductivities from experiments were a few percent.

Table 9. The thermal property data of CeO_2–$LnO_{1.5}$ solid solutions determined in this study

$LnO_{1.5}$ content [mol %]	T [K]	α [$\times 10^{-6}$ $m^2 \cdot s^{-1}$]	LFA		NKR	
			C_p [$J \cdot g^{-1} \cdot K^{-1}$]	k [$W \cdot m^{-1} \cdot K^{-1}$]	C_p [$J \cdot g^{-1} \cdot K^{-1}$]	k [$W \cdot m^{-1} \cdot K^{-1}$]
Gd, 0.0	294.5	6.5980 ± 0.0113	0.380	17.0727 ± 0.7104	0.356	16.1400 ± 0.0045
	474.5	3.2341 ± 0.0624	0.429	9.4443 ± 0.2007	0.415	9.2350 ± 0.0259
	671.8	2.2133 ± 0.0078	0.431	6.4879 ± 0.0551	0.439	6.6771 ± 0.0035
	868.5	1.6468 ± 0.0226	0.455	4.6066 ± 0.1134	0.452	5.1195 ± 0.0102
	1069.2	1.3087 ± 0.0217	0.465	4.1445 ± 0.1030	0.462	4.1601 ± 0.0101
	1277.8	0.9700 ± 0.0475	0.461	3.0774 ± 0.0987	0.471	3.1439 ± 0.0224
	1500.4	0.7368 ± 0.0183	0.433	2.0912 ± 0.0572	0.480	2.4327 ± 0.0088
Gd, 5.0	293.9	4.0324 ± 0.0715	0.399	11.5703 ± 0.3279	0.352	9.9219 ± 0.0252
	476.8	2.4058 ± 0.0078	0.457	7.8552 ± 0.1504	0.411	6.9100 ± 0.0033
	670.8	1.8213 ± 0.0096	0.467	5.9660 ± 0.0503	0.434	5.5190 ± 0.0042
	870.2	1.5198 ± 0.0062	0.486	5.1358 ± 0.0366	0.447	4.7481 ± 0.0029
	1068.9	1.1383 ± 0.0158	0.488	3.8940 ± 0.982	0.457	3.6366 ± 0.0072
	1277.8	0.8487 ± 0.0351	0.453	2.7001 ± 0.2059	0.466	2.7652 ± 0.0164
	1504.5	0.6106 ± 0.0125	0.190	0.7601 ± 0.0553	0.475	2.0279 ± 0.0060

Table 9. The thermal property data of CeO_2–$LnO_{1.5}$ solid solutions determined in this study (cont.)

$LnO_{1.5}$ content [mol %]	T [K]	α [$\times 10^{-6}$ $m^2 \cdot s^{-1}$]	LFA	NKR	$LnO_{1.5}$ content [mol %]	T [K]
Gd, 10.0	295.2	2.7936 ± 0.0522	0.372	7.0727 ± 0.3615	0.350	6.8396± 0.0183
	474.2	1.7464 ± 0.0111	0.439	5.2157 ± 0.0704	0.406	4.9648 ± 0.0045
	671.5	1.3772 ± 0.0132	0.440	4.1217 ± 0.1047	0.429	4.1347 ± 0.0057
	868.2	1.2016 ± 0.0045	0.429	3.4932 ± 0.0252	0.442	3.7183 ± 0.0020
	1069.2	0.9828 ± 0.0073	0.479	3.2040 ± 0.0486	0.452	3.1117 ± 0.0033
	1277.2	0.7585 ± 0.0041	0.486	2.5108 ± 0.0230	0.461	2.4496 ± 0.0019
	1498.8	0.5800 ± 0.0125	0.428	1.6900 ± 0.0760	0.470	1.9094 ± 0.0059
Gd, 15.0	294.2	2.2572 ± 0.0234	0.375	6.2572 ± 0.3213	0.346	5.4259 ± 0.0081
	476.2	1.4097 ± 0.0124	0.422	4.1003 ± 0.0721	0.401	3.9366 ± 0.0050
	670.2	1.1306 ± 0.0041	0.452	3.5240 ± 0.0210	0.423	3.3296 ± 0.0018
	867.5	0.9944 ± 0.0286	0.474	3.3617 ± 0. 1728	0.437	3.0195 ± 0.0125
	1068.8	0.8300 ± 0.0106	0.502	2.9058 ± 0.0633	0.447	2.5793 ± 0.0047
	1275.2	0.6739 ± 0.0096	0.493	2.3161 ± 0.0597	0.456	2.1365 ± 0.0044
	1504.2	0.5335 ± 0.0230	0.435	1.6002 ± 0.1263	0.465	1.7256 ± 0.0107
Gd, 40.0	293.8	1.5075 ± 0.0102	0.357	3.7805 ± 0.0859	0.329	3.4830 ± 0.0034
	474.9	0.9649 ± 0.0124	0.389	2.5543 ± 0.0261	0.378	2.5610 ± 0.0047
	672.2	0.7611 ± 0.0041	0.413	2.1383 ± 0.0048	0.398	2.1294 ± 0.0016
	867.5	0.6254 ± 0.0286	0.417	1.7770 ± 0.0241	0.411	1.8048 ± 0.0117
	1069.2	0.5128 ± 0.0016	0.483	1.6858 ± 0.0097	0.421	1.5165 ± 0.0007
	1275.2	0.4445 ± 0.0024	0.507	1.5432 ± 0.0147	0.430	1.3432 ± 0.0010
	1491.5	0.4321 ± 0.0087	0.548	1.5680 ± 0.0672	0.439	1.3330 ± 0.0038
Er, 5.0	294.2	3.4653 ± 0.0464	0.375	9.8344 ± 0.0836	0.352	8.4843 ± 0.0164
	475.9	2.1642 ± 0.0164	0.457	7.0252 ± 0.1588	0.411	6.1814 ± 0.0068
	670.5	1.6139 ± 0.0070	0.434	4.8490 ± 0.0211	0.433	4.8635 ± 0.0031
	867.7	1.3185± 0.0078	0.433	3.9571 ± 0.1572	0.446	4.0943 ± 0.0035
	1068.8	1.1171 ± 0.0185	0.481	3.8212 ± 0.1361	0.456	3.5469 ± 0.0085
	1278.2	0.8226 ± 0.0051	0.481	2.7428 ± 0.0362	0.465	2.6629 ± 0.0024
	1494.9	0.6362 ± 0.0132	0.426	1.8791 ± 0.0895	0.474	2.0969 ± 0.0063
Er, 10.0	294.0	2.6382 ± 0.0163	0.366	6.9082 ± 0.3399	0.348	6.4162 ± 0.0057
	474.4	1.6738 ± 0.0030	0.424	4.9234 ± 0.1120	0.405	4.7386 ± 0.0014
	670.2	1.2754 ± 0.0102	0.422	3.7292 ± 0.0396	0.428	3.8100 ± 0.0044
	868.2	1.0523 ± 0.0005	0.435	3.1704 ± 0.1255	0.441	3.2387 ± 0.0005
	1069.2	0.8763 ± 0.0027	0.468	2.8448 ± 0.0204	0.450	2.7571 ± 0.0013
	1276.4	0.7136 ± 0.0063	0.463	2.2185 ± 0.3026	0.459	2.2886 ± 0.0029
	1499.5	0.5550 ± 0.0111	0.444	1.7089 ± 0.0664	0.468	1.8128 ± 0.0052
Er, 15.0	294.4	2.2433 ± 0.0256	0.377	5.8614 ± 0.2664	0.345	5.4168 ± 0.0089
	476.2	1.4339 ± 0.0019	0.408	4.0540 ± 0.0116	0.401	4.0232 ± 0.0009
	670.5	1.1244 ± 0.0033	0.429	3.3425 ± 0.0221	0.422	3.3248 ± 0.0014
	868.4	0.9343 ± 0.0077	0.446	2.8852 ± 0.1234	0.435	2.8457 ± 0.0034
	1068.4	0.7820 ±0.0094	0.479	2.6393 ± 0.0656	0.444	2.4342 ± 0.0042
	1275.5	0.6655 ± 0.0061	0.500	2.3439 ± 0.0476	0.453	2.1111 ± 0.0028
	1502.2	0.5165 ± 0.0119	0.450	1.6102 ± 0.0894	0.461	1.6692 ± 0.0055
Er, 40.0	294.4	1.6363 ± 0.0195	0.321	3.7222 ± 0.2137	0.326	3.8508 ± 0.0064
	477.8	1.1417 ± 0.0037	0.402	3.2535 ± 0.0448	0.376	3.0927 ± 0.0015
	673.5	0.9118 ± 0.0021	0.394	2.5453 ± 0.0071	0.395	2.5956 ± 0.0010
	868.2	0.7617 ± 0.0154	0.401	2.1666 ± 0.1683	0.406	2.2292 ± 0.0063
	1068.7	0.6403 ± 0.0033	0.458	2.0902 ± 0.0149	0.415	1.9139 ± 0.0014
	1276.2	0.5622 ± 0.0039	0.478	1.9425 ± 0.0386	0.422	1.7117 ± 0.0017
	1492.7	0.4944 ± 0.0087	0.437	1.5328 ± 0.0589	0.430	1.5317 ± 0.0037

Table 10. The thermal property data of UO_2–$LnO_{1.5}$ solid solutions determined in this study

$LnO_{1.5}$ content [mol %]	T [K]	α [$\times 10^{-6}$ $m^2 \cdot s^{-1}$]	LFA		NKR	
			C_p [$J \cdot g^{-1} \cdot K^{-1}$]	k [$W \cdot m^{-1} \cdot K^{-1}$]	C_p [$J \cdot g^{-1} \cdot K^{-1}$]	k [$W \cdot m^{-1} \cdot K^{-1}$]
Gd, 0.0	296.2	3.2136	0.250	8.1355	0.2347	7.8407
	477.7	2.1311	0.304	6.5533	0.2791	6.1836
	670.9	1.6177	0.311	5.0890	0.2984	5.0178
	868.4	1.3133	0.312	4.1518	0.3089	4.2173
	1068.4	1.0511	0.338	3.5990	0.3160	3.4534
	1275.2	0.8861	0.349	3.1315	0.3231	2.9765
	1493.2	0.7476	0.266	2.0183	0.3332	2.5897
	1717.0	0.6663	0.075	0.5092	0.3494	2.4203
Gd, 5.0	295.2	2.4032	0.269	6.3495	0.2370	5.7749
	476.4	1.7441	0.315	5.4073	0.2810	4.9699
	670.4	1.3897	0.329	4.4893	0.3002	4.2307
	865.9	1.1690	0.319	3.6613	0.3108	3.6832
	1067.2	0.9995	0.339	3.3290	0.3181	3.2237
	1273.2	0.8782	0.352	3.0398	0.3253	2.8961
	1492.2	0.7619	0.358	2.6848	0.3353	2.5908
	1694.2	0.6851	0.084	0.5621	0.3493	2.4264
Er, 5.0	297.2	2.2098	0.262	5.5536	0.2375	5.2691
	479.8	1.1611	0.307	4.7441	0.2812	4.5491
	671.0	1.3035	0.319	3.9780	0.2999	3.9240
	868.9	1.0966	0.324	3.4067	0.3103	3.4159
	1069.8	0.9439	0.361	3.2643	0.3174	3.0077
	1278.9	0.8175	0.366	2.8648	0.3245	2.6631
	1503.9	0.7124	0.089	0.6053	0.3348	2.3947
	1701.7	0.6260	0.059	0.3374	0.3486	2.1908
Er, 10.0	296.2	1.6696	0.223	3.3360	0.2395	3.9792
	481.5	1.3171	0.259	3.1408	0.2833	3.7125
	671.5	1.1583	0.287	2.8978	0.3014	3.4742
	868.4	1.0465	0.286	2.6293	0.3117	3.2454
	1069.3	0.9082	0.331	2.6590	0.3188	2.8808
	1279.9	0.7802	0.334	2.4937	0.3258	2.5297
	1503.0	0.7068	0.194	1.7345	0.3358	2.3620
	1699.3	0.6419	0.066	0.3762	0.3490	2.2288
Er, 15.0	296.2	1.4783	0.230	3.1580	0.2419	3.4831
	478.4	1.1470	0.275	2.8483	0.2846	3.1797
	670.2	1.0002	0.288	2.7468	0.3028	2.9500
	867.2	0.9010	0.289	2.4709	0.3130	2.7466
	1068.2	0.8249	0.323	2.6184	0.3201	2.5712
	1275.2	0.7515	0.334	2.4031	0.3269	2.3928
	1494.4	0.6880	0.257	1.2817	0.3364	2.2542
	1689.4	0.6163	0.061	0.3892	0.3488	2.0933
Er, 40.0	297.7	1.1558	0.267	2.4027	0.2546	2.4685
	484.0	0.8537	0.314	2.0860	0.2944	2.1086
	672.8	0.7615	0.329	1.9503	0.3105	1.9837
	868.2	0.7089	0.331	1.8249	0.3199	1.9029
	1070.1	0.6715	0.357	1.8683	0.3268	1.8412
	1275.8	0.6453	0.370	1.8614	0.3333	1.8046
	1497.7	0.6220	0.379	1.8355	0.3418	1.7836
	1701.5	0.5834	0.260	1.1847	0.3525	1.7254

In this study, as mentioned earlier, C_p data calculated by NKR were also used to estimate the thermal conductivity. Both thermal conductivity values, measured and estimated data were normalized to 96.5% TD. The obtained thermal conductivities were normalized to 96.5% TD using the following Eq. (25),

$$k_{TD} = k_M \frac{1 - P_{TD}}{1 - P_M}. \tag{25}$$

In Eq. (25), k_{TD} is the thermal conductivity for the density of interest, i.e., normalized to the desired density of theoretical density, k_M is the experimentally measured thermal conductivity, P_{TD} is the volumetric pore fraction for the density of interest, and P_M is volumetric fraction by experiments. Recalling that (1 - P) is equivalent to % $TD \times 0.01$, it is possible to quickly assess the effects of density on the thermal conductivity. Figure 52 and figure 53 show the estimated thermal conductivities of CeO_2–$LnO_{1.5}$, and UO_2–$LnO_{1.5}$ samples, as functions of temperature and $LnO_{1.5}$ content. The calculated error was small (less than 1 %). Thermal conductivities of both CeO_2–$LnO_{1.5}$ and UO_2–$LnO_{1.5}$ systems decreased systematically with temperature and decreased with increasing $LnO_{1.5}$ content at any temperatures investigated. In the present case, the presence of $LnO_{1.5}$ is an additional factor that degrades k of CeO_2 and UO_2. The impurity-induced point defects are responsible for the reduction in k. According to this idea, k of CeO_2–$LnO_{1.5}$ and UO_2–$LnO_{1.5}$ is dependent on the homogeneity of the sample, i.e., the concentration of dopant $LnO_{1.5}$ in CeO_2 and UO_2.

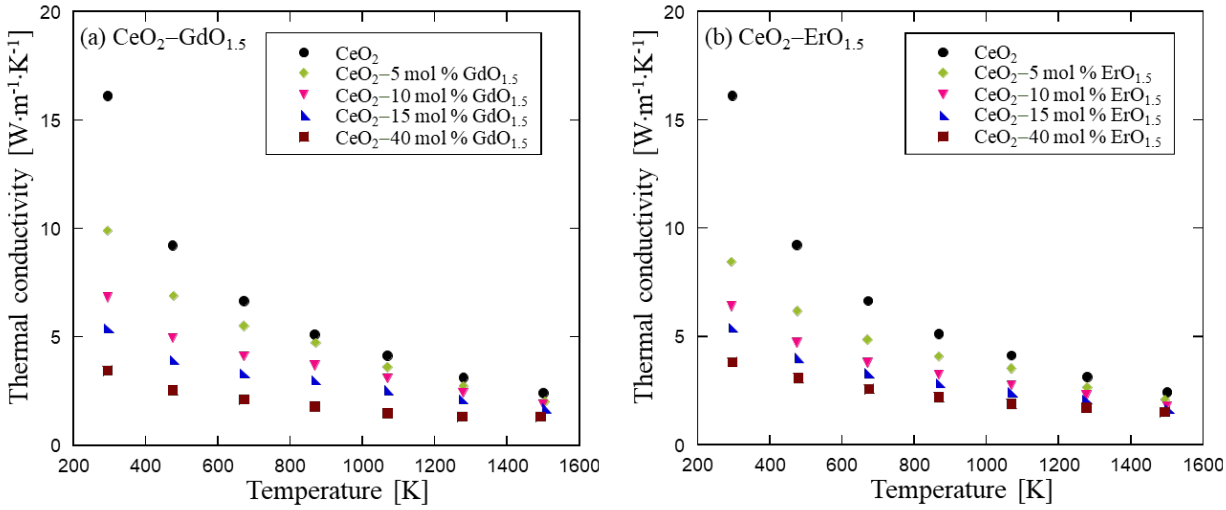

Figure 52. The estimated thermal conductivities of CeO_2–$LnO_{1.5}$ as functions of temperature and $LnO_{1.5}$ content (normalized to 96.5% TD).

In addition, k decreased gradually with temperature up to nearly 1500 K for CeO_2–$LnO_{1.5}$ and up to 1700 K for and UO_2–$LnO_{1.5}$, and the decreasing rates became relatively smaller at a higher temperature. At low temperatures, they decreased rapidly with $LnO_{1.5}$ addition. For example, k of CeO_2 decreased sharply from

approximately 16 to just over 4 $W \cdot m^{-1} \cdot K^{-1}$ with the addition of 40 mol % $LnO_{1.5}$ at nearly 300 K. At high temperatures, thermal conductivities of the samples decreased slowly, especially at above 1000 K.

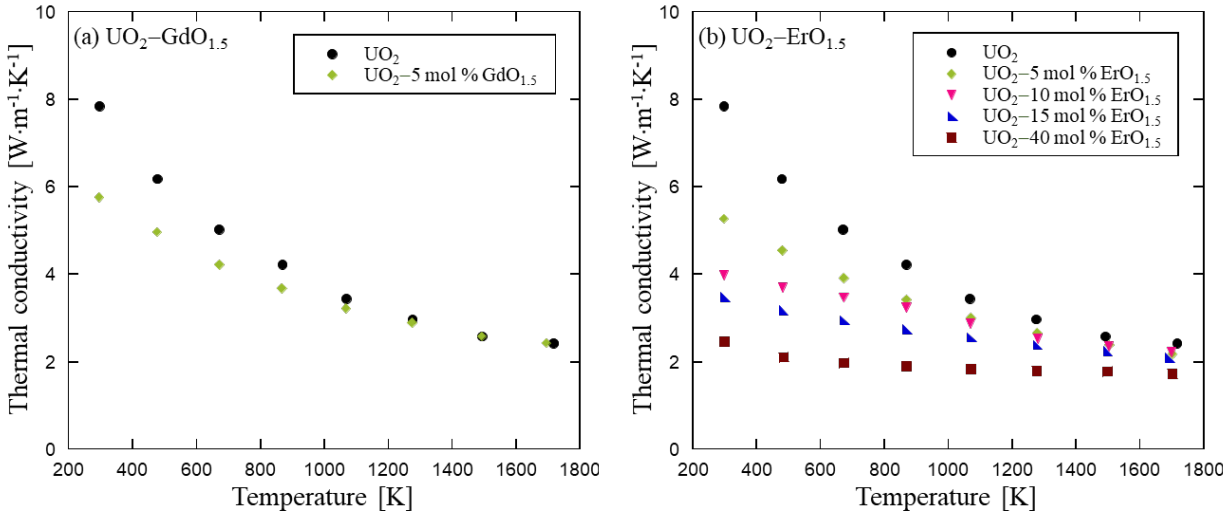

Figure 53. The estimated thermal conductivities of UO_2–$LnO_{1.5}$ as functions of temperature and $LnO_{1.5}$ content (normalized to 96.5% TD).

The inverse of the low-temperature thermal conductivity (so-called thermal resistivity, $1/k$) for solid solutions can be expressed as a function of temperature using the fitting function ($A + BT$) by the following equation,

$$1/k = A + BT, \tag{26}$$

where T is absolute temperature, A and B are constants. A is the thermal resistivity caused by phonon-lattice defect interactions, and B is the thermal resistivity caused by phonon-phonon scattering based on the Umklapp processes. This approximating simplification of temperature dependence was proposed based on the difficulty of incorporating the complex temperature dependences of phonon scattering in crystalline solids suggested by Roufosse and Klemens et al. [12]. The values of A and B were determined by fitting the experimental data from 290 K to 1700 K to Eq. (26) using the least-squares method. Table 11 summarizes the calculated values of A and B for CeO_2–$LnO_{1.5}$ and UO_2–$LnO_{1.5}$ samples. The value of A increased gradually with $LnO_{1.5}$ content, while that of B was insensitive to it. As shown in Figs. 54 and 55, the thermal resistivity increases with temperature, and the relation between them is well expressed in Eq. (26).

Table 11. Measured values of A and B for CeO_2–$LnO_{1.5}$ and UO_2–$LnO_{1.5}$ samples in the present study

$LnO_{1.5}$ content [mol %]	A [$\times 10^2$ m·K·W^{-1}]	B [$\times 10^{-2}$ m·W^{-1}]	Temperature range [K]	R constant
CeO_2	-3.2011	0.0278	294.5 ~ 1500.4	0.99109
CeO_2–5 mol % $GdO_{1.5}$	-1.7663	0.0304	293.9 ~ 1504.5	0.9708
CeO_2–10 mol % $GdO_{1.5}$	4.8004	0.0288	295.2 ~ 1498.8	0.97796
CeO_2–15 mol % $GdO_{1.5}$	8.5747	0.0308	294.2 ~ 1504.2	0.98833
CeO_2–40 mol % $GdO_{1.5}$	19.475	0.0405	293.8 ~ 1491.5	0.98701
CeO_2–5 mol % $ErO_{1.5}$	1.7326	0.0283	292.2 ~ 1494.9	0.98101
CeO_2–10 mol % $ErO_{1.5}$	5.4104	0.0311	294.0 ~ 1499.5	0.99017
CeO_2–15 mol % $ErO_{1.5}$	8.3844	0.0322	294.4 ~ 1502.2	0.99143
CeO_2–40 mol % $ErO_{1.5}$	16.467	0.0329	294.4 ~ 1492.7	0.99976
UO_2	6.2006	0.0210	296.2 ~ 1717.0	0.99789
UO_2–5 mol % $GdO_{1.5}$	12.016	0.0175	295.2 ~ 1694.2	0.99938
UO_2–5 mol % $ErO_{1.5}$	12.853	0.0192	297.2 ~ 1701.7	0.99971
UO_2–10 mol % $ErO_{1.5}$	19.523	0.0149	296.2 ~ 1699.3	0.99171
UO_2–15 mol % $ErO_{1.5}$	24.876	0.0133	296.2 ~ 1689.4	0.99927
UO_2–40 mol % $ErO_{1.5}$	41.340	0.0107	297.7 ~ 1701.5	0.92882

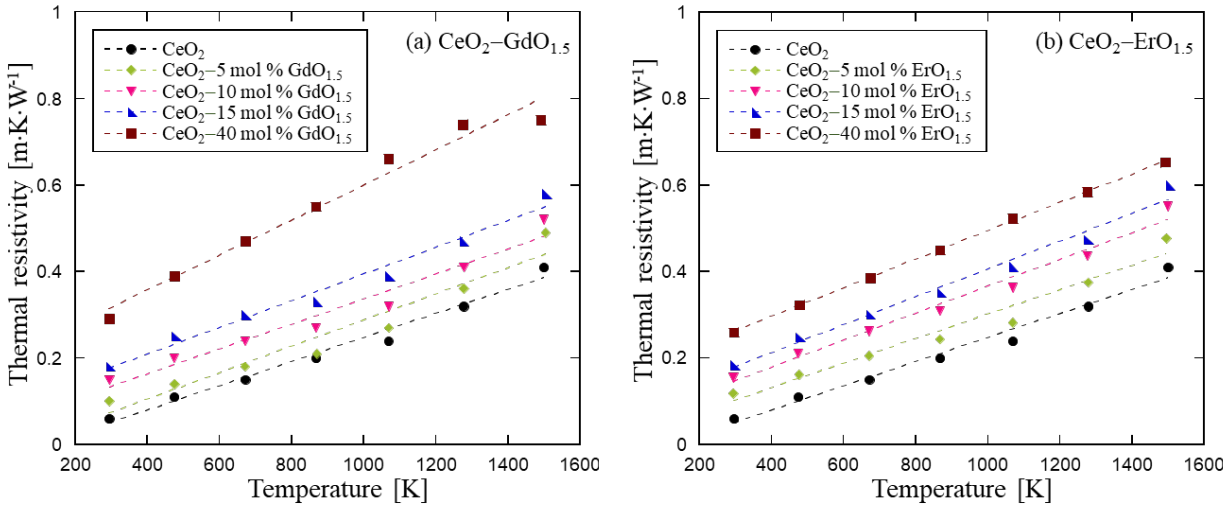

Figure 54. The thermal resistivities of CeO_2–$LnO_{1.5}$ as a function of temperature (normalized to 96.5% TD). Dashed lines were determined by fitting the thermal conductivity, k, to the relation $1/k = A + BT$.

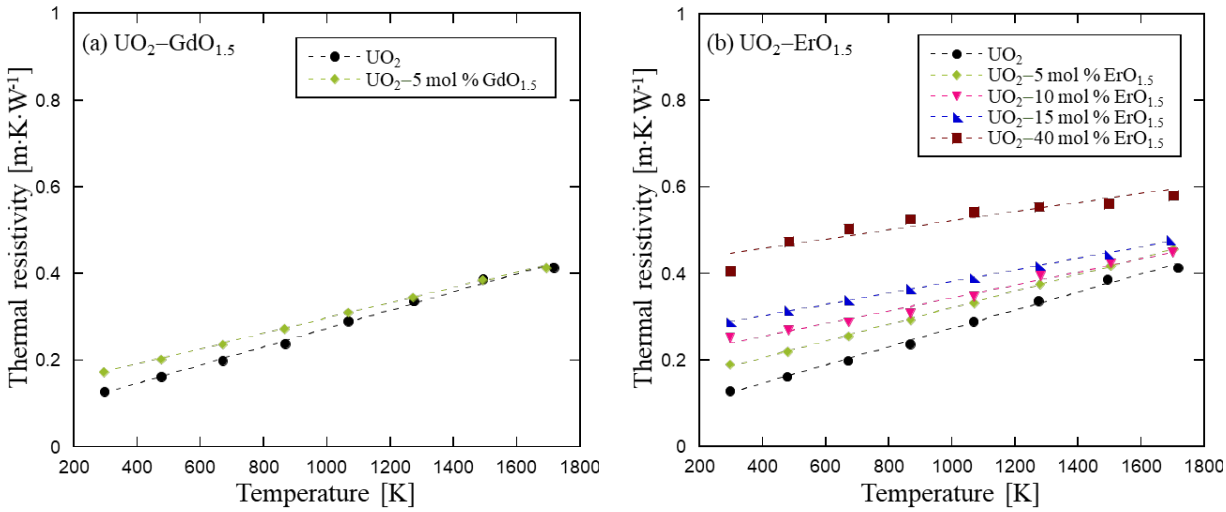

Figure 55. The thermal resistivities of UO_2–$LnO_{1.5}$ as a function of temperature (normalized to 96.5% TD). Dashed lines were determined by fitting the thermal conductivity, k, to the relation $1/k = A + BT$.

For the temperature-independent phonon lattice defect scattering, A, its values are more complex and may be related to physical phenomena. In this case, where cation Ln substituted randomly on the Ce or U cation lattice sites of the host crystal structure, calculation using a fitting function ($A + BT$) showed a significant increase in A values with additional $LnO_{1.5}$ content, while B values were mostly constant. It is known that the lattice defect thermal resistivity depends on the scattering cross-section of the phonons by point defect. The scattering cross-section parameter depends on the differences of mass, bonding force, and atomic size between the point defect and the host atom in the lattice ($LnO_{1.5}$ and CeO_2 or UO_2, respectively). In the present study, the mass difference between Ce, U and Ln atoms, and the ionic radius difference between Ce^{4+}, U^{4+}, and Ln^{3+} cations can be considered as the phonon scattering which results in the increase of lattice defect thermal resistivity, A.

According to the micro-mechanism of thermal conduction, the thermal conductivity of a nonmetallic material is the result of phonon collisions or scattering. Because CeO_2–$LnO_{1.5}$ and UO_2–$LnO_{1.5}$ solid solution samples in this study are nonmetallic and carry no free electrons, the heat is transported predominantly by phonons and photons. The theoretical expression for k_P is,

$$k_P = \frac{1}{3} C_p \cdot \nu_P \cdot l_P \cdot \rho, \tag{27}$$

Where ν_P is the phonon velocity, l_P is the phonon mean free path of a phonon between collisions. Comparing Eq. (27) with Eq. (13), the thermal diffusivity α is written by:

$$\alpha = \frac{1}{3} \nu_P \cdot l_P. \tag{28}$$

As mentioned earlier, C_p of CeO_2–$LnO_{1.5}$ decreased slightly and those of UO_2–$LnO_{1.5}$ increased slightly with increasing $LnO_{1.5}$ content. C_p is almost a constant when the temperature is upon Debye temperature. For the density, it increased slightly with $LnO_{1.5}$ addition. The value of k is, therefore, mostly dependent on the thermal diffusivity, α. The phonon velocity is the average sound velocity which is calculated from the longitudinal sound velocity, v_L, and the shear sound velocity, v_S, by the following equation,

$$v_P = \left[\frac{1}{3}\left(\frac{1}{v_L^3} + \frac{2}{v_S^3}\right)\right]^{-1/3}. \tag{29}$$

The longitudinal and shear sound velocities in the samples were measured by the ultrasonic pulse-echo method and in detail discussed in Section 5. Since the sound velocity in solids generally changes depending on the density, temperature, and chemical composition, etc., the phonon velocity also changes with them. It is, however, experimentally confirmed that the effects of the density and the chemical composition on phonon velocity are small for the CeO_2–$GdO_{1.5}$ samples. Thus, the values of α are mostly determined by l_P, which is the average traveling distance between two consecutive phonon scattering events (collisions).

The phonon mean free path, l_P, is determined principally by two processes, scattering by other phonons, and geometrical scattering. For the scattering by other phonons, we can understand this dependence in terms of the number of phonons with which a given phonon can interact: at high temperature, the total number of excited phonons is proportional to temperature, T. The collision frequency of a given phonon should be proportional to the number of phonons with which it can collide, whence l_P is proportional to T^{-1}. Unfortunately, we could not discuss the temperature dependence of l_P anymore because its dependence of phonon velocity was not evaluated.

For the geometrical effects (or the imperfections of crystals), it may also be important in limiting the mean free path. It is necessary to consider phonon scattering by grain boundaries, chemical impurities, the distribution of isotopic masses in natural chemical elements, lattice imperfections, and amorphous structures. According to Eq. (27), the l_P was calculated by thermal conductivities, heat capacities, densities, and averaged sound velocities in the samples measured at room temperature. Figure 56 shows the calculated phonon mean free path of CeO_2–$GdO_{1.5}$ up to 15 mol % of $GdO_{1.5}$. Firstly, the l_P of CeO_2–$GdO_{1.5}$ obtained in this study was approx. 2–5 nm and was much smaller than the average grain size (approx. 5–30 μm), consequently, the grain boundaries showed no effects on limiting l_P. As shown in Figs. 12–15, since the surface of the samples was not fully uniform, it could affect the measurements of thermal properties. However, as l_P of the samples was much smaller than its average grain size, the effect of the deviation of grain size distribution can be considered to be small and neglected. Secondly, in the present study, as commercial-high purity reagent UO_2, CeO_2, Gd_2O_3, and Er_2O_3 were used to prepare pellets in a clean laboratory, the effects of phonon scattering caused by the chemical impurities on l_P can be neglected. In addition, the distribution of isotopes of the chemical elements often provides an important mechanism for

phonon scattering. Especially Gd has ^{154}Gd–^{160}Gd isotopes in natural, however, the difference in atomic weight is relatively small. Therefore, the isotope effect is anticipated to be trivial. At low temperatures, the chemical composition dependence of thermal conductivity was remarkably large for the samples. This is the reason why the imperfection effect caused by $LnO_{1.5}$ addition becomes dominant and decreases their thermal conductivities. As more $LnO_{1.5}$ is added into UO_2 or CeO_2, U^{4+} or Ce^{4+} ions were partly substituted by Ln^{3+} ions, the number of oxygen vacancies (oxygen defect) increased, l_P decreased which in turn decreased the thermal conductivity.

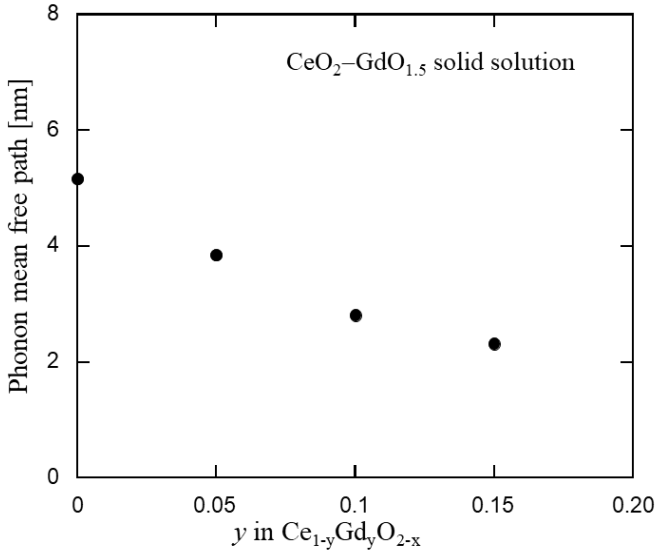

Figure 56. Phonon mean free path of CeO_2–$GdO_{1.5}$ calculated from sound velocities, those were measured at room temperature, as a function of $GdO_{1.5}$ content.

It is considered that thermal radiation becomes a significant factor in the measurement of the thermal diffusivity and thermal conductivity at high temperatures. In this study, the effect of radiation was not taken into consideration because I used solid solution samples with high relative densities. Moreover, all measurements were carried out over the temperature range of equal or less than 1700 K. Therefore, the effect of radiation on the thermal diffusivity and thermal conductivity measured at low and middle temperatures in this study can be considered to be small. In addition, at all temperatures investigated, the thermal diffusivity and thermal conductivity data were obtained directly by measurements in which only conduction was taken into account for heat transfer.

The thermal conductivities for CeO_2 sample obtained in the present study are shown in Fig. 57, together with literature data of CeO_2, UO_2, ThO_2, and PuO_2 [9,11,13–15]. It was found that the thermal conductivity of CeO_2 was in good agreement with the experimental results reported by Khafizov et al. [9]. In comparison with other fluorite oxides, CeO_2 showed the highest thermal conductivity whereas they decreased in the order of ThO_2, PuO_2, and UO_2. This could be explained by the spin-phonon scattering which causes a decrease in thermal conductivity. Considering the electronic structures of these fluorite oxides, bulk CeO_2 and ThO_2 have no f-electrons, and UO_2 and PuO_2 have two and four f-electrons, respectively. The effect of

phonon scattering due to spin which may originate from f-electron(s) is considered to be negligible for CeO_2 and ThO_2 [16,17] so that these thermal conductivities are relatively high. The magnetic property of UO_2 is anti-ferromagnetic, and some literature report that the spin-phonon scattering decreases the thermal conductivity of UO_2 [17,18]. On the other hand, paramagnetism behavior can be observed for PuO_2, and its magnetic susceptibility is much lower than that of UO_2 [19,20]. Thus, the thermal conductivities of UO_2 may be lower than that of PuO_2. Moreover, the thermal conductivities of UO_2–$LnO_{1.5}$ samples agreed well with those of the literature [21–24].

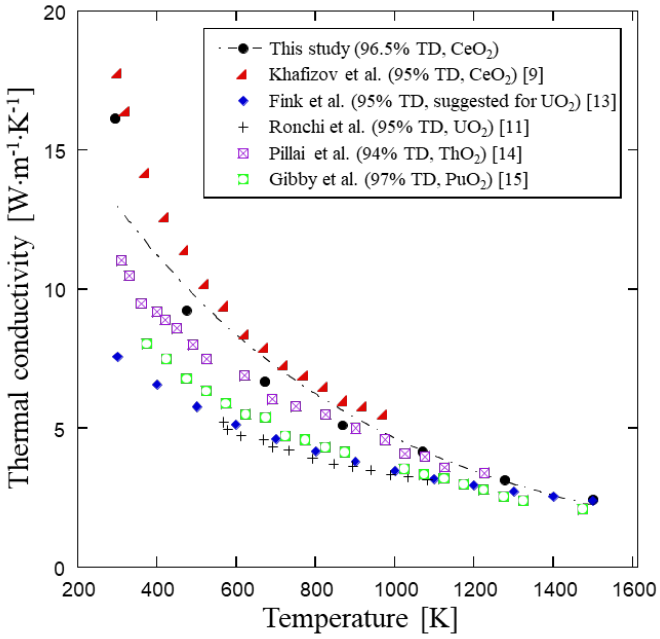

Figure 57. Thermal conductivity data obtained for 96.5% TD of CeO_2 compared to the literature data for CeO_2, UO_2, ThO_2, and PuO_2 as a function of temperature. The dashed line is a guide to the eye.

4.6 Summary

The heat capacities, the thermal diffusivities, and thermal conductivities of CeO_2–$LnO_{1.5}$ and UO_2–$LnO_{1.5}$ solid solution samples were simultaneously measured by LFA technique over the temperature range from room temperature to 1700 K and then the changes in these thermal properties were evaluated as functions of temperature and $LnO_{1.5}$ content. The heat capacity was also calculated by NKR to compared with that measured by LFA.

The results show that the heat capacities of CeO_2–$LnO_{1.5}$ decreased, whereas those of UO_2–$LnO_{1.5}$ increased as $LnO_{1.5}$ content increased up to 40 mol%. In both CeO_2–$LnO_{1.5}$ and UO_2–$LnO_{1.5}$ solid solutions, the measured heat capacities by LFA are comparable with the values estimated by NKR.

The thermal diffusivity of the samples depended on geometrical effects such as microcracks, oxygen vacancies, pores, and grain boundaries of the lattice. The thermal diffusivities of CeO_2–$LnO_{1.5}$ and

UO_2–$LnO_{1.5}$ samples decreased with temperature up to nearly 1700 K, and they also decreased with the $LnO_{1.5}$ content up to 40 mol %.

The thermal conductivities of CeO_2–$LnO_{1.5}$ and UO_2–$LnO_{1.5}$ samples decreased with temperature up to nearly 1700 K. In addition, the thermal conductivities of both solid solutions decreased as the $LnO_{1.5}$ content increased up to 40 mol %. Thermal conductivities of the samples were mostly determined by phonon mean free path in the samples. At high temperatures, the phonon mean free path decreased due to the Umklapp processes, the effect of $LnO_{1.5}$ doping was, however, small. At low temperatures, the increase of phonon scattering, i.e., the reduction of phonon mean free path, was caused by the increase of dopant $LnO_{1.5}$ and oxygen vacancies, which in turn decreased the thermal conductivity of the samples. On the other hand, phonon scattering caused by grain boundaries, and chemical impurities can be neglected, and the isotope effect is considered to be small in the samples in the present study.

4.7 References

[1] W.J. Parker, R.J. Jenkins, C.P. Butler, G.L. Annott, J. Appl. Phys. 32 (1961) 1679–1684.

[2] D. Josell, J. Warren, A. Cezairliyan, J. Appl. Phys. 78 (1995) 6867–6869.

[3] P.V. Mao, T. Arima, Y. Inagaki, K. Idemitsu, Proceedings of 27th International Conference on Nuclear Engineering (2019), Paper No. ICONE27–1927.

[4] S. Sameshima, M. Kawaminami, Y. Hirata, J. Ceram. Soc. JPN. 110 (2002) 597–600.

[5] A.T. Nelson, D.R. Rittman, J.T. White, J.T. Dunwoody, M. Kato, K.J. McClellan, J. Am. Ceram. Soc. 97 [11] (2014) 3652–3659.

[6] F.A. Kuznetsov, T.N. Rezukina, A. Golushenko, Zhur. Fiz. Khin. 34 (1960), 101 (referred in O. Knacke, O. Knbaschewski, and K. Hesselman, Thermochemical Properties of Inorganic Substances, 2nd ed., SpringerVerlag, Berlin, 1991).

[7] R.J.M. Konings, O. Bones, A. Kovács, D. Manara, D. Sedmidubský, L. Gorokhov, V.S. Lorish, V. Yungman, E. Shenyavskaya, E. Osina, J. Phys. Chem. Ref. Data. 43 (2014) 013101.

[8] H. Kopp, Phil. Trans. R. Soc. Lond. 155 (1865) 71–202.

[9] M. Khafizov, I.W. Park, A. Chernatynskiy, J. Lin, J.J. Moore, D. Swank, T. Lillo, S.R. Phillpot, A.E. Azab, D.H. Hurley, J. Am. Ceram. Soc. 97 (2014), 562–569.

[10] M. Hirai, J. Nucl. Mater. 173 (1990), 247–254.

[11] C. Ronchi, M. Sheindlin, M. Musella, G.J. Hyland, J. Appl. Phys. 85 (1999), 776.

[12] M.C. Roufosse, P.G. Klemens, J. Geophys. Res. 79 (1974) 703–705.

[13] J.K. Fink, J. Nucl. Mater. 279 (2000) 1–18.

[14] C.G.S. Pillai, P. Raj, J. Nucl. Mater. 277 (2000) 116–119.

[15] R.L. Gibby, J. Nucl. Mater. 38 (1971) 163–167.

[16] K. Ackland, J.M.D. Coey, Physics Reports. 746 (2018) 1–39.

[17] K. Gofryk, S. Du, C.R. Stanek, J.C. Lashley, X.Y. Liu, R.K. Schulze, J.L. Smith, D.J. Safarik, D.D. Byler, K.J. McClellan, B.P. Uberuaga, B.L. Scott, D.A. Andersson, Nat. Commun. 5 (2014) 4551.

[18] J.P. Moore, D.L. Mcelroy, J. Am. Ceram. Soc. 54 (1971) 40–46.
[19] F. Gendron, J. Autschbach, J. Phys. Chem. Lett. 8 (2017) 673−678.
[20] Y. Hinatsu, T. Fujino, J. Solid State Chem. 60 (1985) 195−202.
[21] S. Fukushima, T. Ohmichi, A. Maeda, H. Watanabe, J. Nucl. Mater. 105, (1982) 201−210.
[22] K. Iwasaki, T. Matsui, K. Yanai, R. Yuda, Y. Arita, T. Nagasaki, N. Yokoyama, K. Une, K. Harada, Nucl. Sci. Tech. 46, 7 (2009) 673−676.
[23] S.H. Kim, Y.G. Kim, H.S. Kim, S.H. Na, Y.W. Lee, D.S. Suhr, J. Nucl. Mater. 342, (2005) 119−124.
[24] S. Yamanaka, K. Kurosaki, M. Katayama, J. Adachi, M. Uno, T. Kuroishi, M. Yamasaki, J. Nucl. Mater. 389, (2009) 115−118.

CHAPTER 5

EVALUATION OF THE MECHANICAL PROPERTIES OF $U_{1-y}Ln_yO_{2-x}$ AND $Ce_{1-y}Ln_yO_{2-x}$ SOLID SOLUTIONS

5.1 Introduction

Mechanical properties such as the elastic moduli and Debye temperature of the fuel pellets are related to the sound velocities, i.e. depending on the density of samples, temperature, and chemical composition. The sound velocities in the CeO_2–$GdO_{1.5}$ samples were measured by the ultrasonic pulse-echo method. The mechanical properties such as elastic moduli and Debye temperature of CeO_2–$GdO_{1.5}$ were estimated from the sound velocities. The bulk modulus of CeO_2–$GdO_{1.5}$ was calculated by MD simulations as well. On the other hand, the data on the mechanical properties of UO_2–$LnO_{1.5}$ were investigated in the literature.

5.2 Ultrasonic pulse-echo method

The longitudinal and shear sound velocities in the pellets were measured at room temperature by the ultrasonic pulse-echo method (NIHON MATECH Echometer 1062) [1] in order to estimate the change in the mechanical properties, e.g. elastic moduli and Debye temperature, of CeO_2–$GdO_{1.5}$ with $GdO_{1.5}$ content. Figure 58 shows the schematic view of the apparatus of the ultrasonic pulse-echo method. The samples were cemented to the SiO_2 buffer, and the other end of the buffer was bonded to the 5 MHz longitudinal and shear sound wave echogenic transducer connected to the Echometer. The glue joint between the transducer and buffer was Sonicoat-SHN13 (Nichigo Acetylene. Corp.). The longitudinal wave and shear wave pulses were measured for measuring the longitudinal sound velocity and the shear sound velocity. Figure 59 illustrates the longitudinal and shear sound wave pulses of CeO_2 solid solutions.

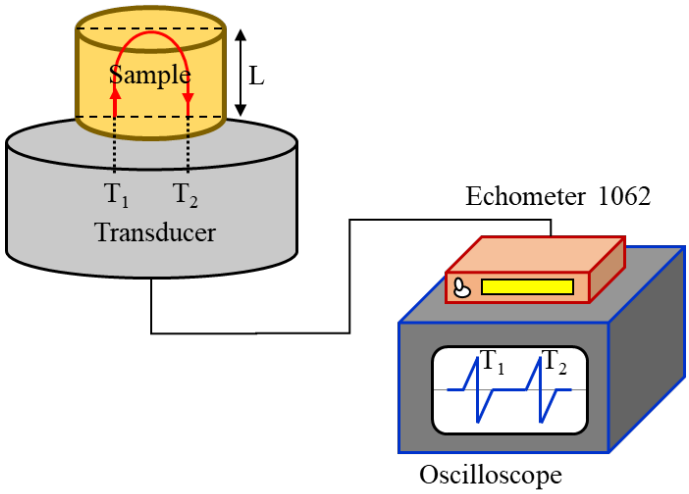

Figure 58. Schematic view of the ultrasonic pulse-echo method.

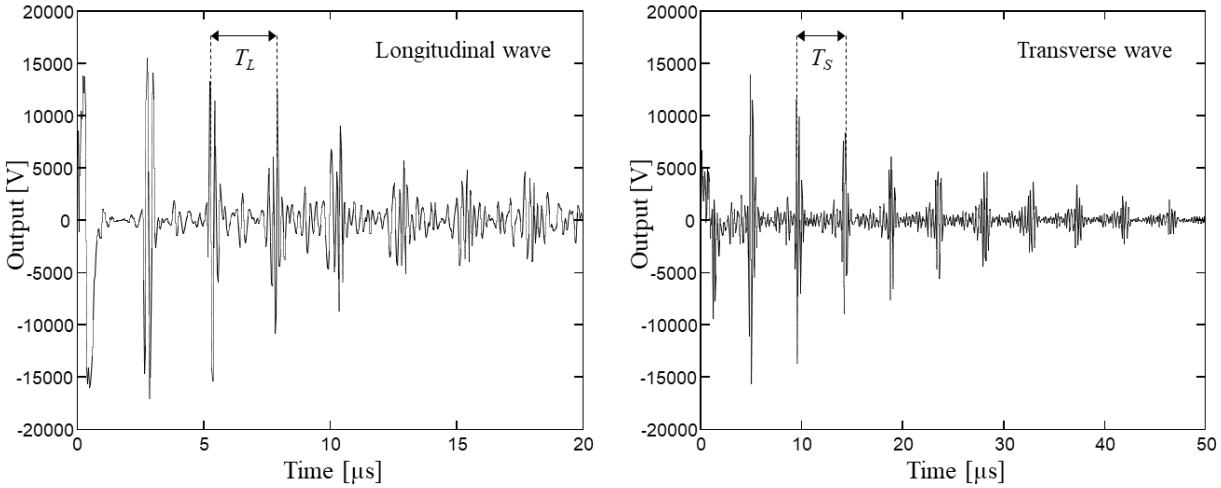

Figure 59. The longitudinal and shear sound wave pulses of CeO_2 solid solution.

The sound velocities in the sample were calculated from the sample length and the time separation between ultrasound echoes. Thus, the longitudinal and shear sound velocities were calculated by the following equation,

$$v_{L,S} = \frac{2L}{T_{L,S}}, \tag{30}$$

where v_L and v_S are the longitudinal and shear velocities, respectively; L is the length of the sample; T_L and T_S are the traveling time of these sound velocities in the sample ($T_{L,S} = T_2 - T_1$). From the obtained sound velocities, various important parameters of nuclear fuels which are mechanical properties such as the elastic moduli and Debye temperature for 96.5% of the theoretical density were evaluated.

5.3 Sound velocities

Table 12 summarizes the sound velocities of CeO_2–$GdO_{1.5}$ samples measured at room temperature in the present study. Figure 60 shows the relationship between the longitudinal and transverse sound velocities of CeO_2–$GdO_{1.5}$ and the relative densities. In the present study, the sound velocities of CeO_2 with various relative densities ranging from 84.59 to 93.64 %TD were measured while the sound velocities of the rest (CeO_2–$GdO_{1.5}$ solid solutions) were investigated corresponding to the relative densities of 95.88, 95.23, and 96.55 % TD, respectively. As can be seen from Fig. 47, the sound velocities of CeO_2 sample increased linearly with relative densities.

Table 12. Measured sound velocity data for CeO_2–$GdO_{1.5}$ solid solutions

$GdO_{1.5}$ content [mol %]	ρ^* [%TD]	v_L [m·s^{-1}]	v_L normalized to 96.5 % TD [m·s^{-1}]	v_S [m·s^{-1}]	v_S normalized to 96.5 % TD [m·s^{-1}]
0.0	84.59	5575		3035	
0.0	85.34	5630		3055	
0.0	86.22	5748		3115	
0.0	86.84	-		3121	
0.0	87.59	-		3129	
0.0	90.39	6088	6585	-	3424
0.0	90.49	6070		3235	
0.0	91.49	6193		3271	
0.0	91.84	6224		3284	
0.0	93.21	6311		3309	
0.0	93.64	6292		3324	
5.0	95.88	4972	5024	2800	2820
10.0	95.23	4678	4784	2643	2684
15.0	96.55	4610	4606	2635	2633

Although the longitudinal and transverse velocities of CeO_2–$GdO_{1.5}$ samples have not been investigated at different relative densities, the relation between their sound velocities and relative densities was assumed and considered to have the same tendency as CeO_2. According to this idea, the sound velocities for CeO_2–$GdO_{1.5}$ samples are, therefore, normalized to 96.5% TD based on the results obtained for CeO_2, and given in Table 12.

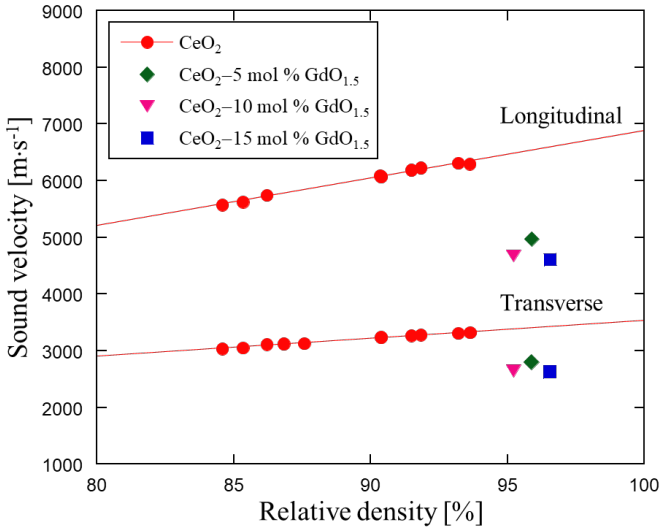

Figure 60. Longitudinal and transverse sound velocities of CeO_2–$GdO_{1.5}$ as a function of relative density.

Figure 61 shows the sound velocities of CeO_2–$GdO_{1.5}$ as a function of $GdO_{1.5}$ content together with those of the literrature for CeO_2, UO_2, and PuO_2 [2]. The sound velocity data for CeO_2 in this study agree well with the available literature data. The sound velocities were lower for specimens with higher $GdO_{1.5}$ content,

and substitutional Gd has a larger ionic radius than Ce. It is obvious that the propagation of sound waves is similar to that of micro-strains in the materials. As increasing Gd content, the anharmonicity of sound wave propagation in the CeO_2–$GdO_{1.5}$ solid solution may increase. Therefore, it is reasonable that the sound velocities of materials are related to the binding energy which joins the atoms to each other in the materials. According to this idea, the smaller binding energy leads to a decrease in the sound velocities. Thus, the dependence of the sound velocity on $GdO_{1.5}$ agreed with that of the thermal conductivity mentioned earlier. Accordingly, similar to the change in the thermal conductivity of CeO_2–$GdO_{1.5}$, the change in the sound velocities was large in the range from 0 to 5 mol %, whereas it was small at high $GdO_{1.5}$ concentration regions.

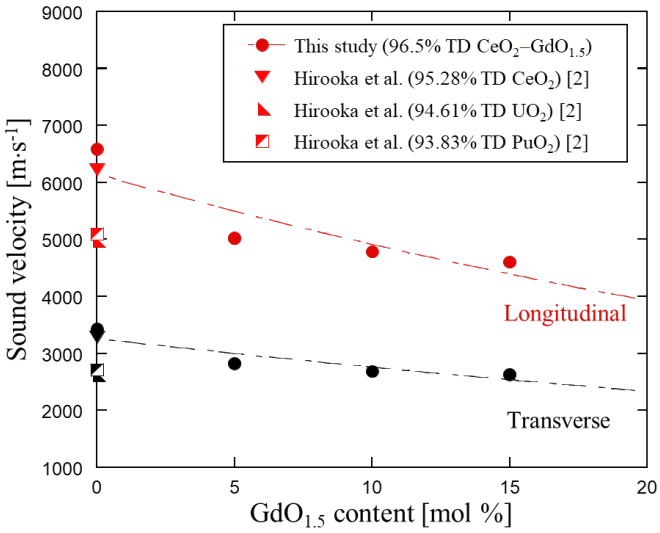

Figure 61. Sound velocities of CeO_2–$GdO_{1.5}$ solid solution samples. The lines are a guide to the eye.

5.4 Mechanical properties

As an important parameter of nuclear fuels, mechanical properties, e.g. the elastic moduli, and Debye temperature were estimated as well. From the measured sound velocities, which are extrapolated for a relative density of 96.5% TD, the elastic moduli (shear modulus G, bulk modulus K, Young's modulus E, and Poisson's ratio ν), and the Debye temperature Θ_D were estimated, as follows:

$$G = \rho v_S^2, \tag{31}$$

$$K = \rho v_L^2 - \frac{4}{3}\rho v_S^2, \tag{32}$$

$$E = \frac{9KG}{3K + G}, \tag{33}$$

$$\upsilon = \frac{E}{2G} - 1, \tag{34}$$

$$\Theta_D = \frac{\hbar}{k_B}\left[\frac{9N}{4\pi V(1/v_L^3 + 2/v_S^3)}\right]^{\frac{1}{3}} = \frac{\hbar}{k_B a}\left[\frac{3N}{4\pi}\right]^{\frac{1}{3}} v_P, \tag{35}$$

where ρ is the density of the sample, $\hbar$ is Planck's constant, k_B is the Boltzmann constant, N is the number of atoms in a unit cell, and V is the volume of the unit cell ($V = a^3$ in case of a cubic crystal structure).

The values of G, K, E, ν, and Θ_D estimated by Eqs. (31–35) are given in Table 13. Experimental shear and bulk moduli are plotted as a function of $GdO_{1.5}$ content in Fig. 62 (a), together with MD calculated bulk modulus. Bulk and shear moduli of CeO_2–$GdO_{1.5}$ solid solutions as $GdO_{1.5}$ content increased. These lattice defects decreased the sound velocity, and thereby decreased the experimental bulk modulus. The shear modulus also decreased with increasing $GdO_{1.5}$ content like the bulk one. As shown in Fig. 62 (b), Young's modulus of E (CeO_2) = 214.6 GPa showed a very good agreement with the value E = 206.0 GPa with 95.28 %TD reported by Hirooka et al. [2]. All elastic moduli of CeO_2–$GdO_{1.5}$ solid solutions decreased with increasing $GdO_{1.5}$ content.

Table 13. Mechanical property data for CeO_2–$GdO_{1.5}$ normalized to 96.5% TD

$GdO_{1.5}$ content [mol %]	E [GPa]	G [GPa]	K [GPa]	υ	Θ_D [K]
0	214.65	81.63	193.14	0.3148	482.71
5	140.75	55.41	102.00	0.2700	394.05
10	127.69	50.26	92.66	0.2703	373.87
15	121.71	48.40	83.60	0.2574	364.99

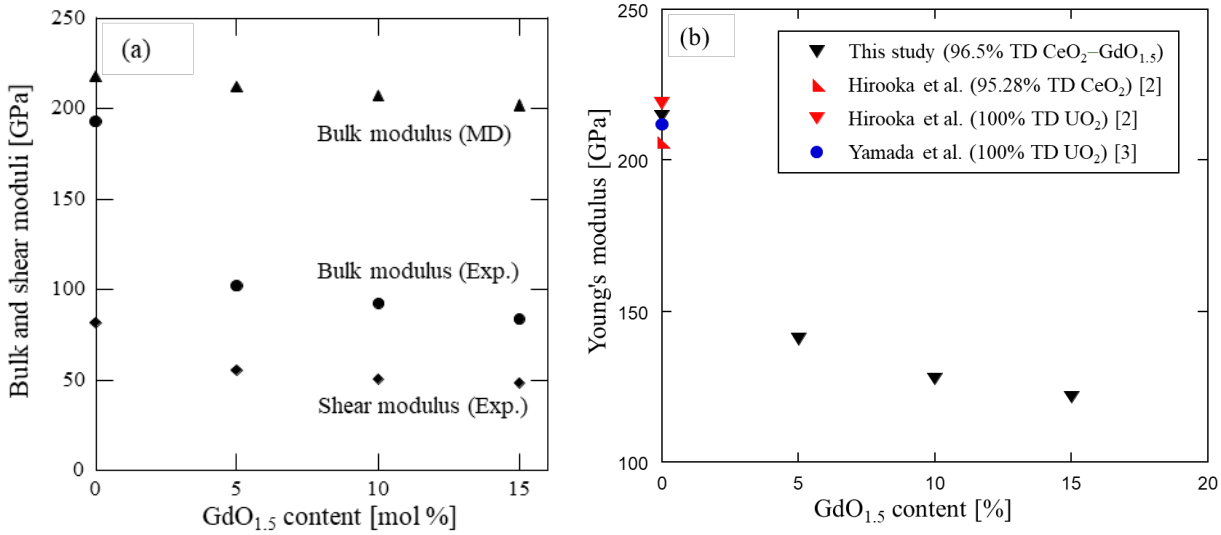

Figure 62. Elastic moduli (a) and Young's modulus data (b) of CeO_2–$GdO_{1.5}$ as a function of $GdO_{1.5}$ content (normalized to 96.5% TD).

Experimental results obtained from XRD measurement showed that the lattice parameters of CeO_2–$GdO_{1.5}$ samples increased with $GdO_{1.5}$ content and these samples formed the solid solution. In addition, MD calculation indicated that as $GdO_{1.5}$ content increased, the excess enthalpy of the solid solution increased for less than 15 mol % of $GdO_{1.5}$ content, which means that the lattice energy (or potential energy) shallowed slightly (Fig. 63 (a)). Thus, the elastic modulus decreased with increasing $GdO_{1.5}$ content.

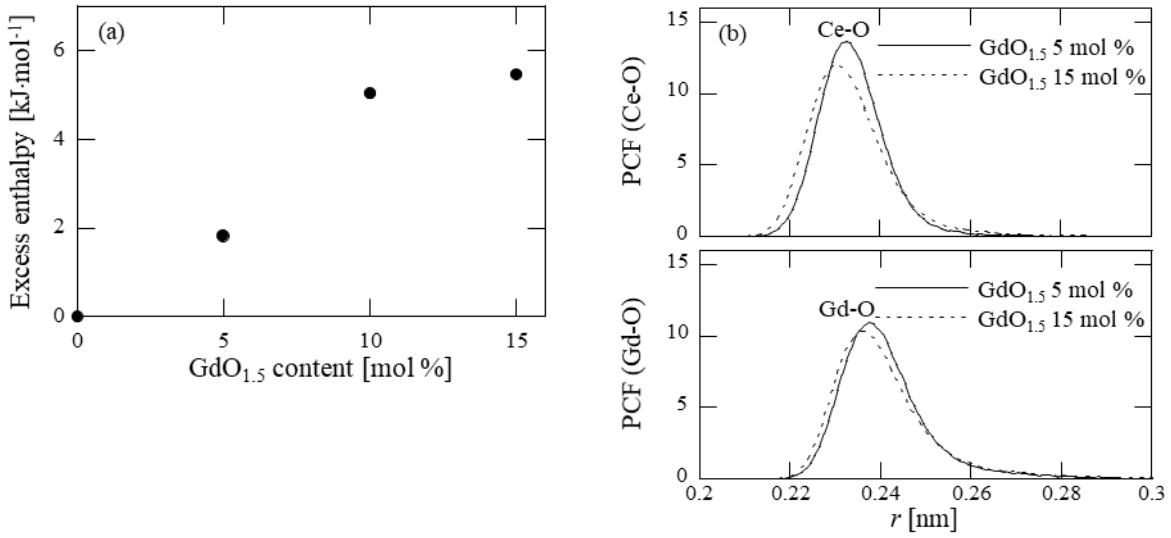

Figure 63. Excess enthalpy (a) Pair-correlation functions Ce-O and Gd-O (b) of CeO_2–$GdO_{1.5}$ by MD.

From the aspect of crystallographic information, the pair-correlation function (PCF) obtained from the present MD analysis and Inaba et al. [4] indicated that the nearest neighbor distance between Gd-O was longer than that of Ce-O and both decreased with an increase of $GdO_{1.5}$ content (Fig. 63 (b)). That was also confirmed by EXAFS measurement [5]. On the other hand, that of O-O increased with $GdO_{1.5}$ addition.

Further, the oxygen coordination number (CN) around Ce, as well as Gd ion, decreases with increasing $GdO_{1.5}$ content because of the increase of oxygen vacancies. Oxygen CN for Gd ion is smaller than that for Ce ion and than expectation from the assumption that oxygen vacancies randomly distributed on anion sites of a fluorite crystal structure. It can be interpreted that oxygen vacancy preferred the neighbor of Gd ion to that of Ce ion. Here, also from the aspect of the bond valence, the lattice energy is discussed. The bond valence sum, which is an effective valence of ion in an ionic crystal, is calculated based on the bond valence model suggested by Brown et al. [6], by the following equations,

$$\mathrm{BVS} = \sum_{i=1}^{CN} exp\left(\frac{r_0 - r_j}{b}\right), \tag{36}$$

where r_0 and b are constant (typically $b = 0.037$), r_j is the interatomic distance between Ce (or Gd) and O ions. The values of r_0 are 0.2028 and 0.2065 nm for Ce and Gd ions, respectively (Brese et al. [7]). Here, r_j is considered to be the average nearest neighbor distance (=$\Sigma PCF(r_j)\cdot r_j / \Sigma PCF(r_j)$) between Ce (or Gd) and O ions (Fig. 64). Note that the average nearest neighbor distance is not the value of r at the peak position of PCF (e.g. see Fig. 63) because these PCFs have an asymmetric form. The result, thus, obtained shows that both BVSs decreased with increasing $GdO_{1.5}$ content because it depended on oxygen CN rather than the average nearest neighbor distance in this case (Fig. 64). Therefore, the binding energy of CeO_2–$GdO_{1.5}$ solid solution weakened as the $GdO_{1.5}$ content increased, consequently, the elastic moduli decreased.

In other words, the mechanical properties of a solid solution depend on the Coulomb-attractive force between ions due to solid solutions have the ionic bond and the covalent bond, and the former is also related to the electrostatic (or Coulomb) attractive force. Each elastic modulus, which is defined as a proportional constant between stress and strain, is related directly to the binding energy. Therefore, the larger the elastic modulus is, the more difficult deformation becomes and hence the higher the binding energy is. Generally, it can be considered that the change of $GdO_{1.5}$ concentration or O/M ratio has a relation with ionic bond lengths. It is known that the elastic moduli decrease as bond length increases. The bond length of Ce-O in CeO_2 is found as 0.234303 nm. As the lattice parameters of CeO_2–$GdO_{1.5}$ increased with increasing $GdO_{1.5}$ content, the nearest Ce-O and Gd-O bond lengths in CeO_2–$GdO_{1.5}$ are not determined exactly but can be considered to be larger with $GdO_{1.5}$ addition, and Ce-O bond length was shorter than Gd-O distance. The shorter Ce-O distance compared with that of Gd-O may be due to the larger Coulomb interaction between Ce^{4+} and O^{2-} than that between Gd^{3+} and O^{2-}. However, it was experimentally confirmed in addition to MD calculation that nearest Ce-O and Gd-O bond lengths in CeO_2–$GdO_{1.5}$ decrease as $GdO_{1.5}$ content increases [4,5]. Therefore, the decrease in BVSs leading to the reduction in elastic moduli of CeO_2–$GdO_{1.5}$ was attributed to the decrease in CN as $GdO_{1.5}$ content increased.

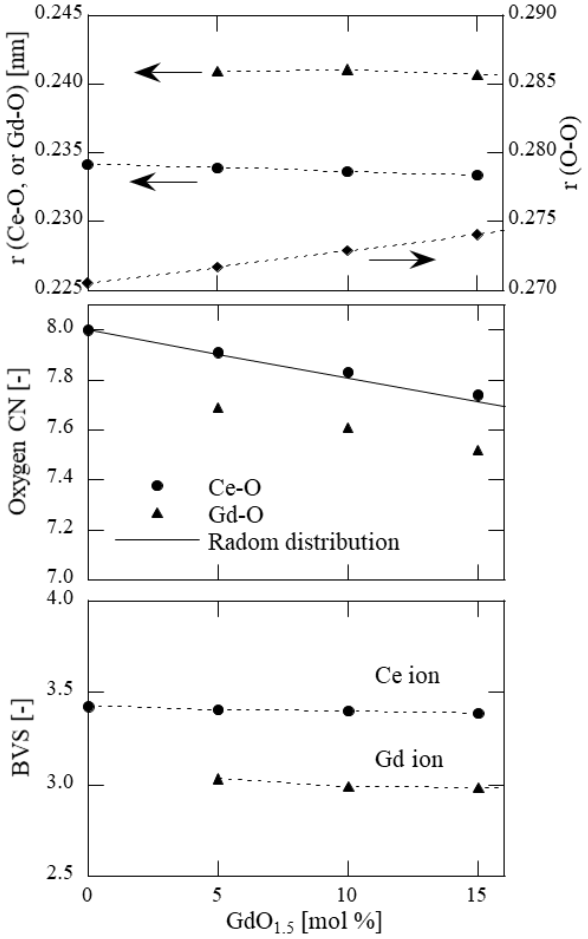

Figure 64. (a) The average nearest neighbor distance between Ce-O, Gd-O, and O-O; (b) Oxygen coordination functions for Ce and Gd ions; (c) Bond-valence sums for Ce and Gd ions. The dotted line is a guide to the eye.

In Fig. 65, the Poisson's ratio estimated from v_L and v_S appeared to decrease with the $GdO_{1.5}$ content. The value of the Poisson's ratio for CeO_2 ($\upsilon = 0.3148$) was in good agreement with the value $\upsilon = 0.307$ with 95.28 %TD reported by Hirooka et al. [2]. For the Debye temperature, which is associated with the hardness of materials, I derived Θ_D using the experimental sound velocities of CeO_2–$GdO_{1.5}$ with 96.5 %TD and the lattice parameters, *a*, obtained by XRD in the present study. The Debye temperature Θ_D for CeO_2 was estimated as $\Theta_D = 482.7$ K and agreed well with the value $\Theta_D = 484$ K [2]. In general, it is known that the Debye temperature decreases as the average mass of a compound or the atom distance increases. Because the nearest neighbor distance Ce-O and Gd-O in CeO_2–$GdO_{1.5}$ as $GdO_{1.5}$ content increased, the increase of average mass due to the $GdO_{1.5}$ addition mostly attributed to the decrease in Debye temperature as shown in Fig. 65.

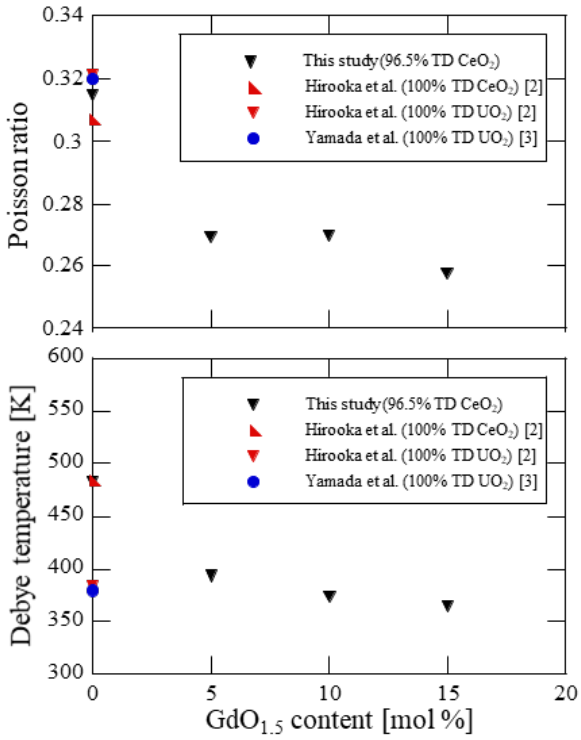

Figure 65. Poisson's ratio and Debye temperature of CeO_2–$GdO_{1.5}$ (normalized to 96.5% TD).

The sound velocities and the mechanical properties of UO_2–$LnO_{1.5}$ solid solutions were not investigated in the present study because of the difficulty in the preparation of UO_2–$LnO_{1.5}$ samples. However, some literature reported that the elastic moduli of UO_2–$LnO_{1.5}$ decrease as $LnO_{1.5}$ content increases. For instance, Young's moduli of UO_2 and $ErO_{1.5}$ are 227 GPa and 187 GPa, respectively and Young's modulus of UO_2–$ErO_{1.5}$ decreases as $ErO_{1.5}$ content increases up to 83 mol % [8]. The data on Young's modulus of UO_2–$GdO_{1.5}$ is limited [9]. In the paper [9] the elastic constants of UO_2–$GdO_{1.5}$ were measured at room temperature, and the results show that Young's modulus and the Poisson's ratio of UO_2–$GdO_{1.5}$ pellets decrease as $GdO_{1.5}$ content increases. Moreover, it is experimentally confirmed by Amaya et al. [10] that the Debye temperature of UO_2–$GdO_{1.5}$ decreases slightly as $GdO_{1.5}$ content increases stated from 267.25 K for UO_2 to 266.5 K for UO_2–27 mol % $GdO_{1.5}$. Therefore, it was confirmed that the $LnO_{1.5}$ doping into UO_2 decreased the sound velocities in the samples and thereby reduced its mechanical properties. Elastic modulus, which is related directly to the binding energy, is defined as a proportional constant between stress and strain. That means how difficult material deformation becomes. Therefore, the decrease in elastic moduli results in the deformation of nuclear fuels.

5.5 Summary

The longitudinal and shear sound velocities in CeO_2–$GdO_{1.5}$ solid solutions were investigated by the ultrasonic pulse-echo method and then the change in its mechanical properties was estimated as a function of $GdO_{1.5}$ content. The sound velocities were lower for specimens with higher $GdO_{1.5}$ content because of

the Gd doping into CeO_2 and an increase of oxygen vacancies. As a result, the elastic moduli and Debye temperature decreased with the $GdO_{1.5}$ addition. In addition, CeO_2 had close elastic moduli with UO_2 while its Debye temperature is higher than that of UO_2. On the other hand, MD calculations showed that oxygen CN decreased with increasing $GdO_{1.5}$. The bond valence sum calculated with the average nearest neighbor distance and oxygen CN for Ce (or Gd)-O decreased with increasing $GdO_{1.5}$, which is related to the reduction in the crystal binding energy. As a result, the bulk modulus estimated from MD analyses decreased with increasing $GdO_{1.5}$ content like experimental ones. However, for CeO_2–$GdO_{1.5}$ solid solution, the experimental elastic moduli were much smaller than that obtained by MD calculation. That difference may be attributed to the lattice defect, e.g. grain boundaries or cracks. On the other hand, $LnO_{1.5}$ doping into UO_2 decreased the sound velocities in the samples and thereby results in the degradation of its mechanical properties

5.6 References

[1] K. Shimamura, T. Arima, K. Idemitsu, Y. Inagaki, Int. J. Thermophys. 28 (2007) 1074–1084.

[2] S. Hirooka, M. Kato, J. Nucl. Sci. Tech. 55 (2018) 356–362.

[3] K. Yamada, S. Yamada, T. Nakagawa, M. Uno, M. Katsura, J. Nucl. Mater. 247 (1997) 289–292.

[4] H. Inaba, Solid State Inon. 122 (1999) 95–133.

[5] A. Kossoy, Q. Wang, R. Korobko, V. Grover, Y. Feldman, E. Watchtel, A.K. Tyagi, A.I. Frenek, I. Lubomirsky, Phys. Rev. B. 87 (2013) 054101.

[6] I.D. Brown, Chem. Rev. 109 (2009) 6858–6919.

[7] N.E. Brese, M. O'Keeffe. B47 (1991) 192–197.

[8] S. Yamanaka, K. Kurosaki, M. Katayama, J. Adachi, M. Uno, T. Kuroishi, M. Yamasaki, J. Nucl. Matter. 389 (2009) 115–118.

[9] M. Hirai, Annual meeting of Japan Atomic Energy Society. 34 (1988) 262.

[10] M. Amaya, K. Une, M. Hirai, J. Nucl. Sci. Tech. 41 (2004) 108–115.

CHAPTER 6

COMPARISON BETWEEN EXPERIMENTAL AND CALCULATED RESULTS

6.1 Introduction

The analytical method based on the statistical mechanics was used to calculate the heat capacity and the thermal conductivity with the help of computer simulation. Molecular dynamics simulation method (MD) is a computer simulation method for studying the physical movements of atoms and molecules. The method was originally developed within the field of theoretical physics in the late 1950s but is applied today mostly in chemical physics, materials science, etc. Simulations act as a bridge in another sense: between theory and experiment. A theory may be tested by conducting a simulation using the same model. In the present study, molecular dynamics simulation has been conducted on CeO_2–$LnO_{1.5}$ samples.

In the present study, the effect of Ln doping on the lattice structure and mechanical properties of CeO_2–$LnO_{1.5}$ solid solutions was evaluated by experimental and MD methods.

6.2 Molecular dynamics simulation (MD)

For CeO_2–$LnO_{1.5}$ solid solutions, the MD simulation was performed with the following Born-Mayer-Huggins potential using the MXDORTO program, which is developed by Hirao and Kawamura [1]:

$$U(r_{ij}) = \frac{z_i z_j}{r_{ij}} + f_0(b_i + b_j)\, exp\left(\frac{a_i + a_j - r_{ij}}{b_i + b_j}\right) - \frac{c_i c_j}{r_{ij}^6}, \tag{37}$$

where r_{ij} is the distance between i-th an j-th ions, z_i is the ionic charge. Ionic charges of Ce, Gd, Er, and O are +2.7e, +2.025e, +2.025e, and -1.35e, respectively. f_0 is the adjustable parameter for the unit. The potential parameters, a_i, b_i, and c_i, are obtained from Inaba et al. [2].

The simulations were done under the NTP ensemble (number of ions, temperature, and pressure are constant). The size of the supercell is 8 × 8 × 8 fluorite unit cells. For the solid solutions, Gd ions were randomly distributed on the cation sublattice sites. From the MD simulation, the crystallographic information, thermodynamic parameter, and bulk modulus were evaluated. Bulk modulus was the inverse of compressibility which was obtained from the relation between the supercell volume and pressure, where the pressure was varied from 0.1 MPa to 5 GPa. In the present study, the results obtained from the MD calculation were used to supplement the experimental ones.

In the equilibrium-MD simulation, the thermal conductivity can be calculated by the time auto-correlation function of energy currents expressed by the Green-Kubo formula [3]. It is usually given by:

$$k = \frac{1}{3k_B T^2 V} \int_0^\infty dt \langle \vec{J}(t) \cdot \vec{J}(0) \rangle, \tag{38}$$

where k_B is the Boltzmann constant, V is the volume of the simulated cell, and $\vec{J}(t)$ is the energy current.

The MD simulation of nuclear fuels using computational techniques is almost free not only from the regulations relevant to the radio-active materials but also from the limitations of experiments. Therefore, unlike experimental methods, the thermal properties of $(Ce,Ln)O_{2-x}$ and $(U,Ln)O_{2-x}$, i.e. heat capacity and thermal conductivity, can be investigated in the wide temperature range by the MD simulation.

6.3 Comparision between experimental and analytical results

Figure 66 shows the calculated lattice parameters of CeO_2–$LnO_{1.5}$ samples by MD calculation in comparison with the experimental results. The MD simulation used the cluster model, which assumed that that Ln^{3+} ions and oxygen vacancies were not randomly distributed on cation and anion sites, respectively, but defect clusters, e.g. Ln^{3+}–V_O–Ln^{3+}, were formed in CeO_2–$LnO_{1.5}$ solid solution. With the cluster model, the lattice parameters of CeO_2–$LnO_{1.5}$ were smaller than those of measured values. However, MD calculated results showed the same relation between the lattice parameters of CeO_2–$LnO_{1.5}$ and $LnO_{1.5}$ content as the measured results.

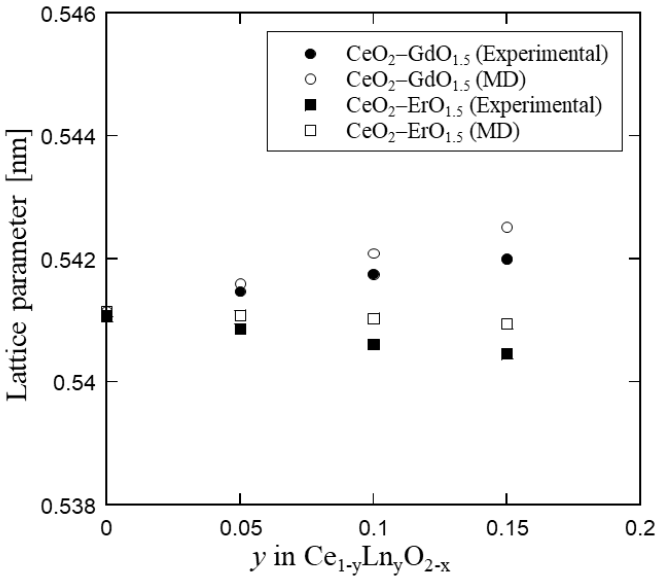

Figure 66. Lattice parameter of CeO_2–$LnO_{1.5}$ compared with the MD calculated results as a function of $LnO_{1.5}$ content.

Figure 67 shows the thermal conductivities of CeO_2–$GdO_{1.5}$ calculated by MD normalized with a porosity of 3.5% with error bars, as a function of $GdO_{1.5}$. Figure 68 indicates the thermal conductivities of CeO_2–$GdO_{1.5}$ obtained by MD calculations as a function of temperature, together with experimental results for comparison.

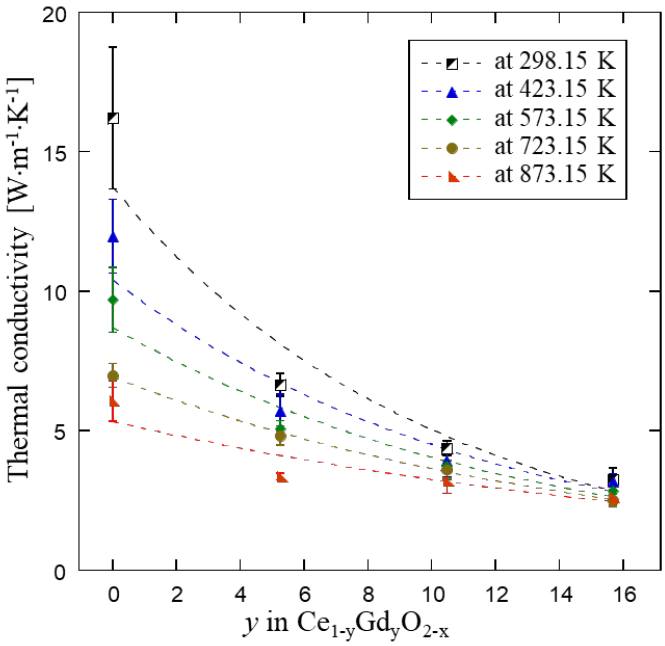

Figure 67. Thermal conductivity data calculated by MD simulations for CeO_2–$GdO_{1.5}$ as a function of $GdO_{1.5}$ content (normalized to 96.5% TD).

The thermal conductivities of CeO_2–$GdO_{1.5}$ obtained by MD were in good agreement with the experimental results at temperatures (above around 700 K). The temperature-dependent thermal conductivity obtained by MD simulations is comparable with experimental results up to nearly 900 K. The thermal conductivity of CeO_2 calculated by MD was higher than that measured by LFA, whereas calculated values of CeO_2–$GdO_{1.5}$ were lower than experimental values. In addition, the thermal conductivities obtained by both methods had a close tendency that the thermal conductivity decreased with temperature, which is due to the Umklapp processes (phonon-phonon scattering), especially at high temperatures. At low-temperature regions, however, there was a remarkable difference between MD and experimental results. Therefore, MD simulations showed comparable results with those of the experimental method at high temperatures.

On the other hand, the MD calculated bulk modulus of CeO_2–$GdO_{1.5}$ is plotted in Fig. 62 (a) together with experimental results. Both experimental and MD calculated bulk moduli decreased with increasing $GdO_{1.5}$ content, and those of CeO_2 are comparable. However, for CeO_2–$GdO_{1.5}$ solid solutions, the experimental bulk modulus is much lower than MD calculated value. Some intrinsic factors, e.g. substitutional Gd ions and oxygen vacancies, decrease experimental and MD calculated bulk moduli of CeO_2–$GdO_{1.5}$ solid solutions. So, such a large difference comes from another reason. Some unfavorable defects, e.g. cracks,

pores, and grain boundaries, for the sound velocity measurement are contained only in the experimental samples because the perfect crystals are used for the present MD calculation.

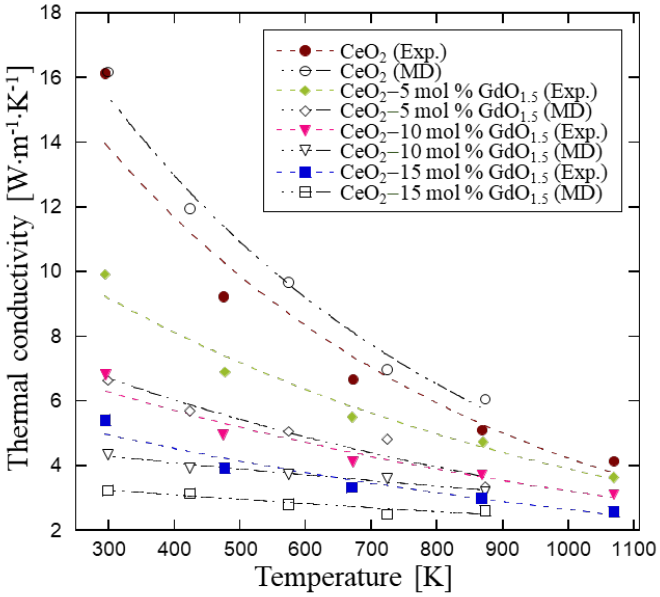

Figure 68. Thermal conductivity of CeO_2–$GdO_{1.5}$ calculated by MD compared to that measured by LFA, as a function of temperature (normalized to 96.5% TD).

6.4 Summary

As an analytical method, MD simulation was conducted to calculate the lattice parameters, thermal and mechanical properties of CeO_2–$LnO_{1.5}$ samples in order to compare with the experimental results. The results show that the lattice parameters, thermal, and mechanical properties calculated by MD agreed well with those of experimental values. The differences between calculated and experimental results were attributed to the effects of unexpected impurities and lattice defects, e.g. grain boundaries, pores, and cracks contained only in the experimental samples, were not taken into account in the present MD calculations.

6.5 References

[1] K. Hirao, K. Kawamura, Material Design Using Personal Computer, Shokabo, Tokyo. (1994) 54–54.

[2] H. Inaba, Solid State Inon. 122 (1999) 95–133.

[3] T. Arima, S. Yamasaki, Y. Inagaki, K. Idemitsu, J. of Alloys and Compounds., 400 (2005), 43–50.

CHAPTER 7

COMPARISION OF THE STRUCTURAL, THERMAL, AND MECHANICAL PROPERTIES BETWEEN $U_{1-y}Ln_yO_{2-x}$ AND $Ce_{1-y}Ln_yO_{2-x}$

7.1 Comparison of the structural, thermal, and mechanical properties

As mentioned above, in terms of crystal structures, it is experimentally confirmed that both CeO_2–$LnO_{1.5}$ and UO_2–$LnO_{1.5}$ solid solutions retained the same F-type structure up to 40 mol % $LnO_{1.5}$. For the lattice parameters, $GdO_{1.5}$ doping increased the lattice parameter of CeO_2–$GdO_{1.5}$ gradually, whereas it decreased the lattice parameter of UO_2–$GdO_{1.5}$. In both CeO_2–$ErO_{1.5}$ and UO_2–$ErO_{1.5}$ systems, when $ErO_{1.5}$ content increased, the lattice parameters of these solid solutions decreased.

Figure 69 shows the heat capacities of CeO_2 and UO_2 for comparison. The specific heat capacity of both CeO_2 and UO_2 solid solutions was close. In addition, the specific heat capacities for both UO_2–$LnO_{1.5}$ and CeO_2–$LnO_{1.5}$ systems increased with temperature up to nearly 1500 K and decreased as $LnO_{1.5}$ content increased.

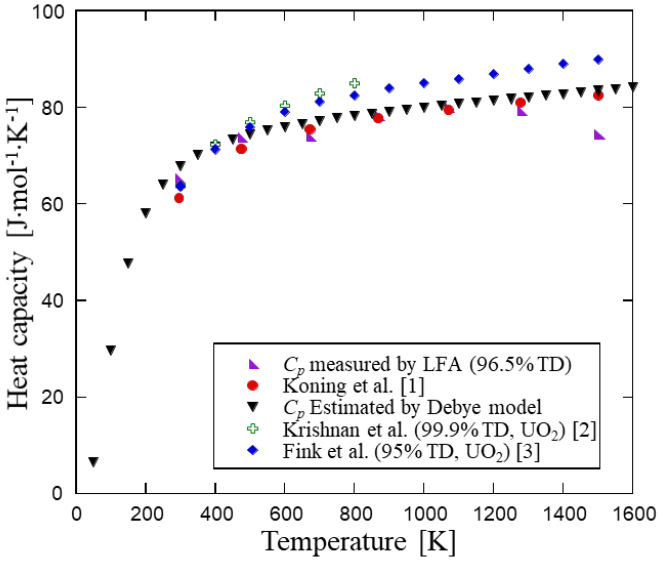

Figure 69. The heat capacity of CeO_2 compared with that of UO_2 as a function of temperature.

Regarding the effect of $LnO_{1.5}$ doping, although the significance of thermal conductivity for CeO_2–$LnO_{1.5}$ was higher than that for UO_2–$LnO_{1.5}$, those of both systems decreased with increasing $LnO_{1.5}$ content at any temperatures investigated and decreased with temperature up to 1500 K. In Fig. 70, the k/k_0 ratios of the thermal conductivities for CeO_2–15 mol % $GdO_{1.5}$ to that for CeO_2 and for UO_2–14.2 and 14.72 mol % $GdO_{1.5}$ to that for UO_2 were compared with calculated ratios for UO_2–$GdO_{1.5}$ system using Halden model [4–6]. Here, k is the thermal conductivities of CeO_2–$GdO_{1.5}$ and UO_2–$GdO_{1.5}$, k_0 is the thermal conductivities of CeO_2 and UO_2. Both UO_2–$LnO_{1.5}$ and CeO_2–$LnO_{1.5}$ solid solutions had a close tendency

where the thermal conductivity appeared to decrease with temperature in the range of interest and decrease with the $GdO_{1.5}$ addition as well. The k/k_0 ratios of the thermal conductivity for both CeO_2–$LnO_{1.5}$ and UO_2–$LnO_{1.5}$ systems were close. Thus, the relative influence of the $LnO_{1.5}$ doping effect on the thermal conductivity of both UO_2– $LnO_{1.5}$ and CeO_2–$LnO_{1.5}$ systems can be considered to be comparable.

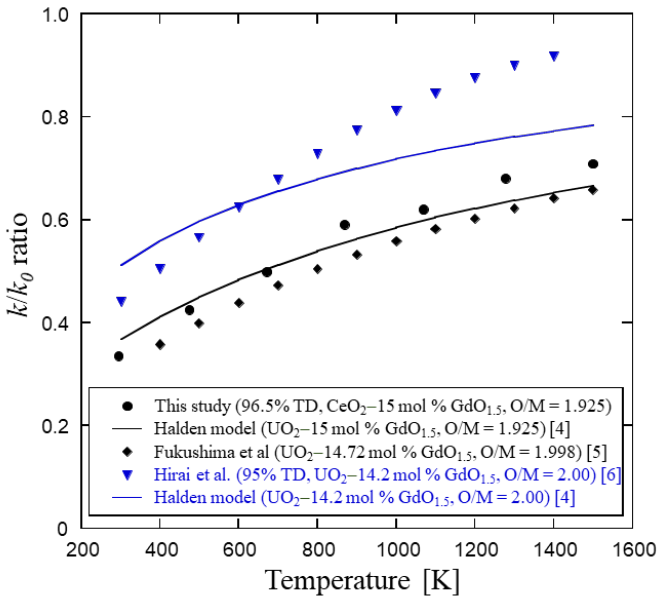

Figure 70. Thermal conductivity ratio in this study for CeO_2–$GdO_{1.5}$ compared to literature data for UO_2–$GdO_{1.5}$.

Regarding the mechanical properties such as the elastic moduli, and Debye temperature, CeO_2 had close elastic moduli in general and Young's modulus in particular with UO_2. In addition, CeO_2 had a close Poisson ratio with that of UO_2, whereas its Debye temperature was higher than that of UO_2. Besides, the elastic moduli and Debye temperature of both CeO_2–$GdO_{1.5}$ and UO_2–$GdO_{1.5}$ solid solutions were confirmed to depend on $GdO_{1.5}$ concentration that they decreased as $GdO_{1.5}$ content increased.

7.2 Summary

With the similarity in crystal structures of UO_2–$GdO_{1.5}$ and CeO_2–$GdO_{1.5}$, CeO_2 was used as a surrogate material for UO_2 and the mechanical properties of CeO_2–$GdO_{1.5}$ samples were investigated based on their sound velocities in this study. It was experimentally confirmed that UO_2–$LnO_{1.5}$ and CeO_2–$LnO_{1.5}$ had the same F-type structure up to 40 mol % $LnO_{1.5}$. Furthermore, the effect of $LnO_{1.5}$ doping on the UO_2–$LnO_{1.5}$ system was comparable to that effect on CeO_2–$LnO_{1.5}$ system, which means the thermal and mechanical properties of both samples decreased as the $LnO_{1.5}$ content increased.

7.3 References

[1] R.J.M. Konings, O. Bones, A. Kovács, D. Manara, D. Sedmidubský, L. Gorokhov, V.S. Lorish, V. Yungman, E. Shenyavskaya, E. Osina. J. Phys. Chem. Ref. Data. 43 (2014) 013101.

[2] R. Venkata Krishnan, K. Nagarajan, Thermochimica Acta. 440 (2006) 141−145.
[3] J.K. Fink, J. Nucl. Mater. 279 (2000) 1−18.
[4] S. Fukushima, T. Ohmichi, A. Maeda, H. Watanabe, J. Nucl. Mater. 105 (1982) 201−210.
[5] M. Hirai, S. Ishimoto, J. Nucl. Sci. Tech. 28 (1991) 995−1000.
[6] D.D. Lanning, C.E. Beyer, K.J. Geelhood, Technical Report NUREG/CR−6534, Vol. 4, PNNL−11513 (2005).

CHAPTER 8

CONCLUSION AND FUTURE WORK

8.1 Results and findings

In this study, the structural, thermal, and mechanical properties were evaluated for $U_{1-y}Ln_yO_{2-x}$ and $Ce_{1-y}Ln_yO_{2-x}$ (y = 0–0.4) solid solution samples by using both experimental and theoretical simulation methods. Here, with the similarity in crystal structures of UO_2–$GdO_{1.5}$ and CeO_2–$GdO_{1.5}$, CeO_2 was used as a surrogate material for UO_2 and the mechanical properties of CeO_2–$GdO_{1.5}$ samples were investigated based on their sound velocities.

SEM observation of the sample surfaces showed that $LnO_{1.5}$ doping into UO_2 and CeO_2 caused the depression of grain sizes of UO_2–$LnO_{1.5}$ and CeO_2–$GdO_{1.5}$ solid solutions. The porosities of these samples increased as the $LnO_{1.5}$ content increased. On the other hand, EDS analyses showed that the element segregation was not found on sample surfaces and the chemical composition of both UO_2–$LnO_{1.5}$ and CeO_2–$LnO_{1.5}$ samples remained almost unchanged during sintering. In addition, the samples had uniform element distribution and no other impurities.

The structural properties of UO_2–$LnO_{1.5}$ and CeO_2–$LnO_{1.5}$ solid solution samples were evaluated by various techniques, i.e., XRD, Raman spectroscopy, and XAFS. A single fluorite structure (F-type) was detected for most UO_2–$LnO_{1.5}$ samples sintered at 1973 K under Ar and Ar-10% H_2 atmospheres, indicating that Gd and Er were dissolved well in the UO_2 fluorite structure. For $LnO_{1.5}$ content of less than 5 mol %, a small amount of the U_4O_9 phase formed in the UO_2–$LnO_{1.5}$ samples. In the CeO_2–$LnO_{1.5}$ samples sintered at 1873 K in air, the F-type lattice was mainly retained until 40 mol % of $LnO_{1.5}$, though the small peaks of XRD pattern from C-type structure of Ln_2O_3 appeared and the small ones from the second phase formed in CeO_2–40 mol % $LnO_{1.5}$ samples.

The lattice parameters of UO_2–$LnO_{1.5}$ decreased as the $LnO_{1.5}$ content increased to 40 mol %. The UO_2–$LnO_{1.5}$ samples sintered in Ar-10% H_2 had a slightly larger lattice size than those sintered in Ar. Since the lattice parameter of UO_2–$LnO_{1.5}$ decreases as the O/M ratio increases, this observation indicated that the sample sintered under more reducing conditions with Ar-10% H_2 had a smaller O/M ratio than that sintered in Ar. However, the lattice parameters of UO_2–$LnO_{1.5}$ sintered under both conditions were close and they were also close to that of stoichiometric $(U,Ln)O_{2.00}$. When Ln^{3+} ions are substituted for U^{4+} ions in the host cation sites, either oxygen vacancies (V_O) are created or some of the U^{4+} are oxidized to U^{5+} or U^{6+} ions to maintain electrical neutrality. It was confirmed by XAFS that the oxidation state of U in the UO_2–$LnO_{1.5}$ was not solely tetravalent U^{4+}, partly oxidized to U^{5+}. A similar observation was obtained by Raman spectroscopy where the Raman spectra of UO_2–$LnO_{1.5}$ were close to that of U_4O_9. The U–O interatomic distances decreased slightly and Ln–O interatomic distance did not change with increasing

$LnO_{1.5}$ content. The shortening in the interatomic distances was in accordance with the contraction of the UO_2–$LnO_{1.5}$ lattices due to the dopant $LnO_{1.5}$. The presence of U^{5+} ions resulted in the reduction in the lattice parameter of UO_2–$LnO_{1.5}$.

For CeO_2–$LnO_{1.5}$ sintered in air, the lattice size of CeO_2–$GdO_{1.5}$ increased with increasing $GdO_{1.5}$ content, whereas that of CeO_2–$ErO_{1.5}$ decreased as the $ErO_{1.5}$ content increased. XAFS showed that Ce retained the Ce^{4+} cation, and both Ce–O and Ln–O interatomic distances decreased with increasing $LnO_{1.5}$ content. Therefore, the ionic radii of cations and V_O were supposed to determine the lattice sizes of these samples. The shortening in the interatomic distances was in good agreement with the contraction of the CeO_2–$ErO_{1.5}$ lattice, however, it was inconsistent with the expansion of the CeO_2–$GdO_{1.5}$ lattice. Based on MD (molecular dynamics) simulation results of the lattice parameters, it is supposed that Ln^{3+} ions and V_O are not randomly distributed on cation and anion sites, respectively, but defect clusters, e.g., Ln^{3+}–V_O–Ln^{3+}, formed in CeO_2–$LnO_{1.5}$ samples. Thus, MD analyses well explained the increase and decrease in lattice parameters of CeO_2–$GdO_{1.5}$ and CeO_2–$ErO_{1.5}$, respectively, with an increase of Ln^{3+} content at the atomic scale. Lattice parameters calculated by MD for CeO_2–$LnO_{1.5}$ suggested that the defect clusters, Ln^{3+}–V_O–Ln^{3+}, were formed in these solid solutions.

The thermal properties of UO_2–$LnO_{1.5}$ and CeO_2–$LnO_{1.5}$ were evaluated by LFA technique over the temperature range from room temperature to 1700 K. The heat capacities were also estimated by NKR to compared with that measured by LFA. The results showed that the thermal conductivities of UO_2–$LnO_{1.5}$ and CeO_2–$LnO_{1.5}$ decreased with temperature up to nearly 1700 K and they also decreased as $LnO_{1.5}$ content increased up to 40 mol %. Thermal conductivities of the samples were mostly determined by phonon mean free path, which decreases due to the Umklapp processes at high temperatures, and due to the increase of phonon scattering caused by the increase of dopant Ln and oxygen vacancies at low temperatures. The phonon scattering caused by grain boundaries, chemical impurities can be neglected, and the isotope effect is considered to be small. On the other hand, the thermal conductivities of CeO_2–$GdO_{1.5}$ calculated by MD simulations were comparable with the experimental values.

The mechanical properties of CeO_2–$GdO_{1.5}$ were evaluated by the ultrasonic pulse-echo technique and those of UO_2–$LnO_{1.5}$ were widely investigated in the literature. $LnO_{1.5}$ doping into CeO_2 or UO_2 caused the degradation of the mechanical of both CeO_2–$GdO_{1.5}$ and UO_2–$LnO_{1.5}$. The bond valence sum of CeO_2–$GdO_{1.5}$ calculated by MD decreased with increasing $GdO_{1.5}$. Therefore, the crystal binding energy of CeO_2–$GdO_{1.5}$ weakened with $GdO_{1.5}$ addition, consequently, its elastic moduli decreased.

The main goal of this work was to provide a comprehensive evaluation of the structural, thermal, and mechanical properties of UO_2–$LnO_{1.5}$ by using various advanced techniques. In fact, the literature data on these properties UO_2–$LnO_{1.5}$ solid solutions are limited and there is little literature on the atomic-scale structure of $GdO_{1.5}$- and $ErO_{1.5}$-doped UO_2 solid solutions. The thermal and mechanical properties of nuclear fuels are strongly dependent on their crystal structures. Especially, it was highlighted that atomic-

scale structures and properties of these nuclear fuels were directly explored by using XAFS. Thus, the results obtained from both experimental and simulation methods in this work are expected to use in the design of nuclear fuels and in the safety assessment of using burnable poison fuels in the LWRs.

8.2 Future work

The objective of this work is to evaluate systematically the effects of $LnO_{1.5}$ doping on the structural, thermal, and mechanical properties of UO_2–$LnO_{1.5}$ and CeO_2–$LnO_{1.5}$ solid solutions based on experimental results, and then to compare these results with the calculated results. Almost the intended targets were reached. However, while working on our study and proposal, I faced a lot of difficulties, and a small part of the intended work has not been done. Therefore, as the perspective of future works, I intend to proceed to further improvements and investigations. The potential improvements in detail for each research item are as below:

First, the O/M ratio is an important parameter of nuclear fuel properties, because it can affect the structural, thermal, and mechanical properties of nuclear fuels. This parameter, therefore, must be confirmed experimentally by measuring the oxygen potential pressure during sintering.

Regard the crystal structure, since the fact that the lanthanides such as Dy, Sm, Hf, and Eu have been also considered for burnable absorbers, in addition to Gd, and Er, it could be interesting to investigate the lattice parameters and the local structures of the above La-doped UO_2 solid solutions.

Finally, as one of the most important properties of nuclear fuel performance, the melting point of fuel pellets shall be evaluated by experiments. Therefore, another perspective of future work consists of measuring the melting points of the specimens and then evaluating the effects of their compositions. For this reason, the laser melting technique (LMT) has been developing to investigate the melting behavior of UO_2–$LnO_{1.5}$ and CeO_2–$LnO_{1.5}$ solid solution specimens. In fact, the LMT, which allows fast-melting and freezing processes, is being conducted under container-less and controlled atmosphere conditions using the thermal arrest technique obtained by a pyrometer. By using this method, the experiment's duration can be reduced, and the interaction between sample and holder can be minimized during melting point measurements. On the other hand, the melting points of these samples are being also evaluated by the high-speed camera, and thereafter compared with data obtained by the LMT. The schematic of the LMT apparatus is shown in Fig. 71.

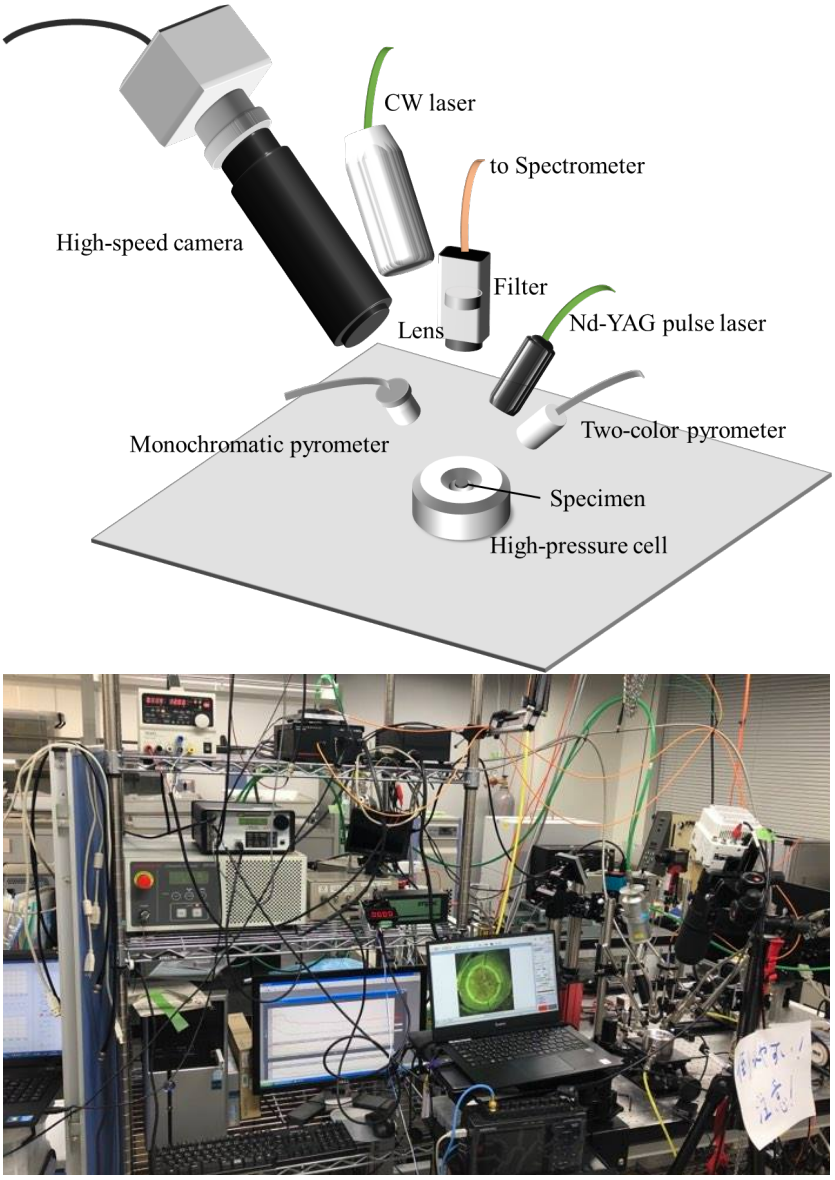

Figure 71. The schematic of melting point measurements by the LMT apparatus in this study.

Appendix

Appendix 1. Fitted parameters of U L_3 edge for UO_2–$LnO_{1.5}$ solid solutions

$LnO_{1.5}$ content [mol %]	Sintering atmosphere	S_0^2	CN	r [nm]	σ^2	ΔE	R
-, 0.0	Ar	1.01	8.09	0.2335	0.01153	6.40	1.99
-, 0.0	Ar	1.02	8.15	0.2337	0.01089	7.27	6.19
-, 0.0	Ar-10% H_2	1.08	8.37	0.2336	0.00678	5.43	5.00
Gd, 4.76	Ar	0.93	7.46	0.2319	0.01136	5.95	9.23
Gd, 5.00	Ar	0.99	7.94	0.2334	0.00994	6.65	1.56
Gd, 9.54	Ar	0.94	7.50	0.2317	0.01052	6.01	2.41
Gd, 10.00	Ar-10% H_2	1.09	8.26	0.2331	0.00790	5.94	2.57
Gd, 14.35	Ar	1.02	7.77	0.2320	0.01066	6.46	5.08
Gd, 15.00	Ar-10% H_2	0.93	7.43	0.2312	0.00498	4.60	7.92
Gd, 40.00	Ar	0.98	7.84	0.2273	0.00924	6.19	1.63
Gd, 40.00	Ar	0.95	7.56	0.2282	0.01012	6.84	7.51
Er, 4.76	Ar	0.98	7.80	0.2330	0.01188	6.66	3.78
Er, 5.00	Ar	1.11	8.09	0.2333	0.01042	6.38	4.05
Er, 9.54	Ar	0.94	7.56	0.2316	0.01013	5.93	5.32
Er, 10.00	Ar-10% H_2	1.02	8.06	0.2329	0.00740	5.71	5.31
Er, 14.35	Ar	1.02	8.14	0.2319	0.01103	6.24	3.63
Er, 15.00	Ar-10% H_2	1.02	8.17	0.2322	0.00767	5.81	3.03
Er, 40.00	Ar	1.06	8.08	0.2281	0.01223	5.95	5.53
Er, 40.00	Ar	1.05	8.4	0.2267	0.01122	5.91	5.24

Appendix 2. Fitted parameters of Gd L_3 and Er L_3 edges for UO_2–$LnO_{1.5}$ solid solutions

$LnO_{1.5}$ content [mol %]	Sintering atmosphere	S_0^2	CN	r [nm]	σ^2	ΔE	R
Gd, 4.76	Ar	1.18	8.22	0.2384	0.01057	2.42	2.33
Gd, 5.00	Ar	1.10	7.84	0.2420	0.00563	4.82	5.53
Gd, 9.54	Ar	1.15	8.31	0.2396	0.00961	3.32	4.77
Gd, 10.00	Ar-10% H_2	1.09	7.92	0.2404	0.00635	4.02	4.92
Gd, 14.35	Ar	1.15	7.70	0.2389	0.00897	2.77	1.10
Gd, 15.00	Ar-10% H_2	1.10	8.00	0.2385	0.00673	2.63	3.97
Gd, 15.00	Ar-10% H_2	1.15	8.09	0.2391	0.00553	3.32	0.99
Gd, 40.00	Ar	1.21	8.06	0.2386	0.01115	3.23	0.98
Gd, 40.00	Ar	1.16	7.72	0.2380	0.00952	3.16	1.11
Gd_2O_3	Pure powder	1.00	7.15	0.2339	0.01046	2.92	1.15
Gd_2O_3	Pure powder	1.04	6.23	0.2313	0.00879	3.16	3.55
Er, 4.76	Ar	1.12	8.36	0.2344	0.01029	4.74	7.37
Er, 5.00	Ar	-	-	-	-	-	-
Er, 9.54	Ar	1.18	8.06	0.2356	0.00917	5.10	2.35
Er, 10.00	Ar-10% H_2	-	-	-	-	-	-
Er, 14.35	Ar	1.15	7.53	0.2355	0.00779	5.11	1.55
Er, 15.00	Ar-10% H_2	1.20	8.17	0.2384	0.00955	7.08	3.65
Er, 15.00	Ar-10% H_2	1.25	8.13	0.2365	0.01251	5.69	2.41
Er, 40.00	Ar	1.20	8.28	2.357	0.01196	5.93	4.0
Er, 40.00	Ar	1.22	8.45	0.2342	0.01192	5.35	1.84
Er_2O_3	Pure powder	1.05	6.28	0.2252	0.00710	5.84	2.63
Er_2O_3	Pure powder	1.12	6.37	0.2251	0.00823	5.68	1.43

Appendix 3. Fitted parameters of Ce L_3 edge for CeO_2–$LnO_{1.5}$ solid solutions

$LnO_{1.5}$ content [mol %]	Sintering atmosphere	S_0^2	CN	r [nm]	σ^2	ΔE	R
-, 0.0	Air	0.70	8.06	0.2329	0.00870	10.59	6.62
Gd, 5.00	Air	0.70	8.00	0.2319	0.00857	10.30	4.01
Gd, 10.00	Air	0.70	7.58	0.2307	0.00886	9.65	4.62
Gd, 15.00	Air	0.70	7.26	0.2291	0.00843	9.04	4.71
Gd, 40.00	Air	0.70	7.26	0.2251	0.00874	8.26	3.68
Er, 5.00	Air	0.70	8.23	0.2316	0.00879	9.79	4.31
Er, 10.00	Air	0.70	7.36	0.2297	0.00798	9.24	3.82
Er, 15.00	Air	0.70	7.39	0.2297	0.00798	9.30	8.55
Er, 40.00	Air	0.70	7.25	0.2261	0.01056	8.33	3.22

Appendix 4. Fitted parameters of Gd L_3 and Er L_3 edges for CeO_2–$LnO_{1.5}$ solid solutions

$LnO_{1.5}$ content [mol %]	Sintering atmosphere	S_0^2	CN	r [nm]	σ^2	ΔE	R
Gd, 5.00	Air	1.00	6.81	0.2462	0.00809	10.00	10.57
Gd, 10.00	Air	1.01	8.08	0.2354	0.01195	2.92	7.51
Gd, 15.00	Air	1.00	8.25	0.2357	0.01211	3.27	1.51
Gd, 40.00	Air	1.00	7.15	0.2339	0.01046	2.92	1.15
Gd_2O_3	Pure powder	1.06	6.36	0.2317	0.00933	3.33	9.15
Er, 5.00	Air	1.04	6.25	0.2375	0.00220	9.73	4.95
Er, 10.00	Air	1.01	6.03	0.2368	0.00283	10.05	6.21
Er, 15.00	Air	1.01	7.95	0.2327	0.00809	7.36	4.00
Er, 40.00	Air	1.00	8.07	0.2282	0.01163	5.28	1.64
Er_2O_3	Pure powder	1.05	6.28	0.2252	0.00710	5.84	2.63